IMPRIMATUR POUR LA THÈSE

Microfabricated Probes with integrated Functions for Scanning Probe Microscopy

de M. Pierre-François Indermühle

UNIVERSITÉ DE NEUCHÂTEL

FACULTÉ DES SCIENCES

La Faculté des sciences de l'Université de Neuchâtel sur le rapport des membres du jury,

MM. N. de Rooij (directeur de thèse), H.-P. Herzig, U. Stauffer, H.-F. Siegenthaler (Uni. Berne) et P. Vettiger (IBM, Rüschlikon)

autorise l'impression de la présente thèse.

Neuchâtel, le 25 mars 1998

Le doyen:

F. Stoeckli

Table of contents

Abstract

Chapter 1: **Introduction**

Chapter 2: **Basics of scanning probe microscopy**

2.1 Introductioa II/1
2.2 How does an SPM work II/2
2.3 The Scanning Tunneling Microscope II/4
2.4 The Atomic Force Microscope II/6
2.5 The Scanning Near Field Optical Microscope II/13

Chapter 3: **Microfabrication technologies**

3.1 Introduction III/1
3.2 Materials III/2
3.3 Micromachining techniques III/4

Chapter 4: **Microfabricated tips**

4.1 Introduction IV/1
4.2 STM tips IV/2
4.3 AFM tips IV/3
4.4 SNOM tips IV/7
4.5 Stylus-like AFM dry etched tips IV/8
4.6 Tips locally coated with diamond IV/12
4.7 SNOM tips fabrication IV/14
4.8 Protection of tips during wet and dry etching processes IV/18
4.9 Conclusion to chapter 4 .... IV/22

Chapter 5: **xy-micropositioner with integrated tip**

5.1 Introduction V/1
5.2 Operating principle V/2
5.3 Structure design V/3
5.4 Fabrication process V/9
5.5 Electro-mechanical characterization V/13
5.6 AFM imaging V/16
5.7 Integration of a large protruding tip on the xy-micro stage V/20
5.8 Discussion and conclusion to chapter 5 .... V/25

Chapter 6: **Sharp silicon tips integrated on piezoelectric cantilevers**

6.1 Introduction VI/1
6.2 Structure design and fabrication VI/2
6.3 Electro-mechanical characterization VI/10
6.4 AFM imaging with piezoelectric cantilevers VI/16
6.5 Discussion VI/26
6.6 Conclusion to chapter 6 .... VI/30

Chapter 7: **Electrolytic thin layer STM probes**

7.1 Introduction VII/1
7.2 The Electrolytic Thin Layer Scanning Tunneling Microscope (ETL-STM) VII/2
7.3 Structure design and fabrication VII/4
7.4 Results VII/10
7.5 Conclusion to chapter 7 .... VII/16

Chapter 8: **Final conclusion**

Acknowledgments

List of publications

Abstract

The excellent suitability of Scanning Tunneling Microscopy (STM) and Atomic Force Microscopy (AFM) for high resolution surface imaging led to a fast development of these instruments. Commercial and user-friendly set-ups are now available for STM and AFM in liquid and in air, as well as microfabricated cantilevers for the different kinds of AFM.

Soon, attempts were made to fabricate devices for Scanning Probe Microscopy (SPM) with integrated functions to allow new kinds of measurements, higher imaging speed and lower production costs. At the beginning, the existing technology for the microfabrication of integrated circuits provided suitable techniques for these realizations. Then, techniques were specially developed for micromachining purposes.

During this thesis, micromachining techniques were used to fabricate AFM and STM probes with integrated actuating and sensing elements. First, fabrication techniques for integrated tips with special shape or coating were developed. Then a microfabricated xy positioner with integrated tip and electrostatic comb actuators was realized, and AFM images were achieved with it. Sharp reproducible tips were also integrated on piezoelectric cantilevers and the imaging quality of these devices was compared with commercial cantilevers and optical detection. Finally, a novel probe with integrated ring electrode around the tip for STM imaging in electrolytic thin layers was demonstrated.

Chapter 1

Introduction

1.1 The Golden Age of Scanning Probe Microscopy

1928: J. R. Oppenheimer showed that a weak electric field could dislodge electrons from a metal surface thanks to the tunneling effect [1].

1982: Utilizing this principle, G. Binnig and H. Rohrer developed the scanning tunneling microscope (STM) for imaging surfaces. This is achieved by scanning a conducting probe very close over the surface to be observed and measuring the resulting tunneling current between the probe and this surface [2].

For the first time, the resolution of a microscope was not obtained by focusing with lenses the waves emitted to or reflected by the object being examined. Instead, a probe was positioned close enough to the surface of this object to detect near field interactions. The Scanning Near-Field or Scanning Probe Microscopy was born. For the first time, it was also possible to observe monoatomic steps on a surface. In this new kind of microscopy, lateral resolution depended strongly on the sharpness of the probe. Chemically etched tungsten tips developed soon after allowed lateral resolution at the atomic level [3].

These results evoked much excitement in the scientific community, and STM rapidly became a very popular investigation medium. Unfortunately, this new and powerful kind of microscope could only be employed on conducting samples. This problem was solved in 1986 by G. Binnig and coworkers, who developed the atomic force microscope

(AFM) [4]. In this instrument, the effects of interatomic forces on a scanning probe were measured by monitoring the elastic deformation of a cantilever with the STM. This technique allowed the imaging of non-conducting surfaces with atomic resolution. Other forces like electrical or magnetic ones can also be used. The scanning probe microscope (SPM) or scanning near-field microscope family was growing.

Meanwhile, in 1984, the scanning near-field microscope concept was also applied to optical microscopy [5]. In this case, a very small aperture was scanned very close to the sample surface. The light collected or emitted by this aperture was used to image the surface topography. In this case, resolution is not limited by diffraction in optical microscopy.

1982-1986: Three fundamentally new observation tools were developed during this golden age of scanning probe microscopy.

1.2 The emergence of 3D microfabrication

Simultaneously, in the early eighties, processes which were used before only for IC fabrication started to be applied for the realization of three dimensional silicon structures [6]. This was a great opportunity especially for the fabrication of AFM sensors, because the very small forces which have to be detected required extremely soft and small cantilevers. Silicon turned out to be well suited for such mechanical applications and, furthermore, etching techniques could be developed to integrate sharp probes or tips on these cantilevers to increase lateral resolution.

During the last decade, microfabraction techniques were improved, allowing industrial fabrication of cantilevers [7] in a reproducible way. Today, arrays of fully integrated AFM cantilevers are microfabricated and used for parallel imaging [8, 9] and very high density data storage systems using AFM cantilevers and tips are being investigated [10, 11, 12].

1.3 Outline of the thesis

This thesis deals with the application of microfabrication techniques for the realization of SPM instruments with integrated functions. In chapters 2 and 3, basic SPM, and microfabrication techniques and materials will be described. As will be seen, silicon micromachining is well suited for the realization of devices which fulfill SPM requirements.

Chapter 4 is dedicated to the fabrication of tips. First, the standard techniques which are used to produce STM, AFM and SNOM tips will be presented. Then, a fabrication process for stylus-like dry etched tips will be discussed. This process allows the realization of AFM tips with an almost ideal shape: a rigid silicon micro column of about 7 µm height and 2 µm diameter is terminated by a sharp tip with high aspect ratio. Local diamond coating on the top of wet etched tips will also be presented. This very hard and chemically inert protection layer is of clear interest to avoid tip wear. A technique to open very small (less than 100 nm in diameter) apertures in a metal coating on SNOM tips will then be described. Finally, thick photoresist tip protection in wet and dry etching processes will be discussed.

Chapter 5 describes the fabrication and characterization of an integrated xy electrostatic micro stage with sharp tip and via hole for optical detection. Such a device may be of interest for applications such as the integration of an AFM inside a SEM or AFM measurements in outer space. First, design considerations and numerical simulation results will be discussed. Then, the fabrication process will be presented and the electro-mechanical behavior of the device will be characterized. Finally, an AFM image recorded with this integrated micro stage will be presented.

In chapter 6, the integration of a self-sharpening tip on cantilevers with piezoelectric elements for actuation and detection will be discussed. The integration of reproducible, sharp tips of equal height on arrays of self-actuating and self-detecting cantilevers is of primary importance for parallel AFM imaging. First, the fabrication process will be described and the devices will be electro-mechanically characterized. Then, AFM imaging will be demonstrated in both contact and dynamic mode.

Chapter 7 presents a new kind of STM probe, called the Electrolytic Thin Layer Scanning Probe Microscope (ETL-STM). This probe allows precise monitoring of chemical species involved in the electrolyte/electrode interface reactions during electrochemical scanning tunneling microscopy. First, the working principle of this new kind of STM will be discussed. Then, an original fabrication process which allows the growth of metal contacts through an insulating and chemically inert glass substrate will be described. Finally, first measurements, showing the validity of this new kind of STM, will be presented.

Chapter 8 will conclude this work. Results obtained in the previous chapters will be considered in view of possible further developments, and new applications will be suggested.

References to chapter 1

1. J. S. Rigden, Scientific American, July 1995, pp. 68-73
2. G. Binnig, H. Rohrer, Ch. Gerber and E. Weibel, Phys. Rev. Lett. 49 (1) 1982, pp. 57-60
3. G. Binnig, H. Rohrer, Ch. Gerber and E. Weibel, Phys. Rev. Lett. 50, 1983, p.120
4. G. Binnig, C. F. Quate and Ch. Gerber, Phys. Rev. Lett., 56 (9) 1986 pp. 930-933
5. D. W. Pohl, W. Denk and M. Lanz, Appl. Phys. Lett. 44 (7) 1984, pp.651-653
6. K. E. Petersen, Proc. IEEE, 70 (5) 1982, pp. 420-457
7. O.Wolter, Th.Bayer and J.Greschner, J. Vac. Sci. Technol., B 9, 1991, p.1353
8. S.C. Minne, S.R. Manalis and C.F. Quate, Appl. Phys. Lett. 67 (26) 1995, pp. 3918-3920
9. T. Itoh, C. Lee and T. Suga, Appl. Phys. Lett. 69 (14) 1996, pp. 2036-2038
10. H. J. Mamin and D. Rugar, Appl. Phys. Lett. 61 (8) 1992, pp. 1003-1005
11. M. Lutwyche et al., to be published in the Proceedings of the MEMS '98 Conference, Heidelberg (Germany) 1998
12. S. Hosaka et al., Nanotechnol. 8 (1997), pp. 1-5

Chapter 2

Basics of SPM

2.1 Introduction

In this chapter, the working principle of the different kinds of SPMs will first be very generally described. Basically, they all function in the same way: a sensor is scanned over the surface to be imaged. This sensor measures a physical quantity which is directly related to the distance between the sensor and the surface. During the scan, this distance is kept almost constant by a feed-back loop. This counter reaction signal is used to map the topography of the surface.

Each kind of SPM will then be described in more detail and a few words written about their performance and fields of application. As mentioned in Chap. 1, the present need for SPM integration will be kept in mind. Attention will be focused on the extent to which the components of these microscopes can or must be integrated by using micromachining techniques.

A short conclusion will summarize the most relevant aspects of the most important kinds of SPMs being used today.

2.2 How does an SPM work?

Fig. 2.2.1 shows schematically the basic structure of most standard commercial SPMs. Important elements are: the sensor, the signal amplifier, the feed-back controller and the positioning unit. In some cases, the sensor is mounted on the positioning unit itself to allow a stand-alone configuration or the use of a liquid or electrochemical cell.

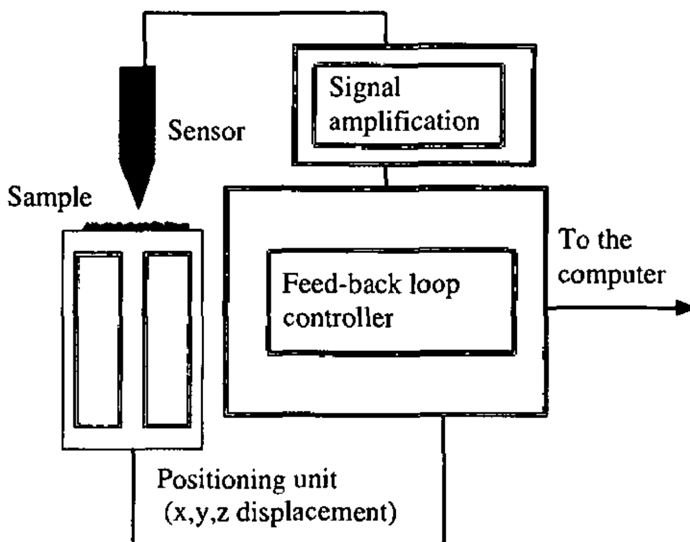

Fig. 2.2.1 Schematic representation of an SPM

The sensor is brought close enough to the sample to feel the variations of the physical quantity due to sample proximity. This physical quantity can be a tunneling current in the case of STM, or a force in the case of AFM. To insure good lateral resolution, the sensor needs to have a sharp tip geometry. In STM, the sensor has a simple structure: the tunneling current is measured directly between the metal tip and the

sample. In AFM, a two-stage sensor is needed: a force bends a cantilever, the deflection of which needs to be detected by a second sensor. Some SPM, like SNOM or MFM (Magnetic Force Microscope), measure physical quantities which are not necessarily related to the topography of the sample. In this case, it is of advantage to integrate the sensor on an AFM tip. The AFM then allows a constant distance to be accurately maintained from the sample surface.

As SPM should detect weak interactions, very small signals have to be detected. Thus, an amplification stage is required before sending the signal to the controller.

In this controller, a feed-back loop signal is generated to maintain the sensor at a constant distance from the sample surface. This is necessary to avoid the sensor from moving outside of the measuring range, in other words, from crashing into the surface or moving too far from it. Usually, this signal is used to record the topography of the sample surface.

This signal is sent to the positioning unit (generally a piezoelectric tube), which will move the sample or the sensor to keep the right distance between them. This piezoelectric tube usually also serves to scan the sample (or the tip, depending on the configuration). Of course, a computer is required for data storage and processing.

Micromachining techniques were used to integrate and to reduce the dimensions of the optical, electric and mechanical parts of the SPM (namely, the sensor and positioning unit). The most significant achievements will be presented in the following chapters.

2.3 The scanning tunneling microscope (STM)

Fig. 2.3.1 illustrates the sensing principle of this kind of SPM. If two conductors are submitted to a voltage difference U and brought close enough to each other, a tunneling current I appears between them. This current changes exponentially with the distance d between both electrodes and is proportional to the potential difference:

$$\mathbf{I \propto U \exp(-ad\sqrt{\Phi})} \qquad (2.1).$$

In this relation, a = 1.025 $Å^{-1}eV^{-1/2}$ and Φ is the height of the tunneling barrier (d being the width of this barrier) [1]. For typical barrier heights of a few electronvolts, voltage differences of a few hundred millivolts and distances of a few Ångströms, tunneling currents in the nanoampere range are measured.

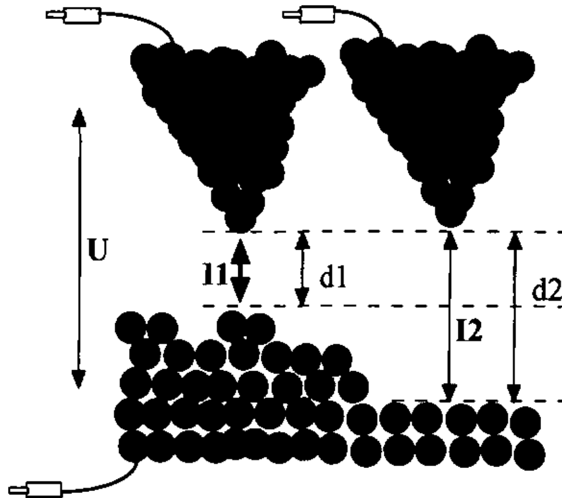

Fig.2.3.1 Distance measurement principle of the STM

Because the tunneling current changes exponentially with the tip-to-sample distance, very high vertical resolution is obtained with such a sensor. The lateral resolution depends strongly on the sharpness of the tip. Commercial tips, fabricated by electroetching of platinum/ iridium, gold or tungsten wire, allow atomic resolution in air on samples like gold or graphite.

Soon after its invention, the STM appeared to be the ideal tool for very high resolution surface studies. It bas been broadly used for UHV, biological and electrochemical applications. It was also used for surface modifications down to the atomic scale [2]. But, as appears in eq. (2.1), one of the major drawbacks of STM is that it may only be used on conductive samples.

A complete microfabricated STM scanner based on integrated piezoelectric actuators was built by S. Akamine and coworkers [3]. Atomic resolution on graphite was achieved with it. Other devices using electrostatic actuation were fabricated by Y. Xu and coworkers [4], by D. Kobayashi and coworkers [5], and by M. I. Lutwyche and Y. Wada [6].

A special microfabricated STM probe for measurements in electrolytic thin layer conditions will be presented in chapter 7.

2.4 The Atomic Force Microscope (AFM)

2.4.1 How does it work?

The principle of the AFM, also called Scanning Force Microscope (SFM), is very simple (cf. Fig. 2.4.1): when the free end of a cantilever is brought onto a surface with a force F, it is deflected by the reaction force F_R of this surface. By measuring this deflection and keeping it constant with a feed-back loop, it is possible to scan the surface with a constant force applied to the cantilever. If the cantilever is flexible enough to be deflected by interatomic forces in a detectable range, and if it is provided with a sharp tip to increase lateral resolution, surface imaging with atomic resolution becomes possible [7, 8]. Unlike STM, AFM can also be used on non-conductive surfaces.

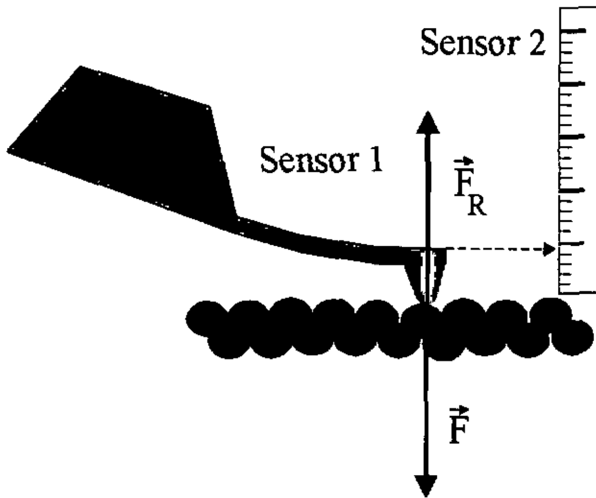

Figure 2.4.1 Force measurement with a flexible cantilever

2.4.2 Detection techniques

Thus, as mentioned above, an AFM sensor needs two stages: on the first one, the cantilever is deflected by a force; on the second one, this deflection is measured. Various solutions were used to do this and are presented in Fig. 2.4.2:

- **The tunneling tip** In the first AFM set-ups [7], a tunneling tip was mounted close to the backside of the cantilever. High resolution was obtained, but it was difficult to handle.
- **The laser beam deflection** [9] A laser beam is focused on the backside of the cantilever and reflected to a two-segment diode. This very simple technique is most commonly used in commercial systems.
- **Interferometer** [10, 11, 12] An optical fiber is positioned close to the backside of the cantilever. The portion of light which is reflected at the fiber-air interface is used as a reference beam. The interference with the beam reflected on the backside of the cantilever serves as the deflection measurement. High resolution is obtained with this system, but it is difficult to adjust the fiber. One can get rid of adjustment problems by integrating interdigitated fixed and flexible areas on the cantilever itself [13]. When a laser beam is focused on such a cantilever, the interference between light reflected by the fixed and movable parts is used for distance measurement.
- **Capacitance** A variable capacitance device can be built by mounting a rigid counter electrode very close to the backside of the cantilever. As the capacitance may also be used for AC and DC actuation, this allows the fabrication of compact probes which can be integrated in arrays [14, 15, 16]. Major drawbacks are very high sensitivity to noise and limited actuation amplitude.
- **Piezoresitive effect** The bulk resistivity of silicon strongly changes with applied stress. This effect has been used in two different ways to

detect a beam deflection. In the first method, a resistor loop is integrated on the cantilever and connected to a Wheatstone bridge [17]. This leads to a very compact and sensitive device which has been used as a detection element for parallel AFM imaging [18]. The second way consists of integrating a CMOS transistor at the base of the cantilever [19]. Changes in bulk resistivity induced by cantilever deflection generate variations in the channel carrier mobility, which in turn are responsible for source-drain current modifications. In addition to the other advantages of piezoresistive sensing, this configuration is fully CMOS compatible. Unfortunately, the integration of reproducible sharp tips on such cantilevers has not yet been realized.

- **Piezoelectric material** A piezoelectric layer may be used as an actuator [3], but also as a sensor [20, 21]. Cantilevers provided with such a layer were used to achieve parallel AFM imaging. The main advantage of this technology is that a single layer may be used simultaneously as a sensor and as an AC and DC actuator, thus reducing the number of technological steps needed to fabricate the devices. Efficiency and patterning techniques of piezoelectric materials are the major weaknesses of this technology. In chapter 6, cantilevers with integrated sharp tips and piezoelectric layers for actuation and detection will be discussed.

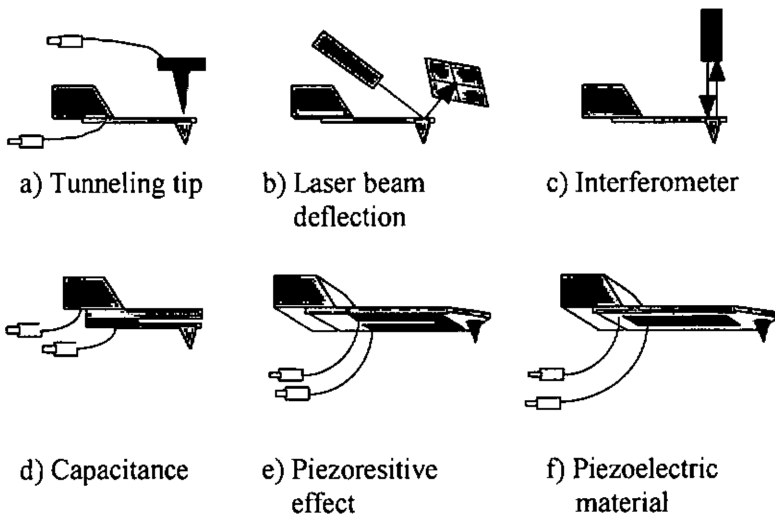

Fig.2.4.2 Detection techniques for AFM cantilever deflection

2.4.3 Operation modes

An AFM cantilever can be operated in two modes: quasi-static or dynamic. In the quasi-static mode, the tip is brought close to or in contact with the sample and scanned. The force applied on the tip is measured directly by the deflection induced on the cantilever and maintained constant by keeping this deflection constant with the feed-back loop. This mode allows relatively fast scanning rates and, if performed in contact mode (see below), lateral force measurements. However, for some special applications, like imaging of fragile surfaces (for example cellular membranes), or to avoid tip wear, one may use the so-called dynamic mode.

In this case, the cantilever is excited near its mechanical resonance frequency and forces are detected by the changes in amplitude, frequency and phase that they induce. This mode is slower than the contact mode, but, as no lateral forces are generated on the tip, the risk of breaking the tip is reduced. It therefore allows the use of tips with higher aspect ratio. This makes it particularly well suited for the imaging of deep trenches.

In Fig 2.4.3, the potential is presented as a function of the distance from the sample. When working in domain I, the tip is in contact with the sample surface and the cantilever is deflected by repulsive forces (contact mode). In domain II, the tip is maintained close to the sample surface and attractive forces are measured.

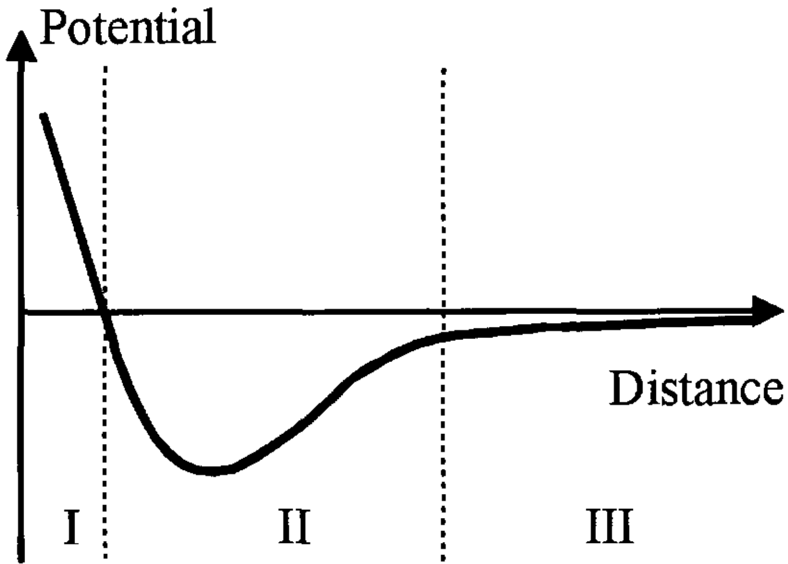

Fig. 2.4.3 Qualitative representation of potential versus distance to a sample surface. In domain I, repulsive forces will be measured; in domain II, the cantilever will be deflected by attractive ones; long range forces act in domain III.

2.4.4. Performances and actual trends

AFM has been widely used for imaging conductive and insulating surfaces in air, UHV or liquid with very high or even atomic resolution [22]. It has also been used as a writing tool [23]. To improve throughput, fabrication of arrays of cantilevers working in parallel is of interest. One of the final goals of these efforts is the realization of ultra-high density data storage systems.

In the first paper about AFM [7], the use of micromachining techniques for the fabrication of flexible cantilevers with high resonance frequencies was already mentioned. The present demand for arrays of cantilevers provided with highly reproducible tips and with fully integrated actuation and detection elements confirms and reinforces the strong relation between AFM and microfabrication. In chapter 5, an AFM device with integrated actuators for lateral scanning will be discussed.

2.5 The Scanning Near-Field Optical Microscope (SNOM)

Resolution in optical microscopy can be dramatically improved by decreasing the distance from the sample at which the microscope is operated [24], i.e by working in the near-field regime and by reducing the aperture of the sensor. This principle is illustrated in Fig. 2.5.1. To realize a device able to do this, a sharp tip made of optically transparent material is coated with a thin layer of highly reflecting metal (for example aluminum). On the apex, a small aperture with a diameter of a few tens of nanometers is created through the metal layer. Basically, such a microscope can be used in emitting or detecting mode. Among others applications, SNOM is particularly well suited for fluorescence imaging of biological objects [25].

As the optical properties of a surface can not always be related to its topography, SNOM imaging often needs to be associated with AFM distance detection. This is done by vibrating a tapered and metal coated optical fiber [26], or by integrating optical sensors on AFM tips [27, 28].

Micromachining technologies are thus widely used to integrate SNOM sensors on AFM cantilevers. In chapter 4, we will briefly describe a technique to open small apertures in the metal coating on tips.

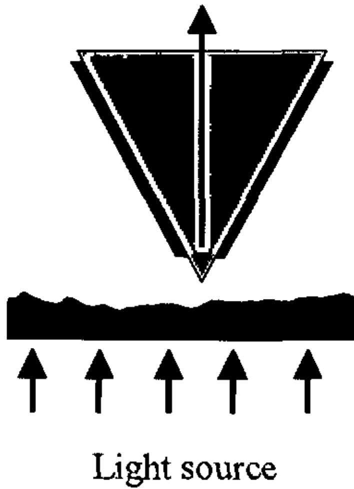

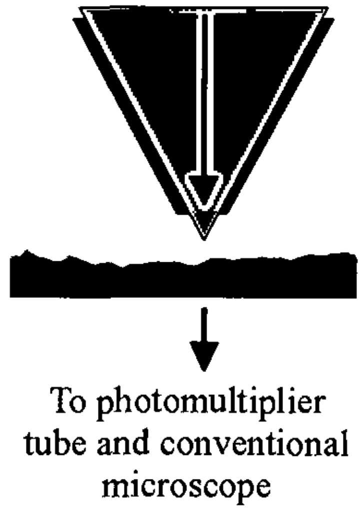

Fig.2.5.1 SNOM principle: (a) in detection mode, (b) in emission mode.

References to chapter2

1. G. Binnig, H. Rohrer, Ch. Gerber and E. Weibel, Phys. Rev. Lett. 49 (1) 1982
2. see for example: R. Wiesendanger and H.-J. Güntherodt (Eds), *Scanning Tunneling Microscopy I and II*, Springer Verlag, Berlin, 1992,1995
3. S. Akamine, T. R. Albrecht, M. J. Zdeblick and C. F. Quate, Sensors & Actuators A21 -A23 (1990) 964-970
4. Y. Xu, S. A. Miller and N. C. MacDonald, Proceedings of the Transducers '95 and Eurosensors IX Conference, Stockholm (Sweden), 1995, pp. 640-643
5. D. Kobayashi, T. Hirano, T. Furuhata and H. Fujita, Proceedings of the MEMS '92 Workshop, Travemünde (Germany), 1992, pp. 214-219
6. M. I. Lutwyche and Y. Wada, J. Vac. Sci Technol. B 13(6) 1995, pp. 2819-2822
7. G. Binnig, C. F. Quate and Ch. Gerber, Phys. Rev. Lett., 56 (9) 1986 pp. 930-933
8. see for example D. Sarid, *Scanning Force Microscopy,* Oxford University Press, 1991
9. G. Meyer and N. M. Amer, Appl. Phys.Lett. 53 1988, pp. 2400-2402
10. D. Rugar, H. J. Mamin, R. Erlandsson, J. E. Stern and B. D. Terris, Rev. Sci. Instrum. 59 (11) 1988, pp.2337-2340
11. C. Schönenberger and S. F. Alvarado, Rev. Sci. Instrum. 60 (10) 1989, pp. 3131-3134
12. D. Anselmetti, Ch. Gerber, B. Michel, H,-J. Güntherodt and H. Rohrer, Rev. Sci. Instrum. 63 (5) 1992, pp3003-3006

13. S. R. Manalis, S. C. Minne, A. Atalar and C. F. Quate, Appl. Phys. Lett.69 (25) 1996 pp.3944-3946
14. T. Göddenhenrich, H. Lemke, U. Hartmann and C. Heiden, J. Vac. Sci. Technol. A 8 (1) 1990, pp. 383-387
15. G. Neubauer, S. R. Cohen, G. M. McClelland, D. Horne and C. M. Mate, Rev. Sci. Instrum. 61 (9) 1990, pp. 2296-2308
16. N. Blanc, J. Brugger, N. F. de Rooij and U. Dürig, J. Vac. Sci. Technol. B 14 (2) 1996, pp. 901-905
17. M. Tortonese, R. C. Barrett and C. F. Quate, Appl. Phys. Lett. 62 (8) 1993, pp. 834-836
18. S. C. Minne, S. R. Manalis and C. F. Quate, Appl. Phys. Lett. 67 (26) 1995, pp. 3918-3920
19. T. Akiyama, A. Tonin, H. R. Hidber, J. Brugger, P. Vettiger, U. Staufer and N. F: de Rooij, Proceedings of the MEMS '97 Workshop, Nagoya (Japan), 1997, pp. 141-146
20. K. Takata, Jpn. J. Appl. Phys. 32, 1993, pp.2455-2458
21. T. Itoh, C. Lee and T. Suga, Appl.Phys. Lett. 69 (14) 1996 pp. 2036-2038
22. R. Lüthi, E. Meyer, M. Bammerlin, A. Baratoff, T. Lehmann, L. Howald, Ch. Gerber and H.-J. Güntherodt, Z. Phys. B 100, 1996, pp. 165-167
23. S. C. Minne, P. Flückiger, H. T. Soh and C. F. Quate, J. Vac. Sci. Technol. B 13, 1995, p.1380
24. D. W. Pohl, W. Denk and M. Lanz, Appl. Phys. Lett. 44 (7) 1984, pp.651-653
25. see for example H. Heinzelmann and D. W. Pohl, Appl. Phys. A 59 (1994) 89-101

26. E. Betzig, Proc. NFO I: "Near Fields Optics", NATO ASI Series E, Vol.242, ed. By D. W. Pohl and D. Courjon, 1993, p. 7
27. R. C. Davis, C. C. Williams and P. Neuzil, Optics Letters, 21 (7) 1996, pp. 447-449
28. H. Yamada, H. Tokumoto, S. Akamine, K. Fukuzawa and H. Kuwano, J. Vac. Sci. Technol. B 14 (2) 1996, pp. 812-815

Chapter 3

Microfabrication technologies

3.1 Introduction

The aim of this chapter is not to make an exhaustive review of the existing microfabrication techniques but to present the materials and technologies related with the devices discussed in this dissertation.

In 1967 already, H. C. Nathanson and coworkers [1] proposed to use the planar IC technologies to build three-dimensional devices. But, until recently, very few specific technologies or materials were developed for three-dimensional fabrication purposes [2, 3]. The increasing interest for micromachined instruments for research or industrial applications [4, 5] has led to the development of new and powerful technologies for three-dimensional microfabrication. Materials with improved properties, as well as deposition and etching techniques with higher resolution and aspect ratio, are now specifically designed for these kinds of applications.

Planar techniques now allow the realization of two-dimensional objects with lateral dimensions of a hundred or even some tens of nanometers. Three-dimensional structures with lateral dimensions smaller than ten micrometers and with aspect ratios as high as one hundred can also be fabricated.

3.2 Materials

Monocrystalline silicon is by far the most utilized material in electronics as well as in microfabrication. Its electrical and mechanical properties and its low cost make it an irreplaceable element in many processes. The electrical properties can be well controlled by doping it positively or negatively. This can be done in the bulk material during crystal growth or on the wafer surface with ion implantation or high temperature diffusion.

Grown silicon dioxide or deposited silicon nitride serve as good electrical insulators and can be easily patterned with dry or wet etching techniques. For the principle etching processes, a good selectivity for the materials involved is desirable. For example, the <100> plane of monocrystalline silicon is etched much quicker in KOH than silicon dioxide or silicon nitride. In turn, silicon dioxide is easily etched in HF but not silicon or silicon nitride. Thanks to this selectivity and to its mechanical properties, silicon nitride is often used for the fabrication of very thin, overhanging structures (for example membranes or cantilevers). Another interesting property of nitride is its ability to impede oxide growth, leading thus to the so-called Local Oxidation of Silicon (LOCOS) processes. This technique was used to locally protect a sharp silicon AFM tip during the process described in chapter 6.

Silicon can also be grown in epitaxial layers or deposited as polycrystalline silicon or polysilicon. This allows the production of wafers with a buried oxide or nitride layer. The major drawback of this technique is that the upper silicon layer is of limited thickness (about ten micrometers). If a thicker layer is desired, the silicon fusion bonding can be used [6]. This technique is now widely utilized for the production of Silicon on Insulator (SOI) wafers. It was also used to realize the device

discussed in chapter 5. Other bulk materials such as glass, quartz or gallium arsenide (GaAs) are used for specific applications. In chapter 7, a special STM probe made of photostructurable glass (Foturan) [7] will be discussed.

Photoresists were primarily used as thin layer masking material for subsequent wet or dry etching. In recent developments, they also proved their reliability as thick molding material [8, 9]. In chapter 4, a thick photoresist application will be presented.

Metals, although mostly used for electric contacts, may also serve for the fabrication of electro-mechanical microtools [10]. This is especially true with recent developments in molding techniques like LIGA or deep photoresist. Metals may also be well-suited as electrodes for electrochemical applications [11].

Piezoelectric ceramics like zinc oxide or, more recently, lead zirconate titanate, are used as surface actuators for membranes or cantilevers and will be discussed in chapter 6.

Diamond is a very promising material from electrical, mechanical and chemical points of view [12, 13]. In chapter 4, an AFM tip with local diamond coating will be presented.

3.3 Micromachining techniques

Micromachining techniques may basically be divided into two groups: surface and bulk micromachining. Most of the surface micromachining techniques come directly from IC technology, but, as the field of micromechanics matured, a specific technology was developed. Bulk micromachining, on the other hand, was specifically developed with micromachining in mind.

3.2.1 Surface micromachining

Surface micromachining consists mainly of growing or depositing layers on a substrate, generally a silicon wafer, and patterning them. Growth can be carried out at high temperature in a controlled atmosphere (as for silicon dioxide) or electrochemically (as for molded metal). Deposition can be made by evaporation (metals), sputtering (piezoelectric ceramic) or chemical vapor deposition (CVD) (oxide or nitride). CVD may be performed at low pressure (and high temperature) or with plasma enhancement (lower temperature).

Thin layers are generally patterned by spinning and patterning photoresist on them. In this way, a mask is reproduced in a photoresist pattern which is in turn transferred into the wanted material by etching the exposed parts of this material with wet or dry etching techniques. For some applications, the so-called lift-off technique is used. In this case, metal is deposited on the patterned photoresist, which is then removed in a solvent. A negative of the photoresist pattern is produced in the metal layer in this way.

Fig. 3.2.1 shows a typical surface micromachining process. In this case, structures are made of polycrystalline silicon. First, a passivation layer (silicon dioxide or nitride) is grown or deposited on a silicon wafer.

Then, a sacrificial layer is deposited and patterned (a). Then, a polysilicon layer is deposited and also patterned (b). Finally, the sacrificial layer is removed (c). Fig. 3.2.2 shows an electrostatic comb actuator realized with this technique.

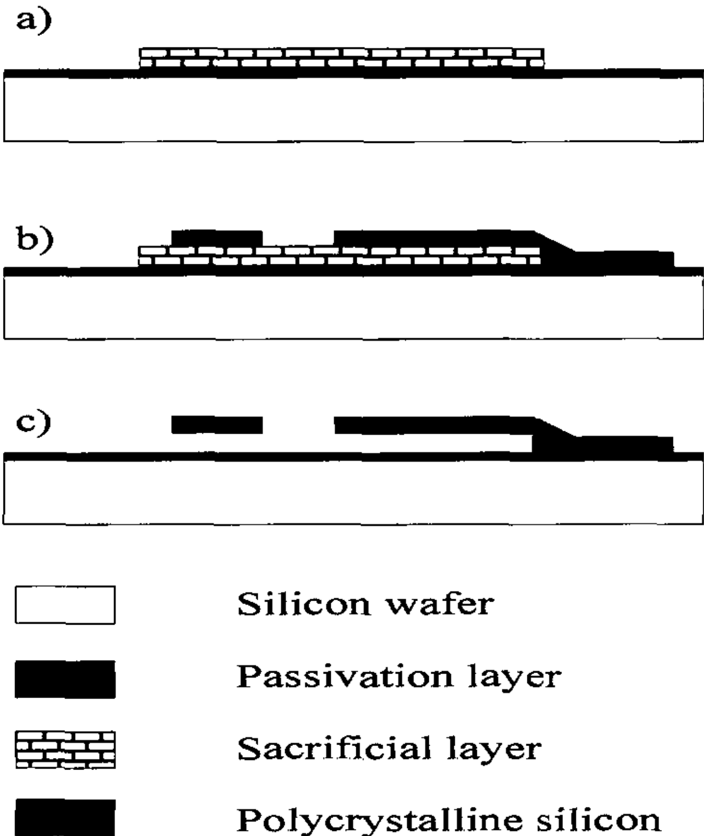

Fig.3.2.1 Typical polycrystalline silicon surface micromachining fabrication process. A passivation layer is deposited or grown on a silicon wafer prior to deposition of a sacrificial layer (a). Then, the polysilicon layer is deposited and patterned (b) Finally, the sacrificial layer is removed (c).

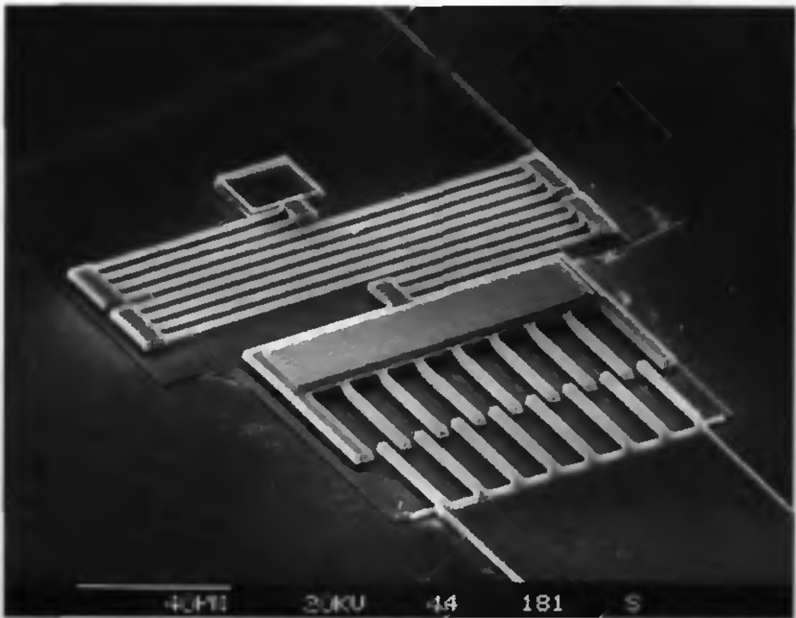

Fig. 3.2.2 Polycrystalline silicon electrostatic comb actuator realized with surface micromachining using a sacrificial layer technique [14].

3.2.2 Bulk micromaching

Until a few years ago, bulk micromachining consisted predominantly of the use of wet etchants like potassium hydroxide (KOH), ethylendiamine-pyrocatechol (EDP) or cesium hydroxide (CsOH) to release cantilevers or membranes. So-called mesas, accelerometer masses or AFM tips were also etched in this way. The basic idea is to use the very high anisotropy of these etches relative to the crystallographic planes of silicon to obtain three dimensional bodies with well defined geometry. As silicon dioxide and nitride have a much smaller etch rate than the silicon planes, they are used as masking materials. Etch stop techniques were developed to allow a safe etching of thin silicon membranes [15].

Fig. 3.3.1 shows a schematic bulk fabrication process for accelerometers with piezoresistive sensors. First, a passivation layer is deposited or grown and patterned on both sides of a silicon wafer. On the upper side, this layer (silicon dioxide or nitride) will serve as a passivation layer. On the lower side, it will serve as a mask for the final anisotropic etch (a). In the next step (b), the piezoresistors are fabricated. Finally, the mass of the accelerometer and the support beams are defined by bulk anisotropic etching. Fig. 3.3.2 shows a micrograph of such a device.

The development of new materials like photosensitive glass [7] and of new etching techniques like deep dry etching [16, 17] allows the micro fabrication of three-dimensional devices in higher density and with much higher aspect ratios.

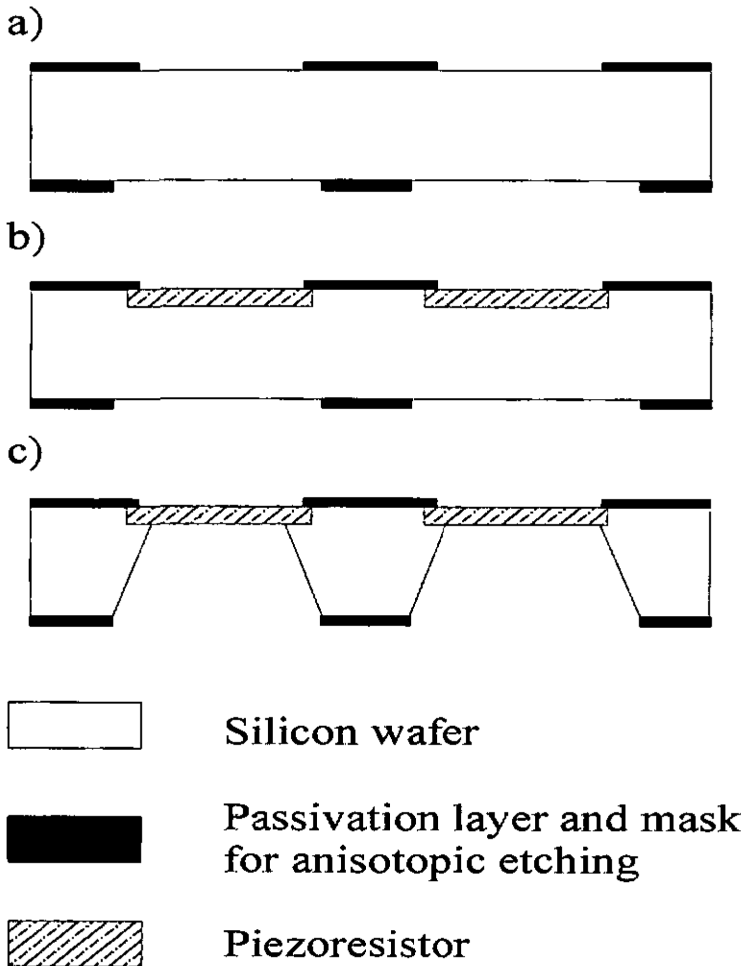

Fig. 3.3.1. Schematic bulk micromachining process for an accelerometer with piezoresistive sensors. (a) Deposition or growth of silicon dioxide or nitride as passivation layer on the upper face and as mask on the lower face. (b) Fabrication of piezoresistive sensors. (c) Release of the mass and the supporting beams.

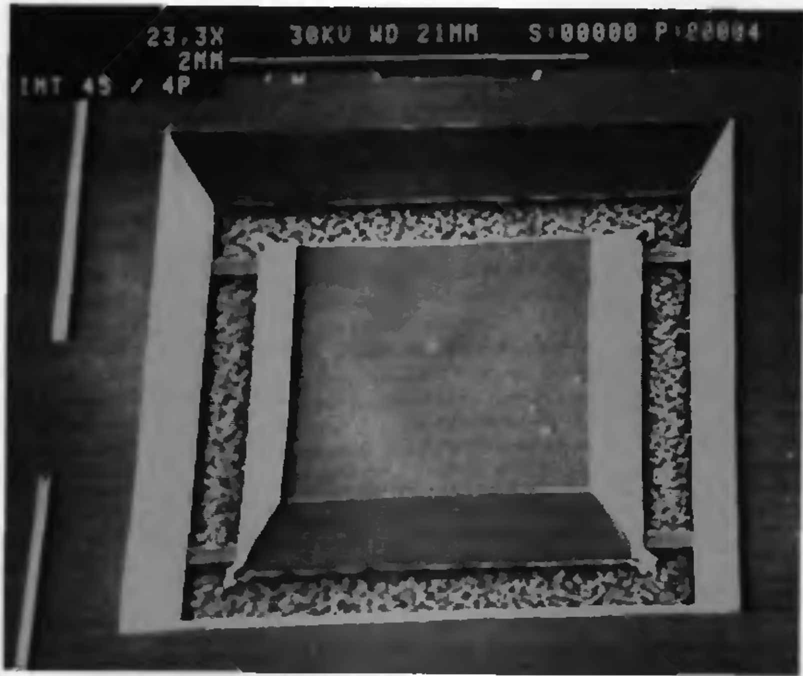

Fig. 3.3.2 Micrograph of an accelerometer with piezoresistive sensor realized with bulk micromachining [18].

References to chapter 3

1. H. C. Nathanson, W. E. Newell, R. A. Wickstrom and J. R. Davis, IEEE Trans. Electron. Devices.14 (3), 1967, pp. 117
2. K. E. Petersen, Proc. IEEE, 70 (5) 1982, pp. 420-457
3. S. M. Sze, *Semiconductor devices. Physics and technology.* John Wiley & Sons1985
4. *Mikromechanik*, edited by A. Heuberger, Springer-Verlag, 1991
5. *Sensor Technology and Devices*, edited by L. Ristic, Artech House, 1994
6. U. Gösele et al., Solid state phenomena, 47-48 (1996) pp. 33-34
7. D. Hülsenberg, R. Bruntsch, K. Schmidt and F. Rheinhold, Silikattechnik 41 (11) 1990, p.364
8. E. W. Becker, W. Ehrfeld, P. Hagmann, A. Maner and D. Münchmeyer, Microelectronic Engineering 4, 1986, pp. 35-56
9. L. Dellmann et al., Proceedings of the Transducers '97 Conference, vol.1, 1997 pp. 641-644
10. D. R. Sparks, S. R. Zarabadi, J. D. Johnson, Q. Jiang, M. Chia, O. Larsen, W. Higdon, P. Castillo-Borelley, Proceedings of the Transducers '97 Conference, vol.2, 1997, pp. 851-854
11. G.-C. Fiaccabrino, PhD dissertation, University of Neuchatel, 1996
12. H. B. Martin, A. Argoita. U. Landau, A. B. Anderson and J. C. Angus, J. Electrochem. Soc. 143 (1996) L133
13. P. Niedermann, W. Hänni, N. Blanc, R. Christoph and J. Burger, J. Vac. Sci. Technol. 14 (1996) p.1233
14. V. P. Jaecklin, PhD. dissertation, University of Neuchâtel, 1994
15. B. Kloeck, S. D. Collins, N. F. de Rooij and R. L. Smith, IEEE Trans. Electron. Dev., ED 36 (4) 1989 p.663

16. Alcatel CIT reactor

17. STS ICP reactor

18. T. Tschan, PhD. dissertation, University of Neuchâtel, 1992

Chapter 4

Microfabricated tips

4.1 Introduction

The tip is one of the most critical components of an SPM sensor. Very high vertical resolution can be obtained with optical, piezoresistive or tunneling detection, whereas lateral resolution depends strongly on the tip shape [1]. Thus, the microfabrication of reproducible tips, if possible with batch techniques, is a challenge for micromachining.

The requirements relative to the material properties change a lot from one SPM tip type to another, but geometrical needs remain the same: high aspect ratio and small curvature radius of the apex. Thus, many fabrication techniques were developed, specially for AFM and SNOM tips, which often have to be integrated on cantilevers.

In this chapter, the most used techniques to fabricate SPM tips will be described. Then, processes which were developed during this dissertation will be discussed. First, the microfabrication of sharp AFM tips with specially well-suited aspect ratio will be described in detail. Then, a technique for local coating of tips will be presented, as well as very promising results for opening small apertures on SNOM tips. Finally, we will show how thick photoresist can be used for tip protection during wet or deep dry etching processes.

4.2 STM tips

As they need not to be integrated on flexible micro cantilevers, STM tips may be fabricated in a very simple way by simply cutting a fine metal wire mechanically. In spite of the coarseness of the tips so obtained, they very often present some micro protrusions which allow tunneling detection with acceptable resolution. To improve the reproducibility of the tip shape, electrochemical etching methods were developed [2, 3].

A critical aspect of STM tip fabrication is the material used. As electrons should tunnel through the gap between tip and sample, any oxide layer on the tip is undesirable. For this reason, only metals like tungsten, gold or platinum-iridium can be used. The electrochemistry of such materials implies the use of strong chemicals, which makes the integration of electrochemically etched STM tips difficult.

4.3 AFM tips

There are many ways to obtain sharp tips integrated on cantilevers: by deposition of material [4, 5], by focused ion beam (FIB) milling [1], by molding, or by etching. Most of the commercially available AFM tips are currently produced by molding or by etching techniques, because they are relatively easy to integrate in batch fabrication processes. Fig. 4.3.1 illustrates these two basic techniques.

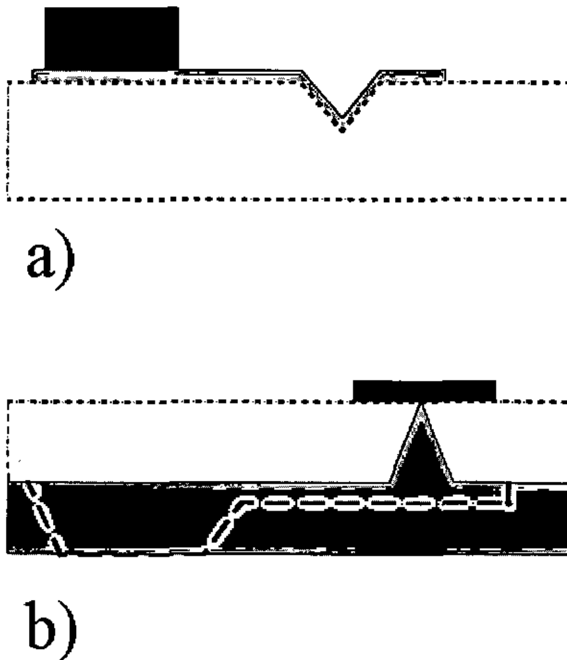

Fig.4.3.1 Two main fabrication techniques for sharp tips integrated on cantilever beams: a) by depositing and patterning a material in a silicon mold b) by silicon underetching.

Molded tips are generally formed from a negative pyramidal, anisotropically etched silicon pit into which nitride [6], metal [7] or diamond [8] is deposited (Fig. 4.3.1 (a)). In this technique, the <111> silicon planes act as an etch stop and make the pyramidal mold easy to create. The tip is protected until the end of the process by the silicon bulk, which allows the cantilevers to be patterned with high precision. Low temperature oxidation sharpening of the mold allows the formation of very sharp tips [9]. The drawback of this technique, however, is that the tip is formed with the point down inside the bulk silicon. This means that a thick layer has to be grown or bonded on the wafer to support the structures after the removal of the silicon mold. This is straight forward for metal tips but may require some additional technological steps for nitride or diamond.

Recently, a double molding technique has been developed which allows the realization of molded platinum tips with high aspect ratio and very small radius of curvature [10].

Tips may also be formed by wet or dry underetching of silicon [11, 12] (Fig. 4.3.1 (b)). The wet etching technique utilizes the selectivity of KOH etching with respect to the crystalline planes of monocrystalline silicon. By correctly choosing the mask design (usually a disc), the selective underetching of silicon induces the intersection of crystalline planes at one point. Fig. 4.3.2 shows a typical tip realized with this process. The main advantage of this technique is that it does not need a very precise etch time control: in case of overetching, the tip decreases in height, but it remains sharp [13]. Another advantage is that very large arrays of sharp tips may be produced in this way. Finally, the height of the anisotropically wet etched tips may vary from less than ten micrometers to more than hundred without changing the aspect ratio, just

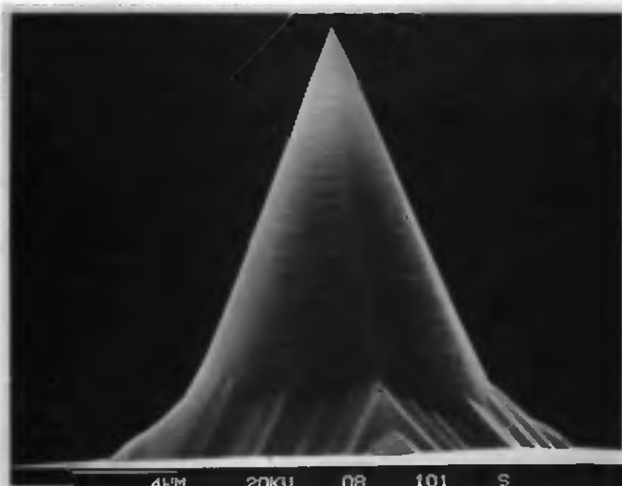

Fig.4.3.2 SEM micrograph of a typical anisotopically wet etched tip

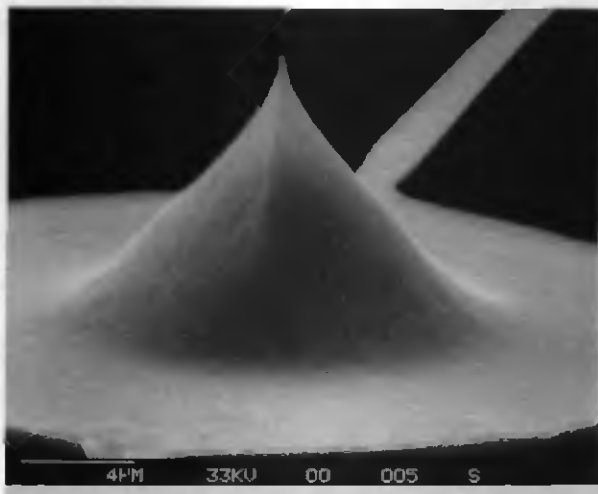

Fig. 4.3.3 SEM micrographs of a silicon tip formed with dry etching and wet etch polishing.

by adjusting the initial mask dimensions. The disadvantage of this technique is the use of KOH at a very early step of the fabrication process. The increase in wafer surface roughness or the risk of contamination may impede further technological steps like transistor implantation.

Isotropic dry etching is used in a similar way: a circular cap of oxide, metal or photoresist is patterned on the silicon surface. Underetching of silicon is then responsible for the formation of the tip shape. The drawback of this technique is that the aspect ratio of the tip is difficult to control, and that the dry etching rate is usually higher at the edges of the wafers than in the center. This may lead to the overetching of the central tips and, hence, to an increased radius of curvature. Isotropic wet etching may be used at the end of the dry process to polish the silicon surface [12]. Apex curvature radius may be reduced by performing a low temperature oxidation sharpening [14]. Fig.4.3.3 shows an example of a tip produced by dry underetching and wet etch polishing.

4.4 SNOM tips

The first SNOM tips were directly fabricated by tapering an optical fiber and coating it with a thin aluminum film at an angle relative to the fiber axis [15]. If the fiber is rotated during the metal evaporation, the sides are well coated but the very top remains open. The drawback of this technique is its incompatibility with batch production processes and its low reproducibility.

Simultaneous AFM and SNOM imaging can be performed with silicon nitride cantilevers fabricated by the molding method [16]. This is an important improvement because it allows the optical sensor to be maintained at a constant distance from the sample by means of the AFM principle. AFM cantilevers with integrated photodetectors have also been fabricated [17]. To do this, a silicon cantilever with integrated tip is fabricated. Then, an insulating layer is deposited or grown and etched on top of the tip. Finally, a thin metal layer is evaporated and etched on the apex. The aluminum contact with silicon is utilized as a Schottky diode to detect light intensity.

In all the processes described above, the critical point of SNOM tip fabrication is to open in a reproducible way a small aperture at the end of the tip. Small means here 100 nanometers or less. Focused ion beam can be used for this purpose. This method shows good results, but is not adapted to batch fabrication. R. C. Davis and coworkers [17] used the fact that an exposed tip emerging from a photoresist layer can be etched. This method is interesting because it requires no lithographic step. However, the resolution achieved so far is only in the range of a few hundreds nanometers.

4.5 Stylus-like dry etched AFM tips

One of the problems of dry etched AFM tips is their relatively low global aspect ratio. This means that even if the last two or three micrometers at the tip extremity have a very good shape (aspect ration up to ten [18]), the accessibility to the tip may be difficult due to the low global aspect ratio of the whole structure. One way to cope with this drawback is to form the tip at the end of a column. An additional advantage is that this design increases the moment induced by lateral forces on the cantilever. Thus, the sensitivity of friction force measurements is improved.

A two-step dry etching process was developed, in which the end of a column, formed during the first step, is etched to a sharp tip with high aspect ratio during the second step. These tips could easily be integrated on cantilevers by using SOI wafers as substrate. The second etch step is then employed to simultaneously form the tip and define the cantilever's shape, while the buried oxide serves as etch stop for a precise definition of cantilever thickness. The fabrication sequence for such tips is described in Fig. 4.5.1. Etching steps were performed in parallel plate reactors with 13.56 MHz RF generators (Leybold Z401S) in reactive ion etching (RIE) mode [19].

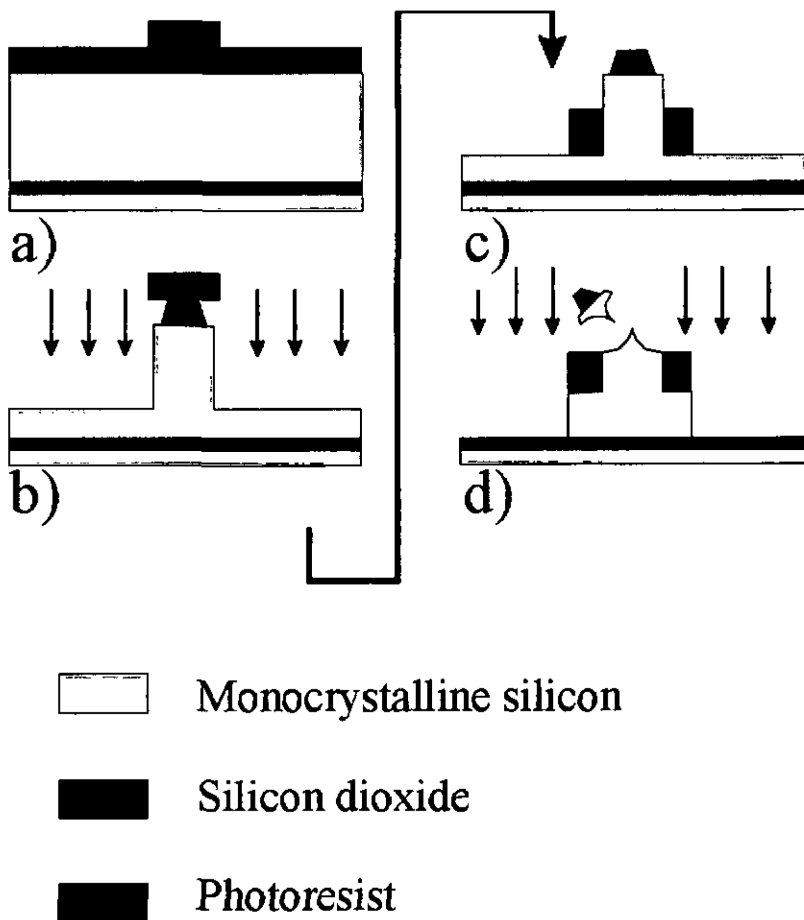

Fig.4.5.1 Fabrication sequence for double dry etching step silicon tips: a) thick oxidation of an SOI wafer and patterning of a thick photoresist layer; b) first dry etching step to form the column and reduction of oxide caps on the top of them with BHF etching; c) after stripping the first photoresist layer, a second thick photoresist layer is spun and patterned (cantilever shape and protection of the base of the columns); d) second dry etching step to form the tips and define the cantilevers.

First, a 1 μm thick oxide layer is grown on an SOI wafer. Then, circular caps are patterned in a thick photoresist layer (AZ 4562, 8 μm) (a). BHF etching is performed to pattern the oxide, followed by the first deep dry etching step to form 10 to 15 μm high columns. This first step is realized with a chlorine / fluorine gas mixture (C_2ClF_5/SF_6). The dimension of the remaining oxide caps on the top of the silicon columns is reduced by BHF etching (b). After stripping the first photoresist layer, a second thick photoresist layer is spun and patterned to define the cantilevers and to protect the base of the columns (c). A second RIE step is then performed with a fluorine / oxygen gas mixture (SF_6/O_2). The stronger underetching effect of this gas mixture is responsible for the final tip shape. At the same time, cantilevers will be defined in the remaining upper silicon layer of the SOI wafer. The buried oxide layer, which is used as an etch stop, allows good uniformity in the cantilever thickness.

Fig. 4.5.2 a) and b) show SEM micrographs of such a tip. Its height is about 7 μm and the diameter of the column is about 2 μm. Note the polishing effect of the second dry etching step and the good profile of the tip. The curvature radius of the apex is estimated to be about 10 nm. Additional low temperature oxide sharpening could be performed if smaller values are needed.

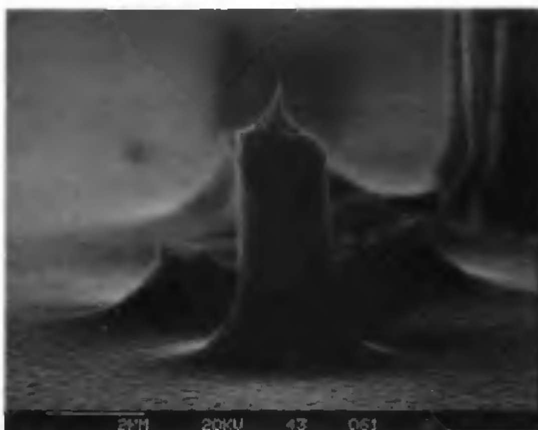

a)

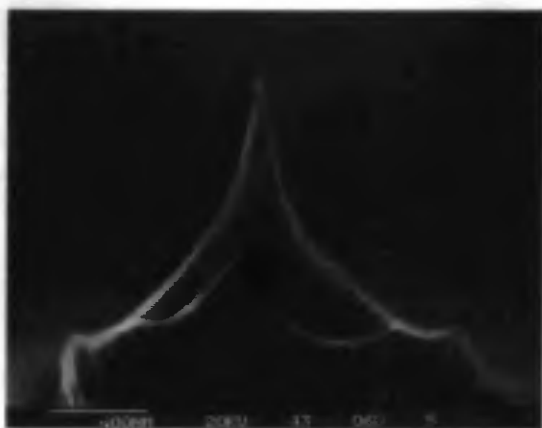

b)

Fig. 4.5.2 a) SEM micrograph of a dry etched stylus tip; b) Close-up view of the upper part; curvature radius of the apex is estimated to be about 10 nm.

4.6 AFM tips locally coated with diamond

One of the major drawbacks of sharp silicon tips is their great fragility. Future applications like very high density memory systems, where large arrays of tens or even hundreds of tips will operate in parallel, will require reliable tips and cantilevers with acceptable lifetimes. The destruction of individual tips will then be unacceptable, because this would mean loss of stored data or oblige the system to perform redundant reading, implying loss of time. Very resistant material like diamond was used to fabricate cantilevers with integrated molded tips, and results are very promising [8, 20].

Another solution consists in coating only the most exposed parts of the tip with diamond. This technique may be useful when diamond tips have to be integrated on silicon cantilevers with other actuating or sensing elements; it is illustrated in Fig. 4.6.1. Silicon tips, which were previously selectively etched in KOH, were used to do this. After tip forming, the wafers were oxidized and a thick photoresist layer (about 8 μm) was spun. The salient part of the tip was then etched in BHF, the photoresist removed and a CVD diamond film was selectively deposited on the oxide free surfaces [21]. During the diamond deposition, the remaining oxide is destroyed. Fig. 4.6.2 shows a silicon tip with its diamond coated upper part. Some isolated diamond grain due to spontaneous nucleation can also be distinguished.

Chemical inertia is another interesting property of diamond, which can be utilized in microfabrication processes as masking material. A 20 minute RIE test in a C_2ClF_5/SF_6 gas mixture gave excellent results: no alteration of the surface could be observed in the SEM. This time would correspond to an etched depth of about 10 μm in silicon.

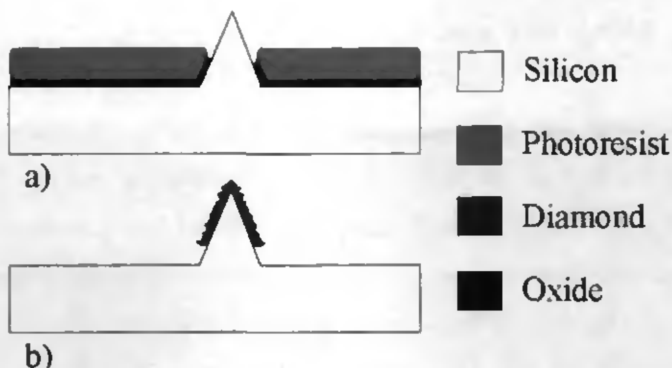

Fig.4.6.1 Locol diomond coating of silicon tips: a) etching of the tips in KOH, oxidation of the wafer, deposition of a thick photoresist layer and removing of the oxide on the solient part of the tip with BHF; b) diamond is CVD deposited on the oxide free top of the tips. Remaining oxide is destroyed during the diamond deposition.

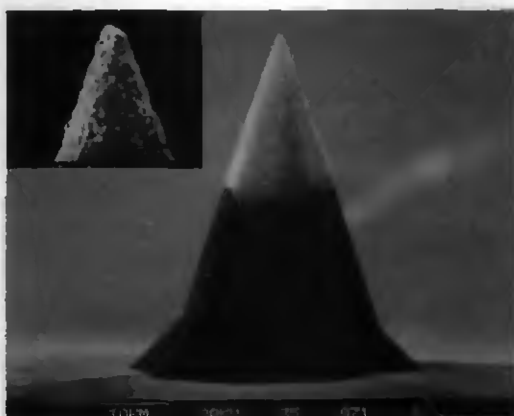

Fig. 4.6.2 Silicon tip with local diamond coating. Scale bar of the opex close-up view is 1 μm.

4.7. SNOM tips fabrication

As already mentioned, there are different ways of making SNOM tips, but they all have to solve the same problem: the etching of a small aperture in the upper metal coating. We present here a technique which allows the opening of small holes or trenches in a thin metal layer at the top of silicon tips. This technique is interesting because it doesn't require any lithography and is compatible with batch processing. The basic idea is to integrate a Schottky diode on the tip [17], and to use the tip effect due to the electrical field in a RIE chamber to open the metal layer.

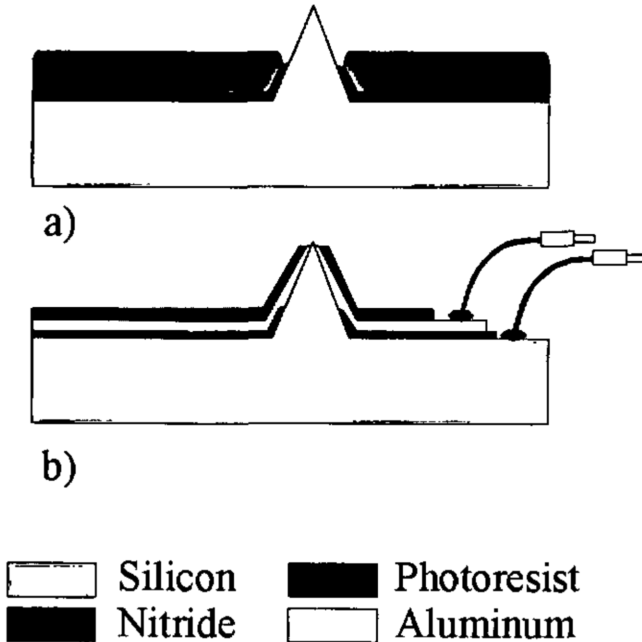

Fig. 4.7.1 Fabrication process for SNOM tips with integrated Schottky diode

The fabrication process is illustrated in Fig. 4.7.1. On a tip which was previously selectively wet etched in KOH, a layer of PECVD nitride is deposited and removed on the top of the tip with the same technique as described in section 4.6. PECVD nitride may be etched with BHF. Then a 50 nm thick aluminum layer is evaporated and covered with a second PECVD nitride layer. This nitride layer is then etched from the very top of the tip in a RIE process by exploiting the tip effect in the plasma. Aluminum is then etched by using the nitride as masking material and contacts are opened with thick photoresist lithography (to protect the structure on the tip).

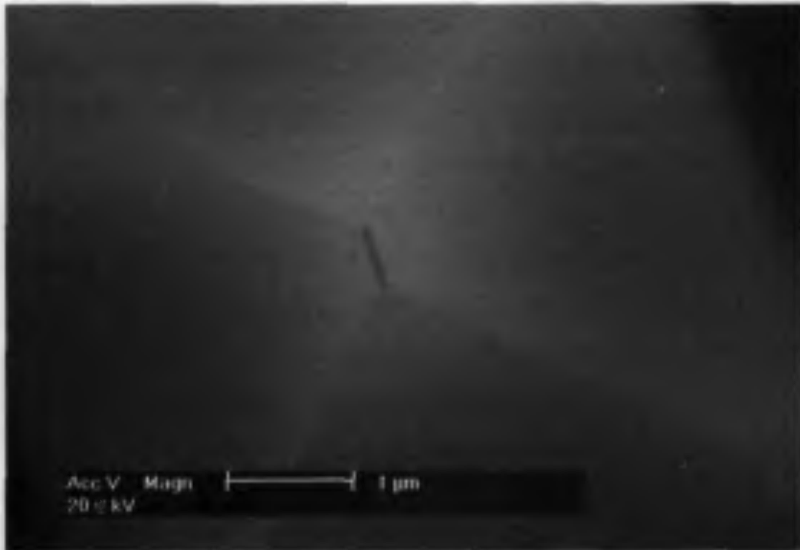

Fig.4.7.2 Top view of a nitride aperture realized by utilizing the tip effect in RIE on a knife shaped tip. Trench is about 500 nm long and 70 nm wide.

This allows the realization of regular holes on tips or trenches on edges. Fig. 4.7.2 shows a top view of a knife-shaped silicon tip covered with PECVD nitride. The nitride was dry etched on the apex by exploiting the tip effect in RIE. The length of the trench is about 500 nm, width is about 70 nm. Fig. 4.7.3 a) shows a side view of a silicon tip coated with a 50 nm thick aluminum layer and a 100 nm thick PECVD nitride layer after nitride etching on the apex. The same tip after aluminum etching is presented in Fig. 4.7.3.b). One can clearly distinguish that the metal protuberance at the top in picture a) has disappeared in picture b). The hole in the metal created in this way is estimated to be about 70 nm in diameter. SEM observation of various tips showed a good reproducibility of this etching technique. Furthermore, knife-shaped tips with linear apertures could be useful for studies with polarized light. These tips were realized in collaboration with G. Schürmann, as a part of his thesis work.

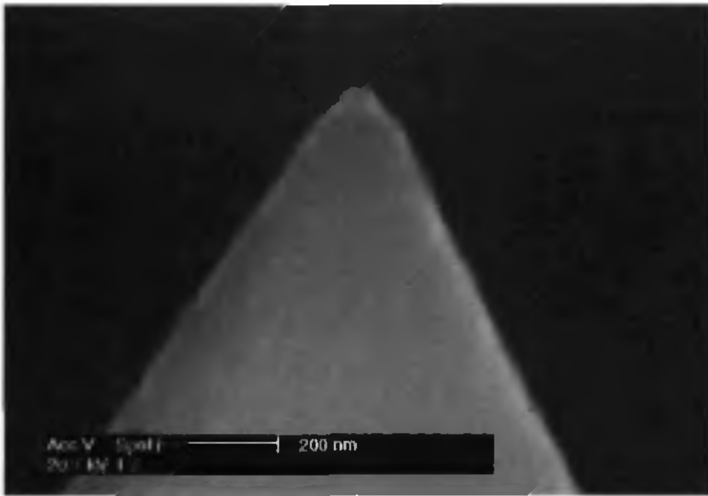

a)

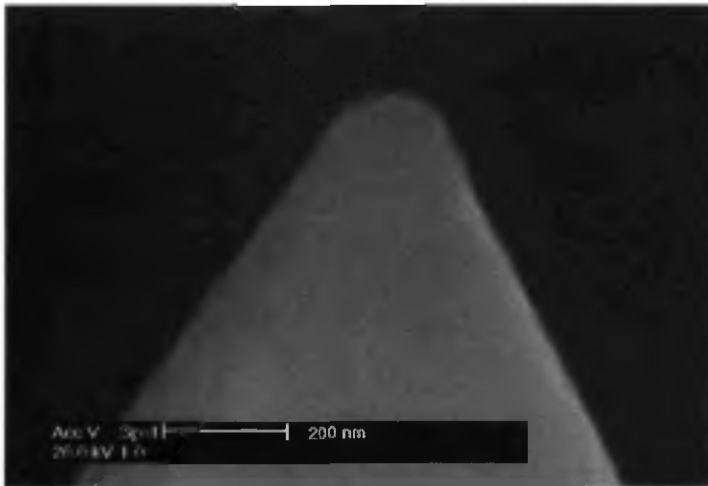

b)

Fig. 4.7.3 Side view of the apex of a tip: A) after nitride dry etching b) after aluminum wet etching. Diameter of the optical aperture is estimated to be 70 nm

4.8 Protection of tips during wet and dry etching processes

In SNOM and some other applications like biological sensors on perforated silicon membrane [22], tips need to be coated with one or more layers and then be protected during dry or wet etching steps which have to be performed after their formation. We present here a technique using a patterned thick photoresist layer to protect the tips during wet and dry etching processes [23]. Shown schematically in Fig. 4.8.1, this technique can of course be extended to other kinds of protruding structures which have to be protected.

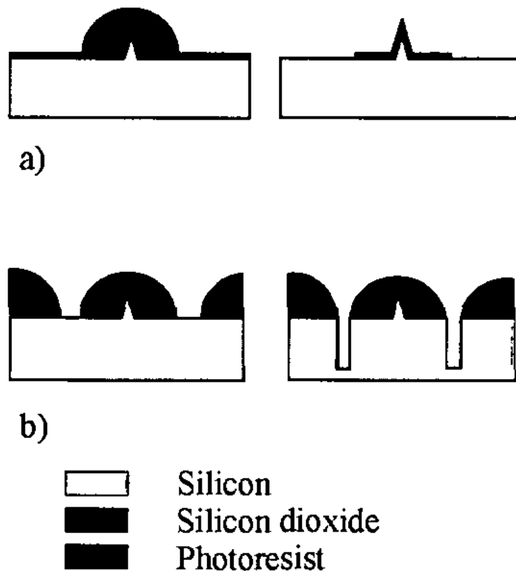

Fig. 4.8.1 Patterned thick photoresist protection of sharp tips a) during wet etching b) during dry etching steps.

A thick photoresist layer was spun on wafers with KOH-etched silicon tips. Height of the tips were 15 and 25 μm. A Karl Süss RC8 Spin Coater spinner and AZ-4562 photoresist were used. A pre-bake step was then performed on a ramped hot-plate and patterning was realized with a commercial mask aligner (Al-6, Electronic Vision). Development was done in an AZ-400 K (1:3) solution. A post-bake step was performed to polymerize the photoresist and to avoid degassing during the dry etching experiments. Fig. 4.8.2 shows a photoresist hemisphere after post-baking. The tip is inside, but can't be seen because of the metal coating deposited to improve the quality of SEM image.

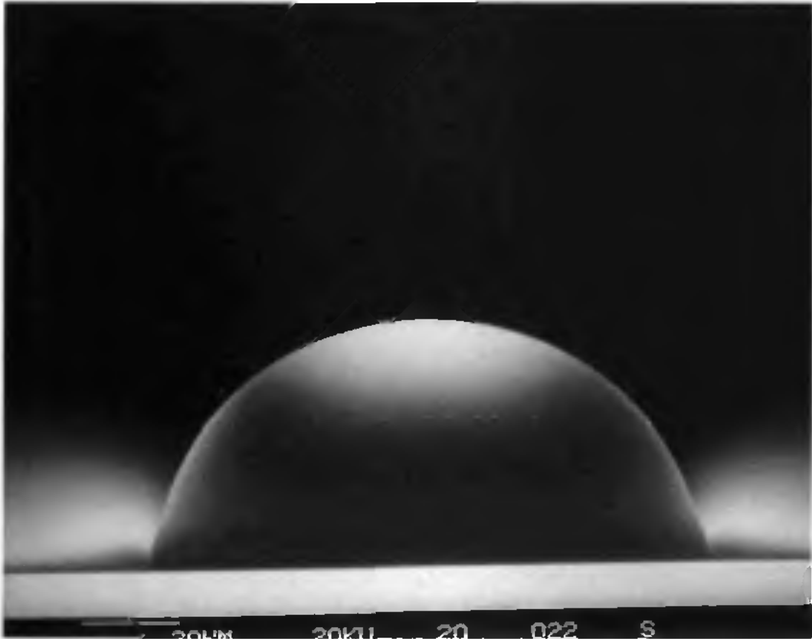

Fig. 4.8.2 Silicon tip hidden in a photoresist hemisphere. Scale bar is 20 μm

Wet etching was then performed in BHF and dry etching was done in an STS ICP reactor in RIE mode. In the first case, the tips were perfectly protected and no damage to the apexes could be observed. In the second case, the biggest tips were slightly etched, while the smallest ones were well protected. Fig. 4.8.3 shows an oxide-coated tip in the center of an oxide disc. In Fig. 4.8.4, a tip on a 65 μm high pedestal is presented. In other experiments, trenches with a depth of about 300 μm and a width of about 20 μm were dry etched without damaging the 15 μm tips while the 25 μm ones were again slightly attacked.

As can be observed on Fig. 4.8.2, the post-bake step induced a strong contraction in the photoresist layer and reduced thus the resolution of the patterning. In spite of its low lateral accuracy this technique may be useful for some micromachining applications. For example, profilometer styli with very sharp tips could be produced in this way.

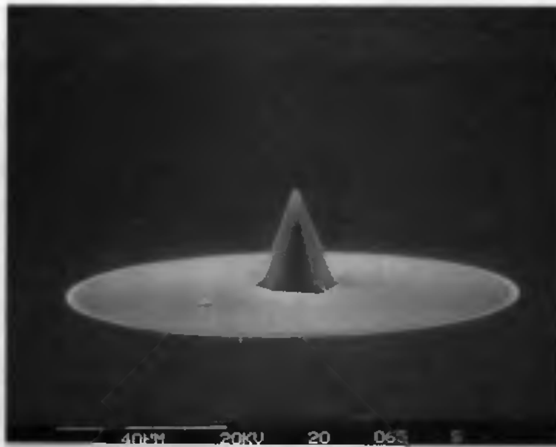

Fig. 4.8.3 Oxidized tip and oxide disc after BHF etching and photoresist removal

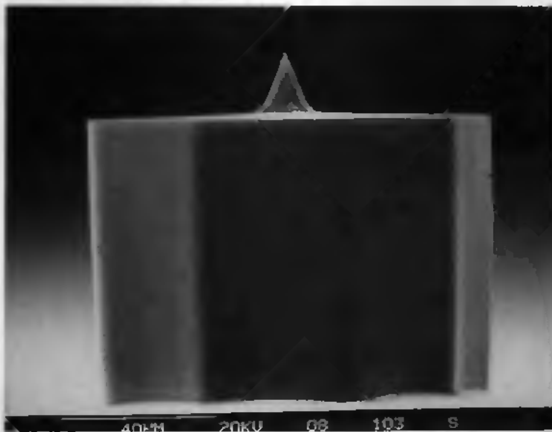

Fig. 4.8.4. Dry etched 65 μm high silicon pedestal with integrated sharp tip on its top.

4.9 Conclusion to chapter 4

A lot of microfabrication techniques have been developed to form AFM tips and to integrate them on force sensors. The most reliable and cheap ones are now used for the mass production of AFM cantilevers. However, the demand exists for improved tip shape or materials to increase the imaging resolution or cantilever lifetime. The stylus-like tips and tips coated with diamond are a contribution in this direction.

Tip formation is only the first step in the realization of SNOM sensors, which then requires very fine patterning of a metal layer on the top of the tip and sometimes the integration of a photosensitive device on the tip itself. We showed that the tip effect due to the electrical field in a plasma reactor can be utilized to define very fine apertures on the apex of metal coated tips.

Finally, a technique using a thick photoresist layer was developed to protect protruding tips during wet and deep dry etching. This allows the integration of sharp tips on high aspect ratio structures.

References to chapter 4

1. J. E. Griffith and D. A. Grigg, J. Appl. Phys. 74 (9) 1993 pp. R83-R109
2. 1. H. Musselman and P. E. Russell, J. Vac Sci. Technol. A 8 (4) 1990, pp. 3558-3562
3. J. P. Ibe et al., J. Vac Sci. Technol. A 8 (4) 1990, pp. 3570-3575
4. T. R. Albrecht and C. F. Quate, J. Vac. Sci. Technol. A 6 (2) 1988, pp. 271-274
5. H. Dai, J. H. Hafner, A. G. Rinzler, D. T. Colbert and R. E. Smalley, Nature 384 (1996) pp. 147-150
6. T. R. Albrecht, S. Akamine, T. E. Carver and C. F. Quate, J. Vac. Sci. Technol. A 8 (4) 1990, pp. 3386-3396
7. J. P. Rasmussen, P. T. Tang, C. Sander,. O. Hansen and P. Moller, Proceedings of the Transducers '97 Conference, Chicago (USA) 1997, pp. 463-466
8. P. Niedermann, W. Hänni, N. Blanc, R. Christoph and J. Burger, J. Vac. Sci. Technol. 14 (1996) p.1233
9. S. Akamine and C. F. Quate, J. Vac. Sci. Technol. B 10 (5) 1992, pp. 2307-2310
10. C. Beuret, P. Niedermann, U. staufer and N. F. de Rooij, presented at the MNE '97 Conference, Athens (Greece) 1997
11. O. Wolter, T. Bayer and J. Greschner, J. Vac Sci. Technol. B 9(1991) p.1353
12. J. Brugger, R. A. Buser and N. F. de Rooij, Sensors & Actuators A 34 (1992), pp. 193-200
13. J.-H. Liu, T. M. Betzner and H. T. Henderson, J. Micromech. Microeng. 5 (1995) pp. 18-24

14. R. B. Marcus and T. T. Sheng, J. Electrochem. Soc.129 (6) 1982, pp. 1278-1282
15. E. Betzig and J. K. Trautman, Science 257 (1992) pp. 189-195
16. N. F. van Hulst, M. H. P. Moers, O. F. J. Noordman, R. G. Tack, F. B. Segerink and B. Bölger, Appl. Phys. Lett. 62 (5) 1993, pp. 461-463
17. R. C. Davis, C. C. Williams and P. Neuzil, Appl. Phys. Lett. 66 (18) 1995, pp.2309-2311
18. J. Brugger, PhD. dissertation, University of Neuchâtel, 1995
19. C. Linder, T. Tschan and N. F. de Rooij, Sensors and Materials, 3 (6) 1992, pp. 311-324
20. P. Niedermann, W. Hänni, D. Morel, A. Perret, N. Skinner, P.-F. Indermühle, N. F. de Rooij and P.-A. Buffat, to be published in Appl. Phys. A, 1998
21. W. Hänni, C. Müller, M. Binggeli, H. E. Hintermann, P. Krebs and A. Grisel, Thin Solid Films 236 (87) 1993
22. P. Thiébaud, N. F. de Rooij, M. Koudelka and L. Stoppini, IEEE Trans. Biomed. Engin. 44 (11) 1997, pp. 1159-1163
23. P.-F. Indermühle, L. Dellmann, S. Roth and N. F. de Rooij, Proceedings of the MME '97 Conference, Southampton (UK) 1997, pp. 39-42

Chapter 5

xy-micropositioner with integrated tip

5.1 Introduction

There are many reasons to microfabricate fully integrated AFM units. First, reducing the size of electro-mechanical components decreases thermal and mechanical noise. Further, miniaturization of AFM devices would allow their integration in other instruments like SEM or their use in outer space. Finally, the batch microfabrication of small, fully integrated units would mean a dramatic price reduction for the AFM sensor part.

Integrated STM units were realized by S. Akamine and coworkers [1] with a multiple piezoelectric layer cantilever, and by Y. Xu and coworkers [2] by using electrostatic micro actuators. The realization of AFM devices is more challenging because of the need to integrate complex detection schemes. S. A. Miller and coworkers [3] demonstrated recently the feasibility of an array of torsional cantilevers with integrated electrostatic actuators and capacitive sensors.

In this chapter, we will discuss the design and simulation of a monocrystalline silicon electrostatic micro positioning unit with integrated sharp tip and via hole for optical detection. The fabrication process will be described, as well as the electro-mechanical characterization of the device. Finally, AFM imaging with this integrated micro stage will be demonstrated and improvements will be suggested.

5.2 Operating principle

Fig. 5.2.1 shows a schematic view of the micro stage. It consists of two beams crossing themselves at their centers where the sharp tip is integrated. The ends of each beam are attached to electrostatically driven comb actuators. Four actuators are necessary because they can only be used in pulling mode [4, 5]. The actuation of two of the four interdigitated combs allows a positioning of the tip in the xy plane.

The combs are electrically isolated from the substrate by a silicon dioxide layer. The drive voltage is applied to pads which are not connected with the tip, so that perturbations due to electrostatic effects are kept as small as possible. Further, the substrate wafer has been etched through, leaving the micro stage overhanging a via hole. Thus, the vertical displacement of the scanned probe can be optically detected.

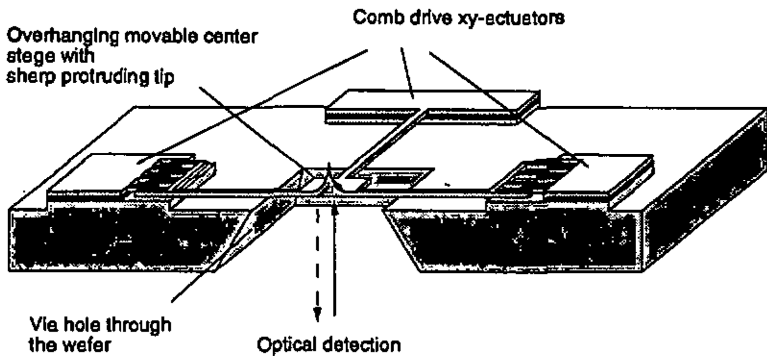

Fig. 5.2.1 Schematic view of an overhanging xy-microactuator with integrated, sharp, protruding tip and via hole for optical detection.

5.3 Structure design

In SFM microscopy, the micro stage has to satisfy various conditions. For the described structure, the following three requirements are the most important. First, the first mechanical resonance frequency has to be high enough (>10 kHz) to extend beyond the noise range. Secondly, the beams of the cross must have a low vertical spring constant in order to be sufficiently sensitive (flexible) to atomic, electric or magnetic forces which are typically of the order of 10^{-9} N. Finally, the horizontal spring constant (in the xy plane) has to be small to enable an electrostatic actuation by the combs.

To estimate the vertical spring constant of the cross, we assumed that the ends of the beams are fixed (an estimation of the contribution of the comb suspensions to the vertical stiffness of the micro stage is rather complex). Further, we assumed that the spring constant of a cross with beams having a width w is the same as that of a beam with twice the width 2w.

Using these assumptions, the first resonance frequency of the cross for free vibrations perpendicular to the substrate (z direction) can be calculated as follows [6]:

$$f_1 = 1.03 / L^2 (Eh^2/\rho)^{1/2} \qquad (5.3.1)$$

where ρ is the density of the material (2300 kg/m^3 for silicon), L and h are the length and the thickness of the beams, respectively, and E the Young's modulus of the material (assumed to be $1.7\ 10^{11}$ N/m^2 for silicon). If the beams of the cross have a length of 750 μm and a thickness of 2.5 μm, a value of about 38 kHz is found, which is beyond the noise.

With the same assumptions as above, the vertical spring constant of the cross, c_z is calculated employing the following expression [7]:

$$c_z = 16\ Eh^3 2w/L^3 \qquad (5.3.2)$$

where w is the width of the beams. With the values mentioned above and w = 3 μm, the vertical spring constant becomes 0.3 N/m, leading to a vertical displacement of a few nanometers for an applied force of 10^{-9} N (Hooke's law), lying thus within the sensitivity range of optical detection systems.

In a similar way, the horizontal spring constant of one beam of the cross in x direction c_{xb} is estimated:

$$c_{xb} = 16\ Ew^3 h/L^3\ . \qquad (5.3.3)$$

Using the values mentioned above, a result of 0.43 N/m is found.

For the horizontal stiffness of the comb suspension c_{xs}, the following formula is employed [16, 17]:

$$c_{xs} = 2Ew^3 h/l^3 \qquad (5.3.4)$$

where l denotes the length of a beam element, two of which form a folded suspension, and E, h and w are the same as defined in eqs.5.3.1 and 5.3.2. For l = 200 μm, a comb suspension stiffness of 2.9 N/m is obtained.

The total horizontal spring constant of the structure sketched in Fg.5.2.1 can then be calculated. Since the suspensions of the active and passive comb actuator and the deflected beam are assumed to have their

ends fixed, they can be considered as three springs connected in parallel. Thus, the resulting total spring constant becomes:

$$c_{tot} = 2c_{xs} + c_{xb} \, . \qquad (5.3.5)$$

For the described structure, we find a value of 6.23 N/m. These values have to be compared with the force created in the combs. For small displacements, this force is given by [5, 8]:

$$F_c = nh\varepsilon V^2/g \qquad (5.3.6)$$

where n is the number of fingers, ε is the permitivity of the air gap, V the applied voltage and g the gap between the fingers. For a driving voltage of 30 V a value of 0.14 μN is obtained, which would allow the micro stage to be moved about 23 nm, while a displacement of 1 μm would require a 6.2 μN force and a voltage of 220 V. Larger displacements at lower drive voltages are achieved for instance by increasing the flexibility of the beams. From eqs 5.3.3 and 5.3.4 it can be seen that a large flexibility is obtained when the beam lengths of cross and comb suspensions are increased or when the width of the beams is diminished. An increase in beam thickness leads to a larger electrostatic driving force (see eq.5.3.6) which, however, is compensated by a lower flexibility of the beams (see eqs. 5.3.3 and 5.3.4). In addition, an enhanced stiffness in the z direction results from an increased beam thickness (see eq. 5.3.2), lowering the sensitivity. In conclusion, a compromise between features like high sensitivity or low drive voltage has to be found by choosing an appropriate structure design. Furthermore, recent developments in dry etching

techniques may allow the achievement of different etch depths for the beams and suspensions and for the comb actuators [9], making possible much larger displacements for a given voltage.

Finite elements simulations were performed with the Ansys® program. The geometry of the device was slightly simplified by ignoring the comb. Static analysis was used to determine vertical and lateral spring constants, while dynamic mode analysis computed the first resonant mode of this rather complex structure. For the values used above, the first resonant frequency was found at 14.2 kHz, which is in the same order of magnitude as our rough model. Fig.5.3.1 shows this first vertical resonant mode.

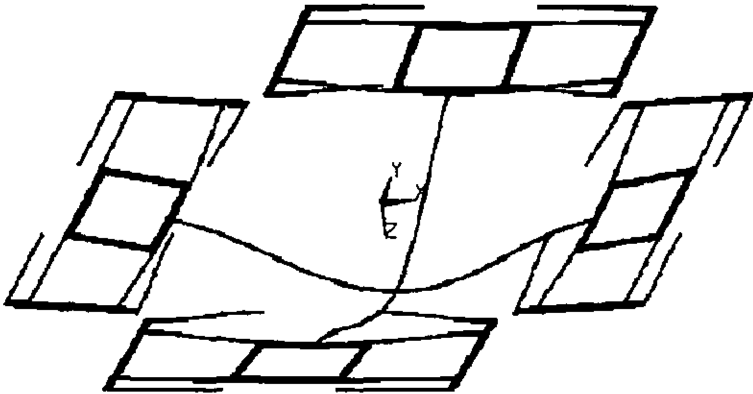

Fig. 5.3.1 Ansys® simulation of the first resonant mode of the xy micro stage at 14.2 kHz (see text for structure dimensions)

The lateral spring constant was found by applying four forces of 0.25 μN on one comb frame and by dividing this force by the obtained displacement (Fig. 5.3.2). A maximum value of 0.22 μm in the x direction was found, leading to a lateral spring constant of 4.5 N/m, which

represents a discrepancy of about 30 percent with the value estimated with our simple model. Another interesting result of this simulation step is the small coupling of the x and y direction motions. A 0.22 μm displacement in the x direction induced a translation in the y direction of 0.26 nm only, which gives a ratio of about 1 to 1000. This value is in good agreement with the one calculated by V. P. Jaecklin [10]. Simulated maximum vertical deviations are again two orders of magnitude smaller and are thus neglectable.

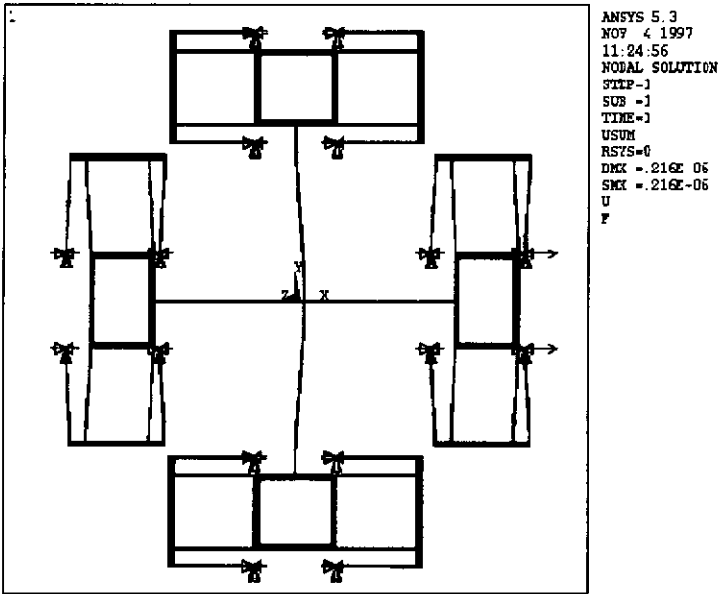

Fig. 5.3.2 Simulated lateral deformation of 0.22μm of the xy micro stage by applying a total force of 1 μN in the x direction

The vertical spring constant was determined in the same way by applying a 1 nN force in the z direction at the intersection of the cross beams. A maximum vertical deflection of 3.4 nm was found, leading to a spring constant of 0.3 N/m, which is in good agreement with the value

obtained with our simple model. For these three simulated values (f_1, c_x and c_z), the simulated values are smaller or equal to the calculated ones. This is a consequence of the fact that in the simple model, degrees of freedom were neglected, thus stiffening the structure.

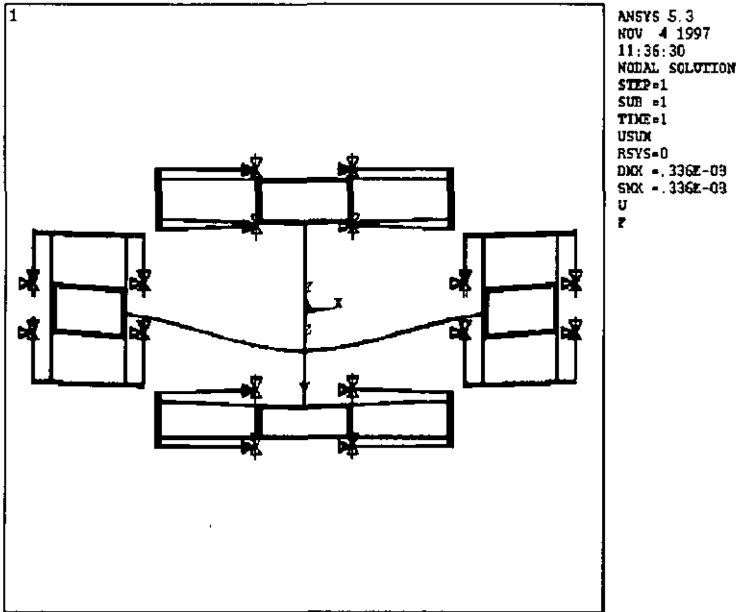

Fig. 5.3.3 Simulated vertical deflection of 3.4 nm of the xy micro stage by applying a total vertical force of 1 nN.

5.4 Fabrication process

The many diverse requirements of the structure presented in Fig. 5.2.1 turn its fabrication into a technological challenge. For example, the presence of a protruding sharp tip impedes the high resolution lithography and dry etching of the cross beams. Comb actuators or the opening of via holes in KOH may destroy the fine silicon structures of the cross. Silicon fusion bonding proved to be an efficient technique to overcome these difficulties. The detailed fabrication process is illustrated in Fig.5.4.1.

Two highly boron-doped silicon <100> wafers with a bulk resistivity of 0.06 Ω cm are used in order to obtain a conductive suspended structure. First, thermal silicon dioxide layers of 0.1 μm and 1 μm thickness are grown on the top and bottom wafer, respectively (a). The oxide of both wafers is then patterned using photolithography and BHF etching (b). On the top side of the lower wafer, this pattern is used to etch a depression with a C_2ClF_5/SF_6 RIE. This depression serves to reduce the sticking of the released structures at the end. On the lower side of the bottom wafer, the pattern will be used as etch mask for the via holes. On the upper wafer, the pattern serves as mask for the subsequent RIE in a C_2ClF_5/SF_6 plasma to prestructure the xy micro stage. The RIE process allows the production of high aspect ratio beams with fairly vertical side walls [5, 11]. Both wafers are then reoxidized to create an etch stop layer for the final KOH and RIE etching steps. After a careful cleaning procedure, high precision double-sided alignment (< 2 μm) on a commercial mask aligner (Al-6 from Electronic Vision) for pre-bonding is performed (c). Then the wafers are sealed together by means of fusion bonding on their SiO_2-SiO_2 contact areas by 4 hours annealing at 1100°C

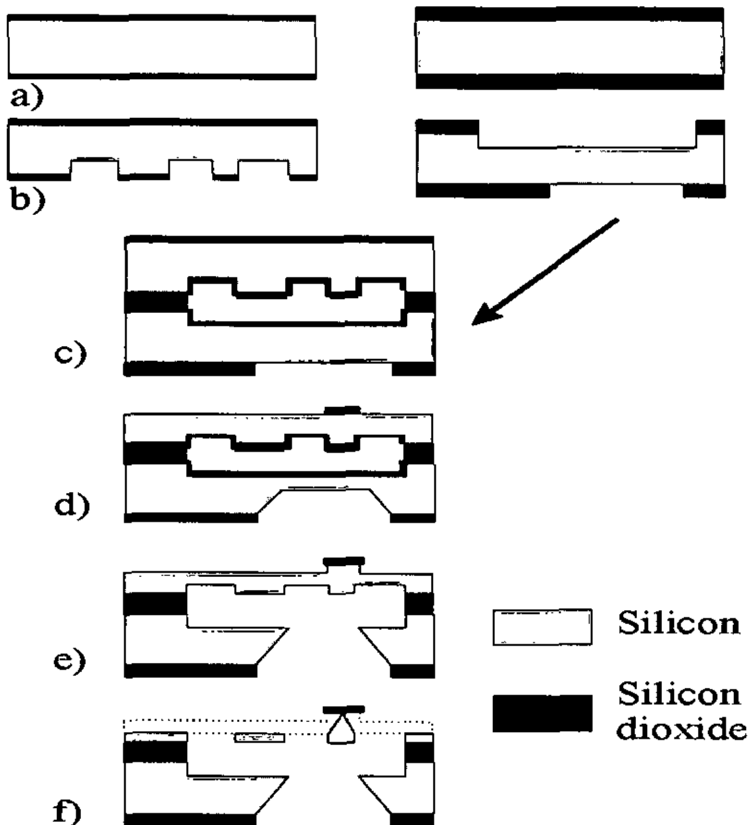

Fig. 5.4.1 Fabrication process for an overhanging xy micro stage with integrated tip and via hole for optical detection. The wafers are first oxidized (a), patterned (b) and reoxidized. Then, they are sealed together with the silicon fusion process (c), and a first KOH etching is performed to thin the upper wafer and partially etch the via hole (d). After oxidation and cap patterning on the upper wafer, the via hole is etched through with RIE (e) and the upper wafer is pierced to release beams and comb actuators (f). At the same time, the tip is formed by underetching of silicon.

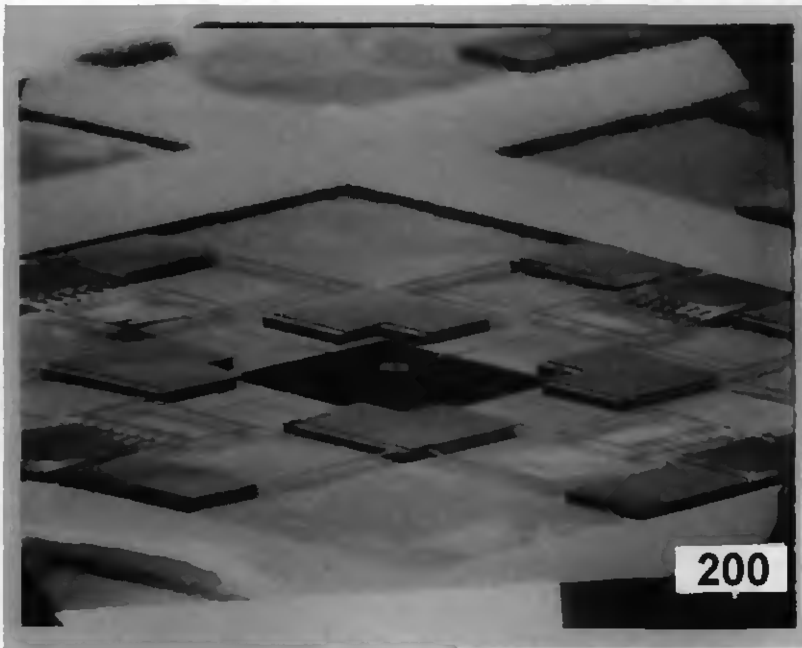

Fig.5.4.2 SEM micrograph of an xy micro-stage with integrated comb actuators, via hole for optical detection and sharp protruding tip. White scale bar is 200 μm.

[12, 13, 14]. In the next step, partial via hole etching of the lower wafer and thinning of the upper wafer are carried out in KOH, until a 25 μm thick membrane remains (d). Afterwards, a 1 μm thick oxide layer is thermally grown. Caps are patterned on the top wafer with lithograpby and subsequent BHF etching. At the same time, the via hole pattern is opened again in the oxide on the bottom wafer. The etching of these holes is achieved in RIE etching, and the original oxide layer of the interface of the wafers, which is now accessible through the via holes, is removed using BHF etching (e). The remaining membrane of the top wafer is finally

pierced through with RIE and tips are formed simultaneously under the SiO_2 caps (f).

Fig. 5.4.2 and 5.4.3 show a top view and a detail of the prototype of such a micro stage, fabricated by means of the described processing sequence. Note the fine beams overhanging the via hole.

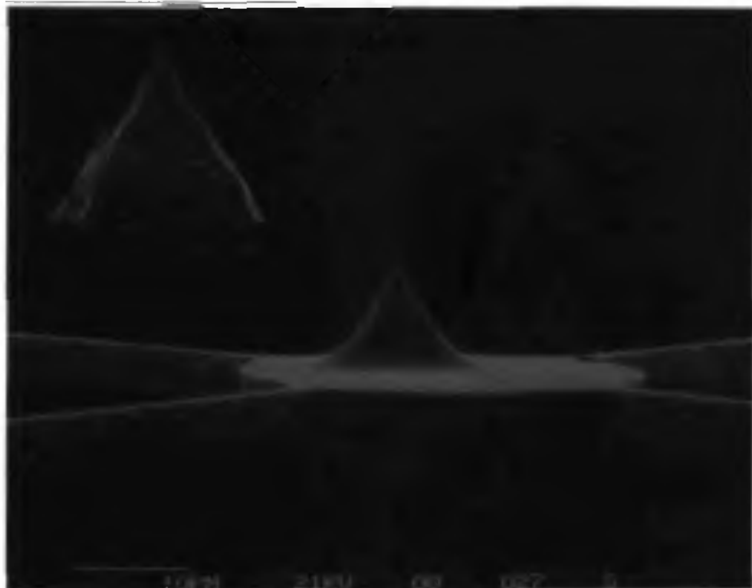

Fig. 5.4.3 Close-up view of the centrol stage with the integrated sharp tip. The scale bar on the top left corner is 1 μm. Curvature radius of the opex is estimated to be less than 70 nm.

5.5 Electro-mechanical characterization

The measured lateral displacement versus applied voltage of a structure whose beams and suspensions were about 2 µm wide and 2.5 µm thick is shown in Fig. 5.5.1. The same data are presented in Fig. 5.5.2 as a function of the square of the applied voltage. They were obtained by applying a dc voltage ranging from 0 to 200 V on one comb actuator and by visually measuring the displacement on the screen of a video camera connected to a microscope. The accuracy of the measurement is $\pm$ 0.5 µm. As expected, the curve shows a good second order fitting [5]. A maximum displacement of 12 µm was observed with an applied voltage of 300 V. Thus, a (2x6) x (2x6) μm^2 scanning area is available by actuating the four combs actuators of an such xy micro stage with 200 V.

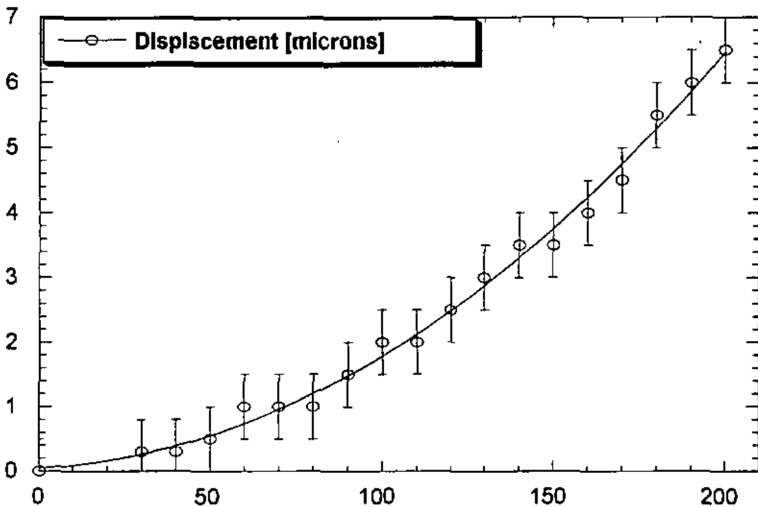

Fig. 5.5.1 Measured displacement versus applied voltage curve of electrostatic actuation of one of the four comb actuators of an xy micro stage with integrated tip. As expected, a good second order fitting is observed (plain curve).

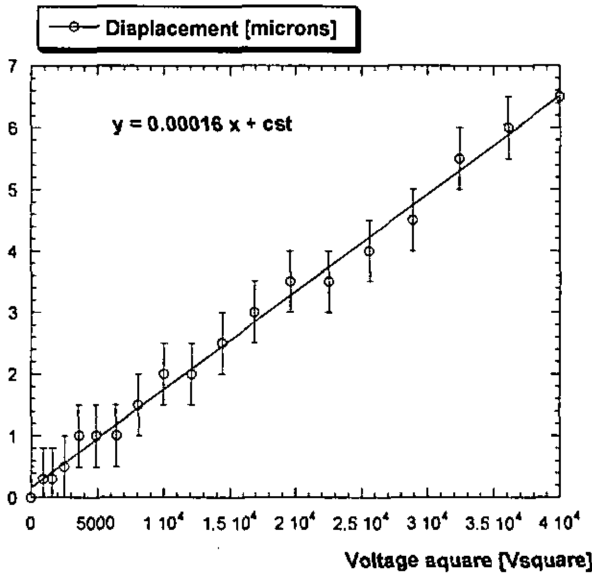

Fig.5.5.2 Measured displacement versus square of the applied voltage for the some data as in Fig. 5.5.1. Error bars are ±0.5 μm. The solid line is the best fit line through the data paints.

Finite element simulation of the structure gave a lateral spring constant of 1.4 N/m. By introducing this value and Eq. (5.3.6) in Hook's law, a value of 0.11 nm/V^2 is obtained, which is significantly smaller than the one of 0.16 nm/V^2 deduced from Fig. 5.5.2 . The same tendency was observed by V. P. Jaecklin and coworkers [5], who attributed this discrepancy to variations in the widths and gap distances of the beams and suspensions.

The same set-up was used to determine the first lateral resonance frequency of the devices. A square signal with an amplitude varying between 0 and 100 V and frequencies ranging from 0 to 30 kHz was applied to the comb. The first resonant frequency of a structure with

beams and comb suspension 2.5 μm thick and 3 μm wide was observed with the microscope at about 16 kHz (Fig. 5.5.3). It was not possible to determine higher lateral modes.

To determine the vertical resonant modes, the devices were glued on a piezoelectric patch and excited by sweeping the frequency of an oscillator. The response to excitation frequencies ranging between 1 and 20 kHz was measured with a confocal microscope and with an interferometer in air and in vacuum (Fig. 5.5.3). The first resonant frequency of the structure mentioned above was found at about 13.5 kHz. This value is significantly smaller than the one obtained with the crude estimation described in section 5.3, but is still higher than 10 kHz. Simulated values were in good agreement with this measurement (see Fig. 5.3.1).

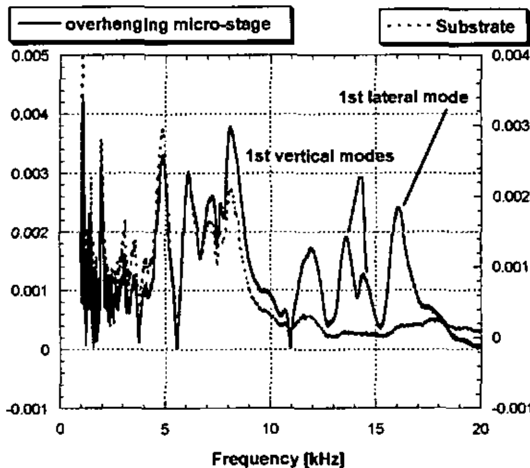

Fig. 5.5.3 Measure of first resonont modes of an xy micro stage with integrated sharp tip and electrostatic comb actuators realized in air with a confocal microscope (units of the vertical axes are arbitrary).

5.6 AFM imaging

Fig. 5.6.1 shows the experimental set-up used to realize AFM imaging with the integrated micro stage. As the bonding pads were on the same side as the tip and close to it, electrical contacts had to be achieved with micro-prober needles. Thus, the accessibility to the scanning tip was seriously reduced and another tungsten carbide prober needle was used as a sample. The alignment of the optical fiber and its introduction into the via hole were achieved thanks to two piezoelectric creeping actuators. The silicon chip with the xy table could be positioned

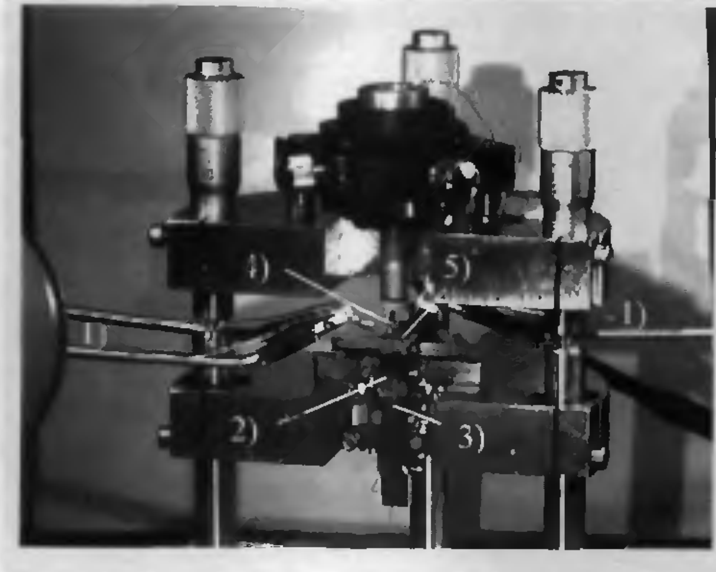

Fig.5.6.1 Set-up for AFM imaging with integroted xy micro-stage. 1) Electric contacts (micro-prober needles) 2) Optical fiber positioning unit 3) Optical fiber 4) Sample (micro-prober needle) and piezoelectric tube 5) Silicon chip with xy table

laterally with the first one, while the optical fiber could be adjusted vertically with the second one. The optical fiber was brought to within a few micrometers from the backside of the central stage of the xy table. Deflection measurements were done by utilizing the interference between the light reflected on the fiber-air interface and on the silicon surface. The sample was fitted on a piezoelectric tube to allow vertical fine adjustment and feed-back actuation during the imaging. Rough alignment was performed thanks to five micro screws. The controller and driving electronics were taken from an Omikron instrument.

Fig. 5.6.2 shows a SEM micrograph of the sample surface which was imaged. Lateral dimensions of the features are estimated to be a few hundreds of nanometers and the vertical range of dimensions less than 100 nm. Fig. 5.6.3 shows the same surface imaged with the integrated xy micro stage in contact mode and with interferometric detection. Lateral and vertical dimensions of the features on the image are in good agreement with the ones of Fig. 5.6.2. Lateral dimensions were deduced from the scanning voltage applied to the comb actuators with help of the curve of Fig. 5.5.1. Vertical scaling was computed from the wavelength of the light (HeNe laser).

In Fig. 5.6.4, an image of the same surface imaged with a commercial instrument (Park Scientific Instrument) is presented. Aspect and dimensions are in good agreement with both images above. The higher noise level observed on the image of Fig. 5.6.3 is due to the poor mechanical stability of the set-up, and possibly also to scan non-linearity. For example, the left corner of the image of Fig. 5.6.3 has a much smoother appearance than the other regions.

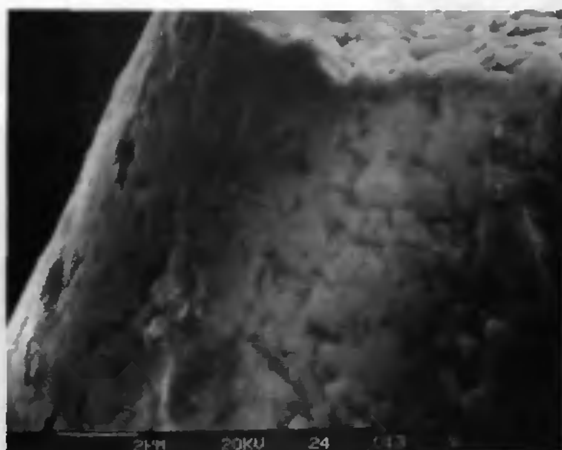

Fig 5.6.2 SEM micrograph of a tungsten carbide needle surface used as sample for AFM imaging with integrated xy micro stage.

Fig. 5.6.3 0.7 x 1 μm^2 contact mode AFM image of tungsten carbide needle surface. The aspect and dimensions of the imaged features are in good in agreement with the SEM view (see Fig. 5.6.2) and the AFM image realized with a commercial instrument of the same surface (Fig. 5.6.4)

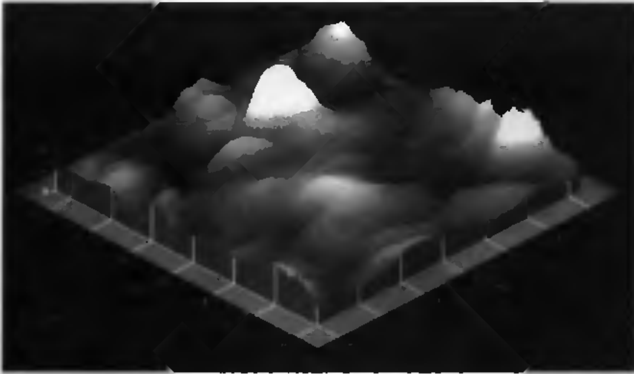

Fig. 5.6.4 1.2 x 1.2 μm^2 AFM image of the same surface imaged in Fig. 5.6.3, achieved with a commercial instrument (Park Scientific Instruments).

5.7 Integration of a large protruding tip on the xy micron stage

The main disadvantage of the integrated xy AFM table is the bad accessibility to the tip, due to the lateral dimensions of the whole stage. Thus, the integration of a larger protruding tip represents a significant improvement. As mentioned in Chap.3, KOH underetching of a silicon dioxide cap allows the formation of high aspect ratio sharp tips with significant height.

To estimate the influence of the large tip mass on the mechanical behavior of the structure, a very simple model was used, in which the torsion in the comb suspensions and their lateral displacement was neglected (see Fig. 5.7.1). It was assumed that the device can be considered as a beam with both ends fixed and with a width twice one of the cross arms. From the measured thickness, width and first resonance frequency of a structure, an "equivalent" length is defined, which is the length that such a simple beam should have in order to show the same first resonance frequency as the cross. The first resonance frequency of such a beam with the mass of the large tip on its center is then used to approximate the resonance frequency of the structure loaded with the large tip.

For example, the measured resonance frequency of a structure with cross arms and suspension beams 3 μm wide and 2.5 μm thick, respectively, and without tip, is 13.5 kHz. The corresponding simulated value is 14.2 kHz (see Fig.5.3.1). We model this as a beam with both ends fixed, with a thickness of 2.5 μm and a width of 6 μm, having its first mode at the same value. Analytically, the first resonance frequency of such a beam is given by [6]:

$$f_1 = 1.03 / L^2 (Eh^2/\rho)^{1/2} \qquad (5.3.1)$$

where ρ is the density of the material (2300 kg/m^3 for silicon), L and h are the length and the thickness of the beam respectively and E the Young's modulus of the material (1.7 10^{11} N/m^2 for silicon). Thus the equivalent length can be expressed as:

$$L_{eq}^2 = 1.03 \, (Eh^2/\rho)^{1/2} / f_1 \qquad (5.7.1)$$

For the values given above, we get 1300 µm. The volume of the tip can be approximated by a cone with a height of 50 µm and a basis radius of 25 µm, giving a volume of about 3×10^{-14} m^3 with a corresponding mass of about 10^{-10} kg. The beam defined above (h = 3 µm thickness, b = 6 µm width and L_{eq} =1300 µm equivalent length), loaded on its center with such a mass M and with a uniform load per unit length w, would have its first resonance frequency given by approximately [6]:

$$F_{1load} = 0.64 \, [Ebh^3 g/(ML_{eq}^3 + 0.383wL_{eq}^4)]^{1/2} \quad (5.7.2)$$

which, in our case, gives a value of about 5 kHz. This is still acceptable for AFM imaging, if the device is used with some damping media. Simulation of the given structure loaded at the intersection of the cross beams with a mass equal to the one of the large silicon tips gave a first resonance frequency at 11.3 kHz which is higher than environmental noise.

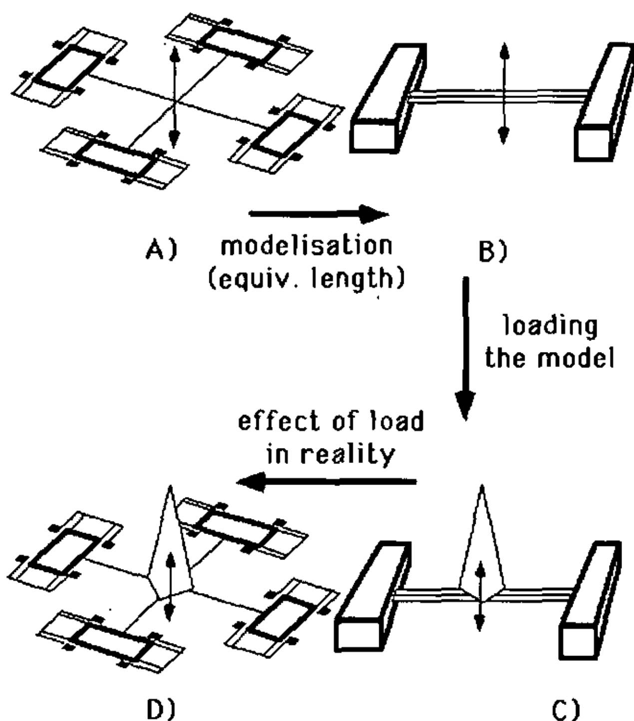

Fig. 5.7.1 Simple beam equivalent length model for an xy micro-stage loaded on its center.

The fabrication process is very similar to the previous one (see Fig. 5.4.1). In step d), the upper membrane is kept 70 µm thick, reoxidized and oxide caps for KOH underetching are patterned. Then, the via holes are finished by RIE and the wafers are sealed in chucks to form the tips in KOH. This KOH etching is stopped a few minutes before the caps fall off, and is followed by a RIE to pierce through the membrane and finish the tip

forming. Fig. 5.7.2 shows an xy micro stage with an integrated high aspect ratio large silicon tip.

The first resonant frequency of such a structure was measured to be at 9.5 kHz (Fig. 5.7.4), which is significantly higher than the value estimated with our crude model but again in fair agreement with the simulation results.

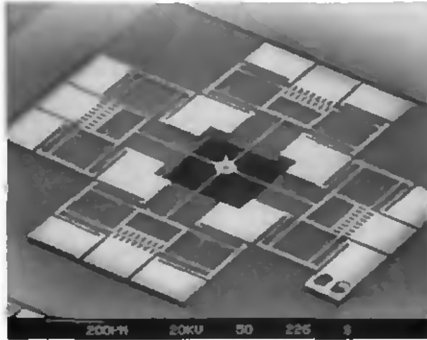

Fig. 5.7.2 Top view of an xy micro stage with integrated large tip with high aspect ratio. The height of the tip is about 50 μm

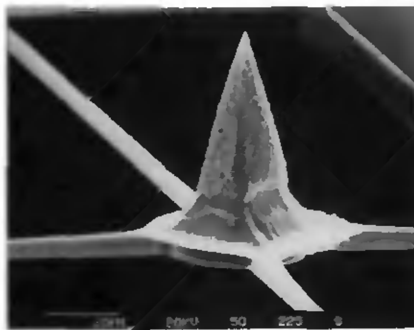

Fig. 5.7.3 Close-up view of the large tip on the center of the stage. The surface geometry is due to the final RIE underetching. Apex radius is smaller than 100 nm.

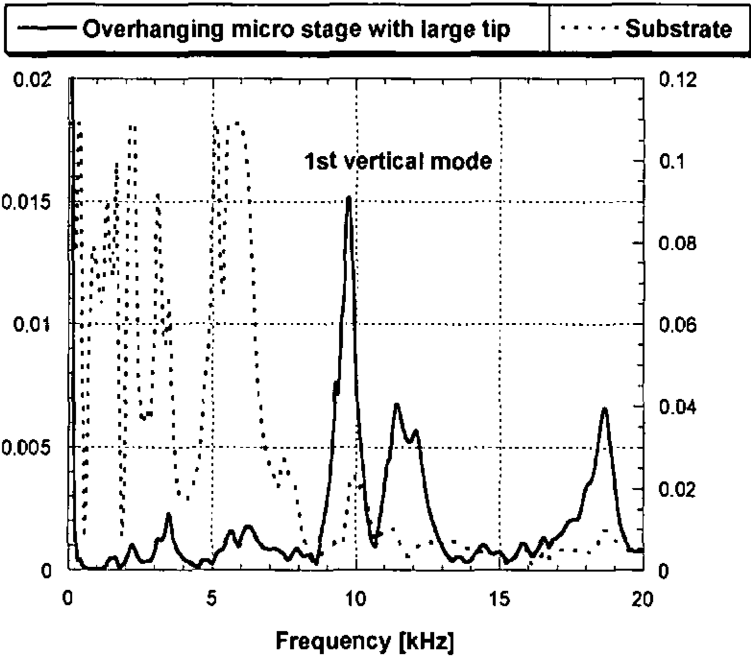

Fig.5.7.4 First resonant frequency of an xy micro stage with integrated electrostatic comb actuators and large silicon tip (units af the vertical axes are arbitrary).

5.8 Discussion and conclusion of chapter 5

A monocrystalline silicon, micromachined xy stage with integrated sharp tip and via hole for optical detection was realized thanks to a combination of the silicon fusion bonding technique and wet and dry etching techniques. The electro-mechanical characterization of the obtained devices revealed that the resonance frequencies of the structures are above the environmental noise value and that scanning areas of some tens of micrometers square are achievable with voltages up to 200 volts. These results fit well the finite element simulations done on a slightly simplified model.

The scanning amplitude could be significantly increased by the use of recently developed deep dry etching techniques (see Chap.3 and [9]). To reduce the variation of the vertical spring constant due to the lateral deformation generated by the scanning, a rigid central frame provided with a flexible cross could be incorporated (see Fig. 5.8.1). The deviation in one scanning direction caused by scanning in the perpendicular direction should be electrically compensated to obtain subnanometer precision positioning.

A very compact design should be achievable by integrating piezoresistive sensors for vertical deflection and capacitive counter reaction actuators. And, last but not least, the new silicon fusion techniques and photoresist electrodeposition should allow backside electrical contacting.

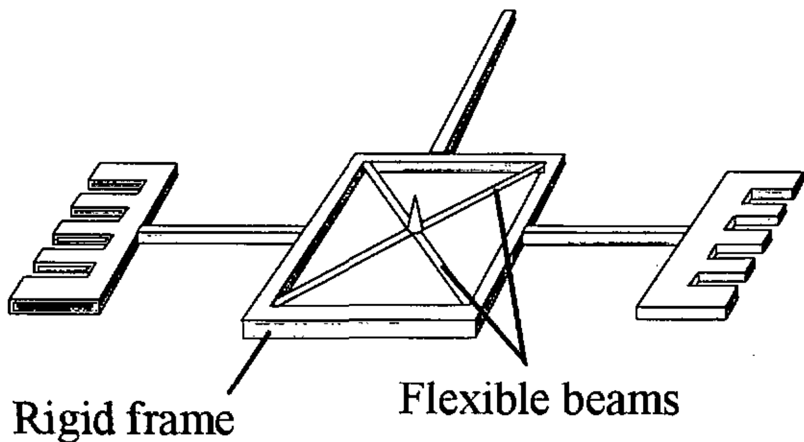

Fig.5.8.1 Cross with central rigid frame and flexible beams to reduce the effect of lateral deformotion due scanning on the vertical spring constant of the verticol force sensor.

References of chapter 5

1. S. Akamine, T. R. Albrecht, M. J. Zdeblick and C. F. Quate, Sensors and Actuators A21-A23 (1990) pp. 964-970
2. Y. Xu, S. A. Miller and N. C. MacDonald, Proceedings of the Transducers '95 and Eurosensors IX Conference, Stockholm (Sweden), 1995, pp. 640-643
3. S. A. Miller, K. L. Turner and N. C. MacDonald, Proceedings of the Transducers '97 Conference, Chicago (USA) 1997, pp. 455-458
4. W.S.N. Trimmer and K.J. Gabriel, Sensors and Actuators 11 (1987) p.189
5. V.P. Jaecklin, C. Linder, N.F. de Rooij and J.M. Moret, J. Micromech. Microeng., 2 (1992) p.250
6. S. Timoshenko, D.H. Young and W. Weaver, *Vibration problems in engineering*, Wiley, New York, 4th edn., 1974, Ch.5
7. R.J. Roark and W.C. Young, *Formulas for stress and strain*, McGraw-Hill, New York, 1986.
8. C. Linder, Ph.D. Dissertation, Institute of Microtechnology, University of Neuchâtel, 1993
9. C. Marxer et al., Proceedings of the MEMS '97 Conference, Nagoya (Japan) 1997, pp. 49-54
10 V. P. Jaecklin, Dissertation, Institute of Microtechnology, University of Neuchâtel, 1994
11. C. Linder, T. Tschan and N.F. de Rooij, Sensors and Materials, 3 (1992), pp. 311-324
12. R. Stengl, T. Tan and U. Gösele, Jap.J. of Appl. Phys.28 (1989) p.1735

13. C. Harendt, H.-G. Graf, E. Penteker and B. Höfflinger, Sensors and Actuators, A21 (1990) p.927
14. J. Brugger, R.A. Buser and N.F. de Rooij, J. Micromech. Microeng., 2 (1992) p.218

Chapter 6

Sharp silicon tips integrated on piezoelectric cantilevers

6.1 Introduction

The operation of many cantilevers in parallel to increase the scanning velocity of AFM imaging is one of the major topics of SPM-related micromachining investigations [1, 2, 3, 4]. Devices with high scanning rates would be of great interest for very high density data storage systems and for automatic wafer inspection in integrated circuit production.

Cantilevers provided with piezoelectric layers were demonstrated to work as self-actuated sensors for AFM [2, 5]. The next step to achieve fully parallel AFM with high lateral resolution is the integration of sharp tips on such cantilevers.

In this chapter, we will discuss the integration of reproducible self-sharpening tips on such piezoelectric cantilevers. First, structure design and the fabrication process will be described in detail. Then, cantilevers will be electro-mechanically characterized and their suitability for AFM imaging in dynamic and contact modes will be demonstrated.

6.2 Structure design and fabrication

Using monocrystalline silicon micromachining, arrays of 5 cantilevers with integrated tip and piezoelectric layer of zinc oxide (ZnO) for actuation and detection (Fig. 6.2.1) have been fabricated. The beams are 700 μm long, 130 μm wide and 10 μm thick. Some other structures with a single lever have also been realized, with beam length varying between 200 and 1000 μm. Two parallel piezoelectric layers have been deposited on some cantilevers to allow friction force measurement [6] (Fig. 6.2.2).

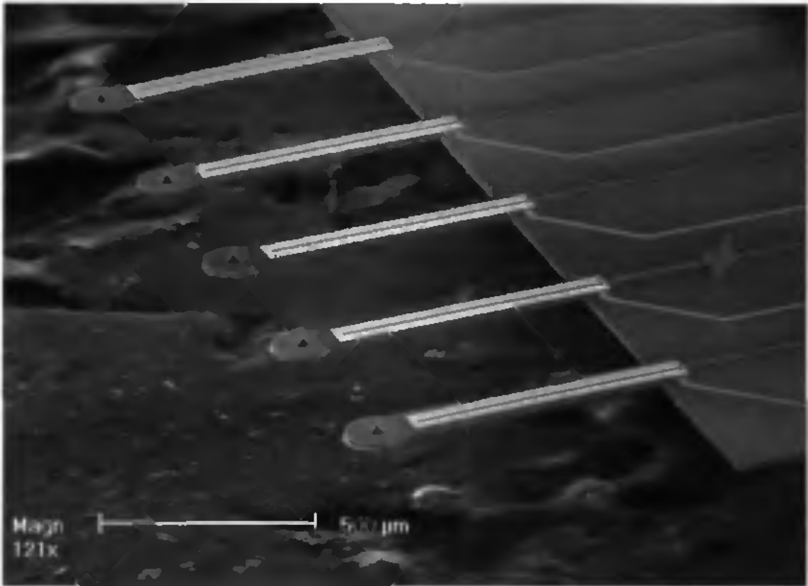

Fig.6.2.1 SEM micrograph of an array of 5 cantilevers with integrated tip and piezoelectric layer for actuation and detection

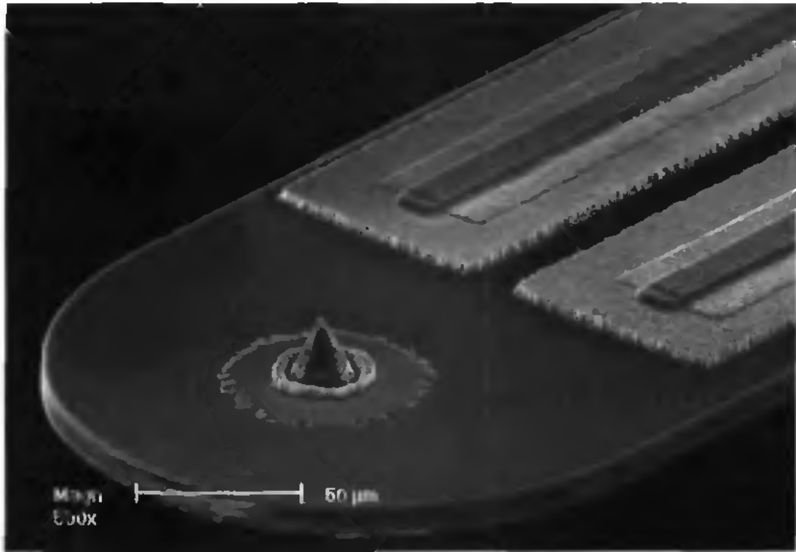

Fig. 6.2.2 SEM micrograph of a cantilever with two parallel piezoelectric lanes and integrated tip. Rings around the tip are etch residues of aluminum and zinc oxide.

At the beginning of the fabrication sequence (Fig. 6.2.3), the wafers are oxidized and covered with a low pressure chemical vapor deposition (LPCVD) nitride layer. The upper nitride is removed (plasma etching) and the lower nitride and the upper oxide are patterned (plasma etching and BHF respectively) (a). The tips are then etched in KOH according to a process developed by Wolter [7] and allowing a good homogeneity in tip sharpness and height, due to a self-sharpening phenomena [8]. Afterwards, the wafers are oxidized for a short time and a thin LPCVD nitride layer is deposited (b) to electrically isolate the silicon substrate from the future electrodes.

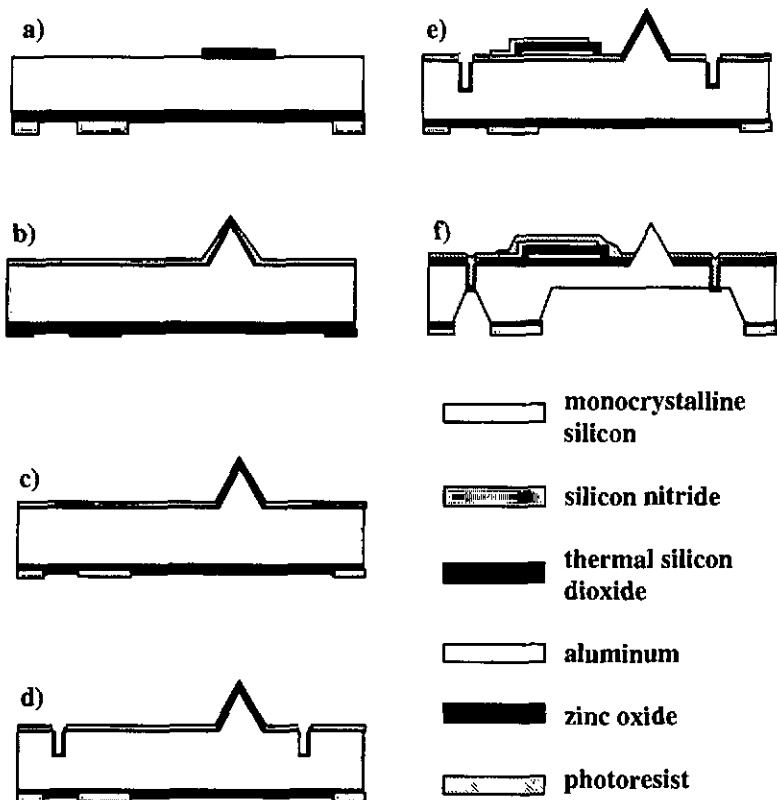

Fig. 6.2.3 Fabrication process for cantilevers with integrated tip and piezoelectric layer: (a) Patterning of first oxide and nitride layers (b) Tips forming and deposition of thin oxide and nitride layers (c) Removing of upper nitride layer on the tips and growth of a thick oxide cap (protection against next RIE step) (d) Etching of 10 µm wide and 5 µm deep trenches to delimit the levers and thin oxidation of the walls and bottom (e) Deposition and patterning of both electrodes and ZnO layer (f) Deposition of thick photoresist layer on the upper side, protection with a chuck and etching through of the backside in KOH.

In the next step, the nitride is removed from the top of the tips with RIE and BHF lift-off. To do this, a thick layer of photoresist is spun on the wafer, from which the tips emerge (Fig. 6.2.4). Removal of the nitride layer is first partially done by RIE with a chlorine / fluorine gas mixture (C_2ClF_5/SF_6) (Fig. 6.2.5). The silicon is protected during this step by the thin underlying oxide layer. The tip effect observed during this step was utilized to open small apertures on the apex of SNOM tips (see Chap. 4.7). Nitride removal is achieved by a BHF lift-off type etch, during which the underlying oxide layer is removed (Fig. 6.2.6). Then, a thick oxide is grown on the nitride free top of the tips to protect them during the next step (Fig. 6.2.7) (c). The cantilevers are then delimited by 10 μm wide and 5 μm deep trenches etched with RIE. The walls and bottom of these trenches are covered with a thin layer of oxide which will act as an etch stop for the final KOH etching (d).

Fig. 6.2.4 Tip with thin oxide and nitride coating emerging from a thick photoresist layer.

Fig. 6.2.5 Partial nitride RIE etching. Silicon is protected by the thin underlying oxide layer. Note tip and edges effects. Scale bar is 2 μm.

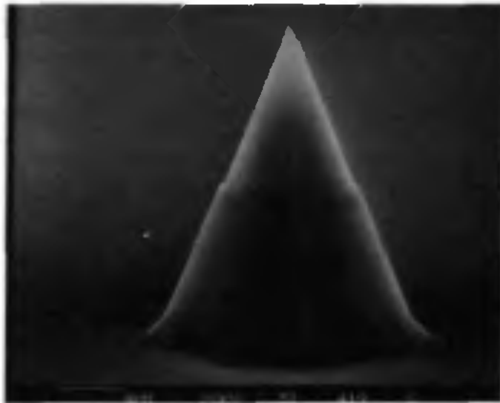

Fig.6.2.6 Tip after complete nitride removal with BHF lift-off like etching. Silicon apex was perfectly protected during the whole process. Note the dark 1 μm wide underetched ring at the edge of the nitride layer.

The second part of the process is similar to the one developed by Racine et al. [9], and begins with the deposition of the aluminum electrodes and the ZnO layer. The first electrode is patterned by wet etching, and is covered with a thin layer of chemical vapor deposited (CVD) oxide to improve the quality of ZnO crystal growth and to provide electric isolation. Then, the ZnO layer is deposited by reactive sputtering and patterned in a solution of acetic and phosphoric acids and DI water (1:1:110). This technique allows an underetching rate of ZnO of about *200 %*, which is comparable with other results [1]. After deposition of a second thin CVD oxide layer, the upper electrode is deposited and patterned also by wet chemical etching (e). Finally, the upper face is covered with thick photoresist, the oxide on the top of the tips is removed in BHF and the wafer is sealed in a chuck and etched through from the backside in KOH (f). The oxide layer at the bottom of the trenches grown in step (d) is etched before removing the photoresist with acetone.

Fig. 6.2.8 and 6.2.9 show lateral views of a released cantilever and a close-up view of the tip. Curvature radius of the apex is estimated to be less than 50 nm. This value is larger than the one of commercial silicon tips etched in KOH because of the smoothing effect of the high temperature oxidation step. This effect could be compensated by sharpening the tips with a low temperature oxidation process [10].

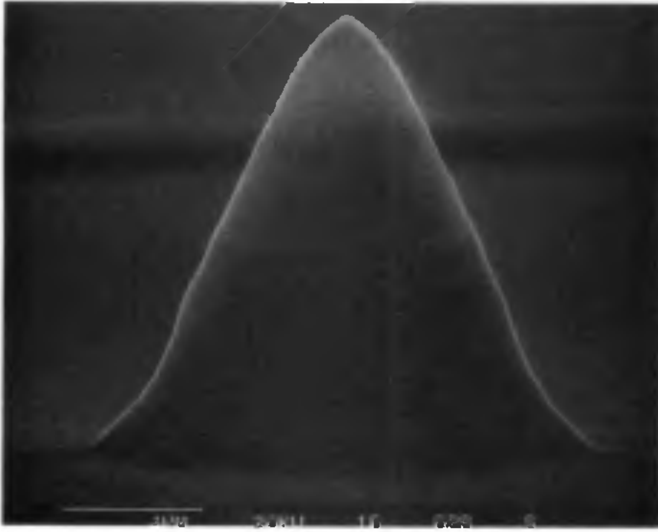

Fig. 6.2.7. Tip after 1 μm silicon dioxide growth on the nitride free top.

Fig.6.2.8. Released cantilever with sharp tip and side-by-side zinc oxide lanes for lateral force detection.

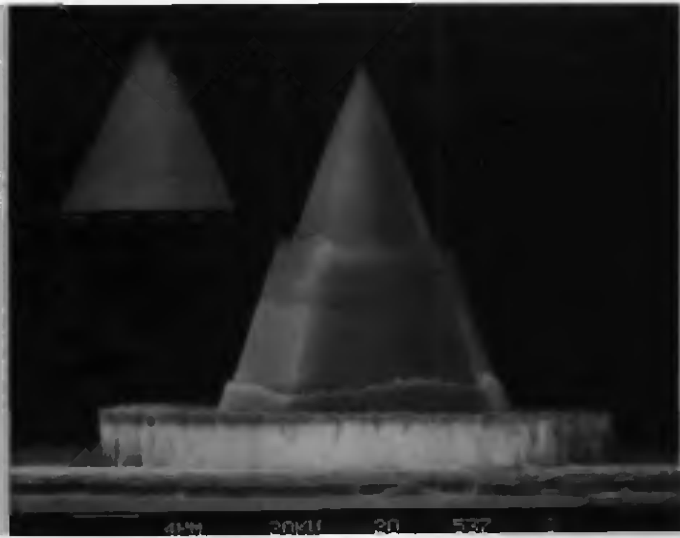

Fig.6.2.9. Close-up view of the tip. Aluminum and ZnO etch residues can be seen at the bottom. Scale bar on the insert is 400 nm. Radius of curvature of the apex is less than 50 nm.

6.3 Electromechanical characterization

6.3.1 Quasi-static actuation

In order to maintain the tip at a constant distance above the surface to be imaged, a fully integrated cantilever has to compensate for the sample topography. In this section, the quasi-static actuation of the lever with piezoelectric layer will be characterized.

Fig. 6.3.1 shows a sequence where a 1 Hz alternating signal of 20 V_{pp} was applied to a 500 μm long, 130 μm wide and 5 μm thick beam. A low frequency bias of 40 V is added by hand at a lower frequency to the signal and the vertical displacement of the beam is measured with a confocal microscope. The measured deflection at the end of the cantilever was about 30 Å/V. This deflection, $\delta(L)$, at the end of a piezoelectric beam can be calculated as a function of the applied voltage, V, with the following expression [11]:

$$\delta(L) = \frac{-3d_{31}s_{11}^{si}s_{11}^{p}h_{si}(h_{si}+h_p)L^2}{K}V \qquad (6.3.1)$$

where s_{11}^{si} and s_{11}^{p} are the compliance under mechanical stress of the substrate and the ZnO film respectively, h_{Si} is the thickness of the substrate, h_p that of the piezoelectric film, d_{31} the piezoelectric coefficient and

$$K = 4s_{11}^{p}s_{11}^{si}h_{si}(h_p)^3 + 4s_{11}^{p}s_{11}^{si}(h_{si})^3h_p + (s_{11}^{p})^2(h_{si})^4 + (s_{11}^{si})^2(h_p)^4 + 6s_{11}^{p}s_{11}^{si}(h_{si})^2(h_p)^2 \qquad (6.3.2).$$

In this calculation the following constants were used: Si substrate: s_{11}^{si} = 0.77 10^{-11} m^2/N, ZnO film: s_{11}^{p} = 0.79 10^{-11} m^2/N and d_{31} = 5.4 10^{-12} C/m (single crystal values of ZnO). A value of 180 Å/V is calculated. If we consider that in our case the piezoelectric layer is only active between the two electrodes (about 20% of the whole piezoelectric layer) and that the value of the transverse piezoelectric coefficient for a polycrystalline layer amounts 50 to 80 % of the bulk value [12], the measured value of about 30 Å/V is in agreement with the analytical model of J. G. Smits and W. Choi [11] and other authors [1]. No impedance variations were observed in the ZnO layer in spite of the relatively high applied voltages.

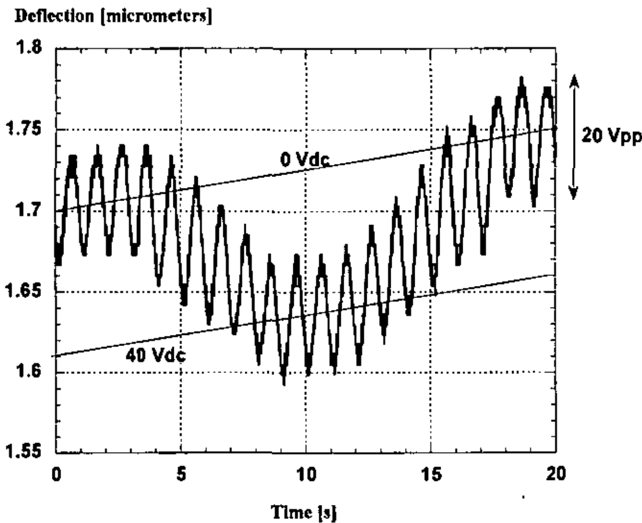

Fig.6.3.1. Pseudo static actuation of a 500 μm beam. A DC bias voltage varying from 0V to 40 V and then from 40 V to 0 V again is added to a 20 Vpp pseudo static signal at 1 Hz. General drift is due to the measurement set-up.

6.3.2. Actuation and detection near tbe first resonance frequency

Optical and electrical measurements were performed on various levers to characterize their mechanical and electrical behavior. All the results presented in this section, except the measurements shown in Fig. 6.3.6, were obtained with the same structure, namely, a 500 μm long, 130 μm wide and 10 μm thick cantilever. Fig. 6.3.2 shows the mechanical response (beam deflection) of the cantilever beam generated by vibrating the chip with an external piezoelectric plate (plain line) and by directly exciting the cantilever with the integrated piezoelectric layer (rough dashed line) near the first resonance frequency (54.45 kHz) of the free cantilever. The beam deflection, measured with an optical interferometer, was found to be 450 nm and 80 nm, respectively. The excitation voltage, applied to the integrated piezoelectric layer, was 200 mV_{rms}. The quality factor was measured to be about 280. The impedance of the integrated piezoelectric layer of the same structure was measured by applying a 200 mV_{rms} signal and is represented on the graphic of Fig. 6.3.2 by the fine dashed line.

The direct piezoelectric effect was characterized by measuring the current generated by the cantilever excited with an external vibrating plate as in Fig. 6.3.2. As shown in figure 6.3.3, a maximum signal of 24 nA was found at the resonance frequency for a vertical displacement of 450 nm.

Simultaneous excitation and detection [5, 13] of the cantilever was measured by incorporating a 100 kΩ resistor on one of the contact wires to the integrated piezoelectric layer. The voltage at the borders of this

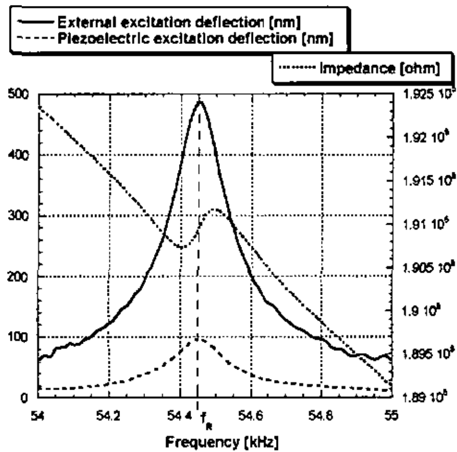

Fig.6.3.2 Mechanical displacement (left scale) at the end of a 500 μm long cantilever generated by external excitatian (plain line) and by actuatian with integrated piezaelectric layer (raugh dashed line). The impedance of the same device is represented with the fine dashed line (right scale).

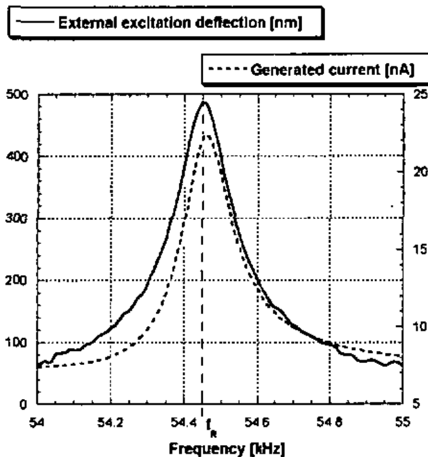

Fig. 6.3.3. Direct piezoelectric current (right scale) measured far the same structure as in Fig. 6.3.2 and generated by the deflection due ta external excitatian (left scale).

resistor was measured with a lock-in amplifier using the excitation signal as reference (Fig.6.3.4).

The current through the resistor is obtained by dividing the measured voltage by the value of the resistor. Fig. 6.3.5 shows this current near the resonance frequency as well as the mechanical displacement generated at the end of the cantilever by applying a 200 mV_{rms} excitation signal to the integrated piezoelectric layer. This displacement was measured optically. On Fig. 6.3.6, the amplitude of the current through the external resistor I_R of a 700 μm long cantilever is plotted near the first resonance frequency for various excitation voltages. Curves were offset to illustrate the part of the current due to the mechanical resonance.

As it can be observed on Fig. 6.3.5 and 6.3.6, I_R depends on the amplitude of the mechanical vibrations of the cantilever (plus a phase change at resonance frequency). Thus, I_R may be used to detect the amplitude and frequency variations of cantilever oscillation. This allows a very compact self-exciting detection scheme.

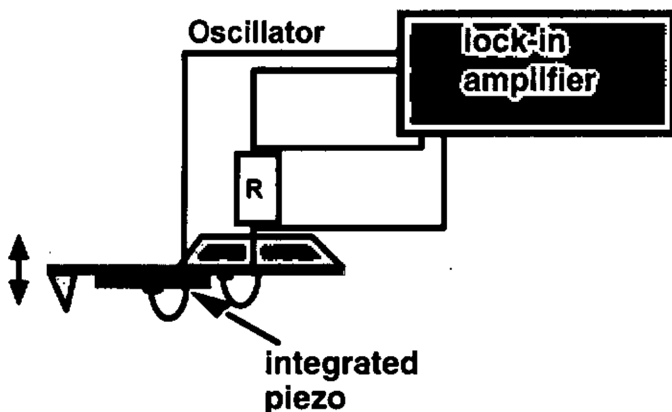

Fig. 6.3.4 Simultaneous excitation and detection scheme for a cantilever with integrated piezoelectric layer.

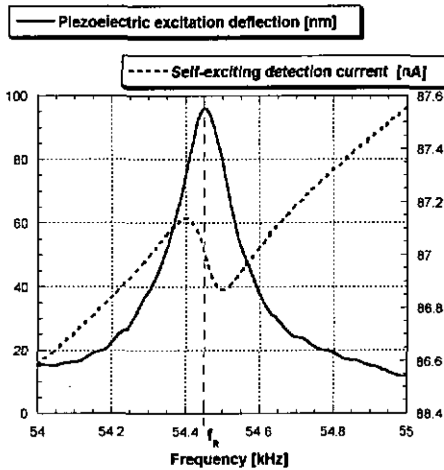

Fig. 6.3.5 Current I_R through the resistor on one contact wire of the integrated piezoelectric layer (right scale, dashed line) and mechanical displacement at the end of a 500 μm long cantilever near resonance frequency for a 200 mV_{rms} excitation (right scale, solid line).

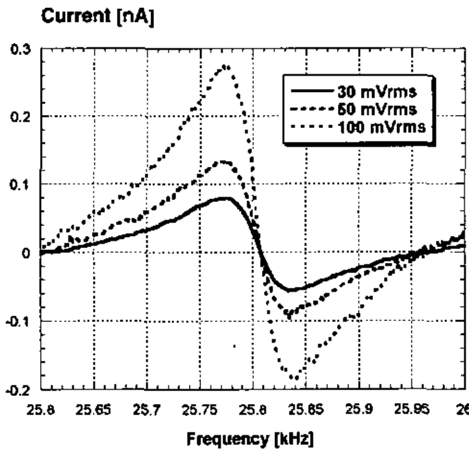

Fig. 6.3.6 I_R current for a 700 μm long cantilever for different excitation voltages. Curves were offset to illustrate the effect due to the mechanical resonance.

6.4 AFM imaging with piezoelectric cantilevers

The cantilevers were fitted in a commercial NanoscopeIII® AFM thanks to specially designed PCB's and metal support (Fig. 6.4.1). Images of grids in dynamic and contact mode were achieved by using this set-up, which allowed simultaneous optical and piezoelectric detection.

Fig. 6.4.1 Silicon chip with a 1000 μm long cantilever glued on a PCB with 5 metal lanes and screwed on a metal support. The ensemble can be fitted in a Nanoscope® III AFM head.

6.4.1 Dynamic mode AFM imaging

The detection scheme presented in Fig. 6.3.4 was connected to the NanoscopeIII® electronics as shown in Fig. 6.4.2. The cantilevers were operated near the resonance frequency, at a constant current I_R. Fig. 6.4.3 shows the deflection and the amplitude of the current versus the distance from the sample surface. The amplitude of the freely vibrating level was measured optically and was found to be about 30 nm. In Fig. 6.4.3, the deflection was measured optically. With this calibration, a sensitivity of about 2.5 pA/nm and an estimated noise level of about 7 pA were computed.

Fig. 6.4.4 (a) shows an image of a grid with a 1 μm period. It was realized with a cantilever with integrated tip and self-exciting piezoelectric detection. For comparison, Fig. 6.4.4 (b) represents the same surface imaged with a commercial cantilever with KOH-etched silicon tip and optical detection. The height of the lines was about 15 nm. Details of the features are very similar on both pictures. Note especially the trenches behind the lines. The parallel lines in 6.4.4 (a) are probably due to a shift in the impedance value of the ZnO layer due to material degradation.

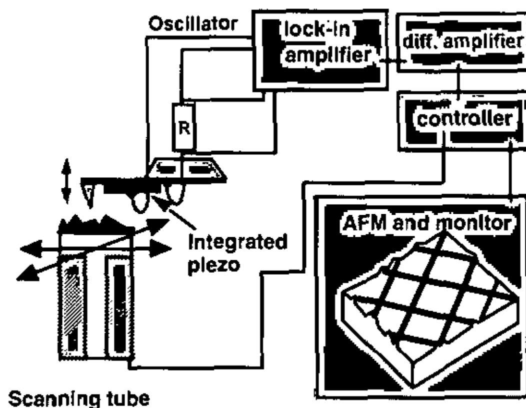

Fig.6.4.2 Detection scheme for AFM imaging with self-exciting piezoelectric cantilever detection

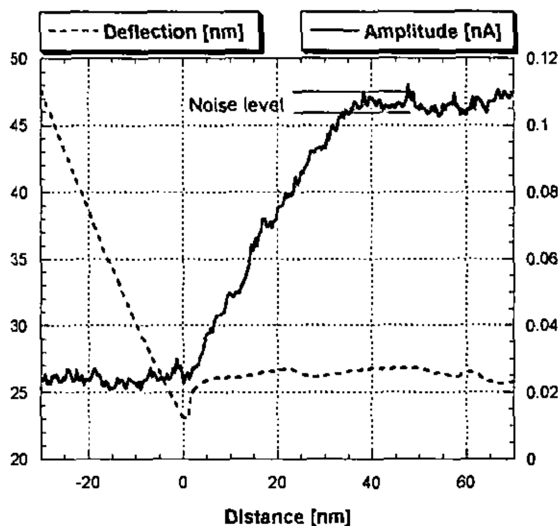

Fig. 6.4.3 Cantilever deflection (left scale) and I_R amplitude (right scale) as a function of the distance to the sample. Free vibration amplitude was measured optically to be about 30 nm. Noise level wos determined visually.

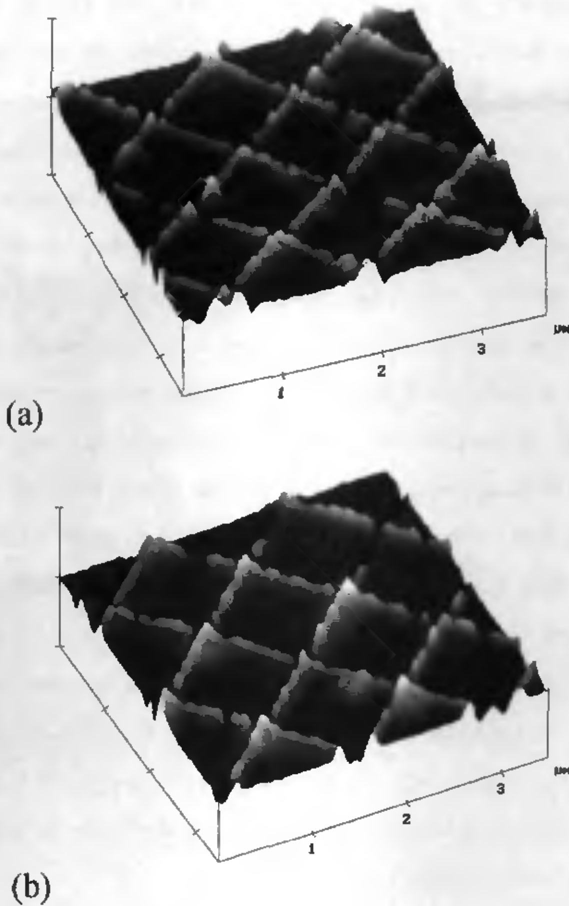

Fig. 6.4.4. (a) Dynamic mode AFM image of a grid with a 1 µm period achieved with a cantilever with integrated tip and self-exciting integrated piezoelectric sensor. Height difference is about 15 nm. (b) Dynamic mode image of the same grating taken with a commercial instrument (silicon tip and optical detection, NanoScope® III, Digital Instrument). Note the appearance of the lines and the small trenches behind them.

To compare the quality of piezoelectric and optical detection, simultaneous measurements with both sensing techniques were performed. The counter-reaction was generated from the optical signal while both optical and piezoelectric error signals were recorded. The sample was a quartz substrate with chrome lines with a period of 250 nm and a height of about 100 nm. As can be observed on Fig. 6.4.5 (a), the piezoelectric error signal is much more noisy than the optical one in Fig. 6.4.5 (b), but the features can be clearly distinguished. Note the contamination on the top right corner, proving that both pictures were taken at the same place.

In order to compare the quality of commercial tips and cantilevers with the piezoelectric ones, images of the same sample were achieved with optical detection for both types of cantilevers. The upper profile of Fig. 6.4.6 was taken with a piezoelectric cantilever (and optical detection) and the lower one with a commercial cantilever with KOH-etched silicon tip. Only slight differences can be observed between the two profiles. As the cantilevers needed to be changed between these two experiments, it was not possible to image exactly the same area. It is thus difficult to determine if the small variations between both profiles are due to the tip geometry or to sample inhomogeneity.

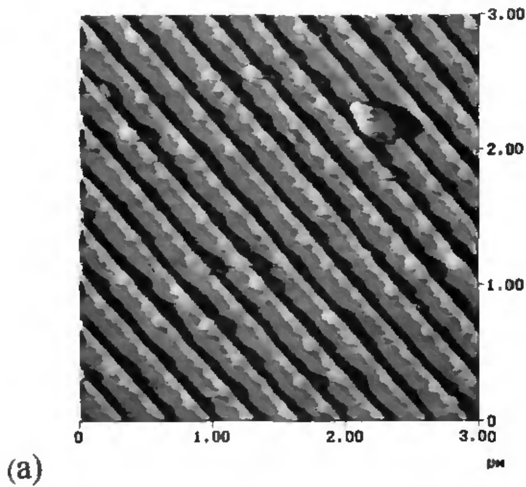

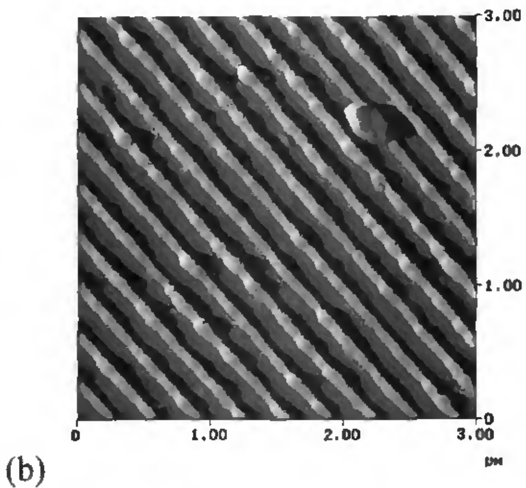

Fig. 6.4.5 Simultaneous piezoelectric (a) and optical (b) error signals (uncompensated amplitude variation) of a 3 x 3 μm^2 image realized with a piezoelectric cantilever. The sample consists of chrome lines with a period of 250 nm and a height of about 100 nm on a quartz substrate

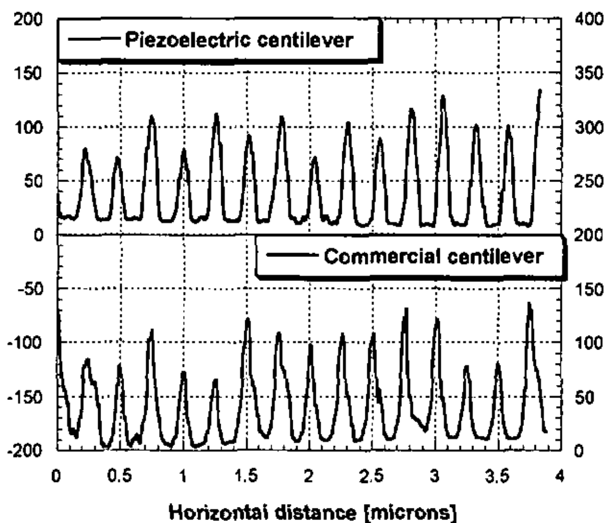

Fig.6.4.6 Sections of 100 nm high chrome lines with a period of 250 nm on a quartz substrate realized with a piezoelectric cantilever (upper profile, left scale) and with a commercial cantilever with KOH-etched silicon tip (lower profile, right scale). Optical detection was used in both cases.

6.4.2 Contact mode imaging

According to [11], the charge Q(δ) due to the direct piezoelectric effect and produced by a piezoelectric bimorph can be expressed as a function of the deflection, δ, generated at the end of the cantilever with following expression:

$$Q(\delta) = \frac{3d_{31}Bw}{4L}\,\delta \qquad (6.4.1)$$

where d_{31} = 5.4 10^{-12} C/m (single crystal values of ZnO) is the piezoelectric coefficient, w and L are respectively the width and the length of the bimorph, and B is a constant depending on the material used. A cantilever with dimensions 1000 μm long, 100 μm wide and 10 μm thick (5 μm silicon and 5 μm zinc oxide) would then generate a charge of about 0.5 fC/nm, which lies within the detectable domain. The vertical spring constant of such a cantilever can be estimated to be about 5 N/m.

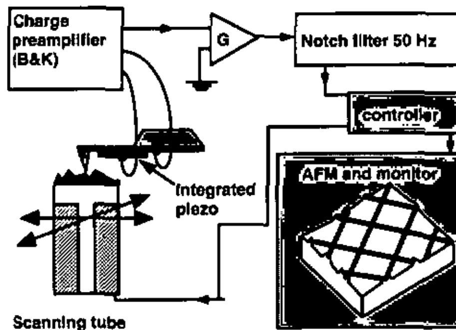

Fig. 6.4.7 Set-up for contact mode imaging with piezoelectric detection.

Using the set-up shown in Fig. 6.4.7 and the same support as shown in Fig. 6.4.1, contact mode images were achieved with piezoelectric detection. The tip of a 1000 µm long cantilever was brought in contact with the sample and scanned. The direct piezoelectric signal induced by the topography was first amplified by a Brüel&Kjaer charge preamplifier. The 50 Hz noise was notch-filtered before the signal was sent to the Nanoscope® controller.

Fig. 6.4.8 shows a top view of a 15 x 15 μm^2 image of a grid with a period of 10 µm and with a hole depth of 180 nm. Fig. 6.4.9 represents a 3 x 3 μm^2 image of a 1 µm period grid with 15 nm high lines. On Fig. 6.4.10, deflection and charge versus distance curves are presented. The measured sensitivity is about 1 fC/nm, which lies in the same order of magnitude as the above calculated value. Note that the charge curve is very similar to an exponential capacitance discharge curve.

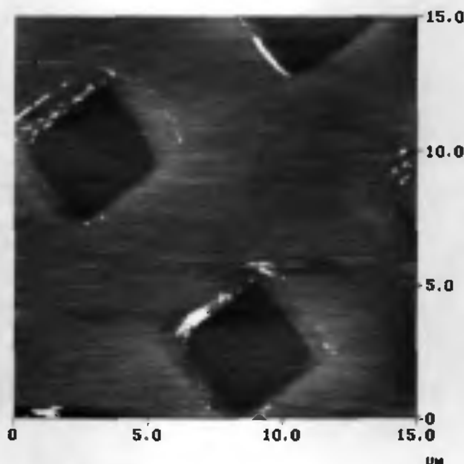

Fig. 6.4.8 Contact mode piezoelectric detection image of a 10 µm period grid. Depth of the hole is about 180 nm

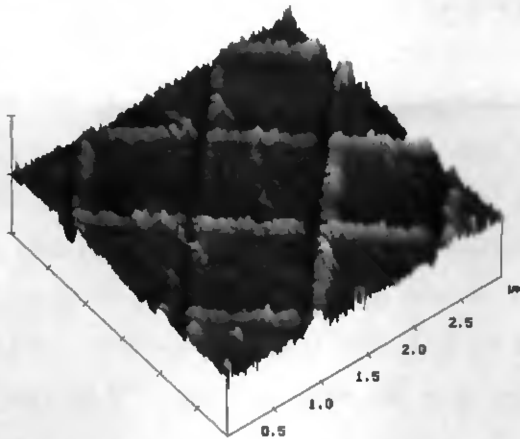

Fig. 6.4.9 Image of a 1 µm period grid realized by using contoct mode piezoelectric detection. Height of the lines is about 15 nm

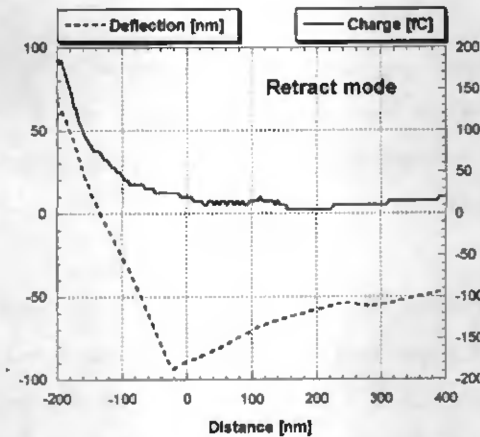

Fig.6.4.10 Simultoneous deflection (left scale) and charge (right scale) versus distonce in retroct mode for o 1000 µm long piezoelectric contilever. Sensitivity is obout 1 fC/nm.

6.5 Discussion

Parallel AFM imaging requires arrays of cantilevers with integrated actuation and detection functions. In this chapter, a process was developed which allows the fabrication of piezoelectric cantilevers with integrated self-sharpening tips. The alignment of such an array of cantilevers could be easily done by vibrating only the two external levers during the approach. The vibration amplitude of some tens of nanometers is enough to impede the other non vibrating tips to touch the sample (Fig. 6.5.1).

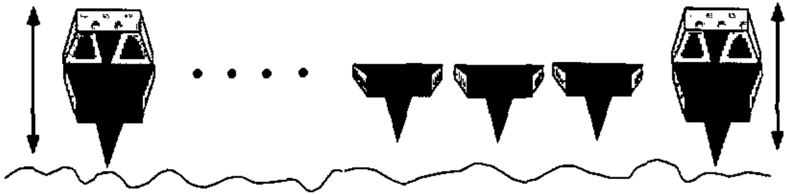

Fig.6.5.1 Schematic approach procedure for an array af self-exciting cantilevers with integrated detection: only the external levers are vibrated, allowing a safe approach ta the surface to be imaged

The operation of these cantilevers with optical detection demonstrated that their imaging ability is very close to that of commercial cantilevers with wet etched silicon tips. Nevertheless, piezoelectric actuation and detection showed some undesirable characteristics. First, the electrical behavior may vary significantly from one cantilever to another. SEM observations revealed that this may be due to bad metal coating of the 5 µm zinc oxide step (Fig. 6.5.2). Contact quality could be improved by depositing a thicker metal layer. This could be done locally, to avoid

cantilever stiffening. Second, evidence of electrical break-down were observed during approach curves in dynamic and DC mode (Fig. 6.5.3). It is not clear whether this phenomenon is due to insufficient insulation between piezoelectric layer and electrodes, humidity on the zinc oxide layer or defects in the piezoelectric material itself. Finally, lack of symmetry was observed in DC mode actuation (Fig. 6.5.4). Again, more investigations would be required to decide if this effect is due to piezoelectric material properties or to the geometry of the cantilever (slight initial bending due to internal stress, for example).

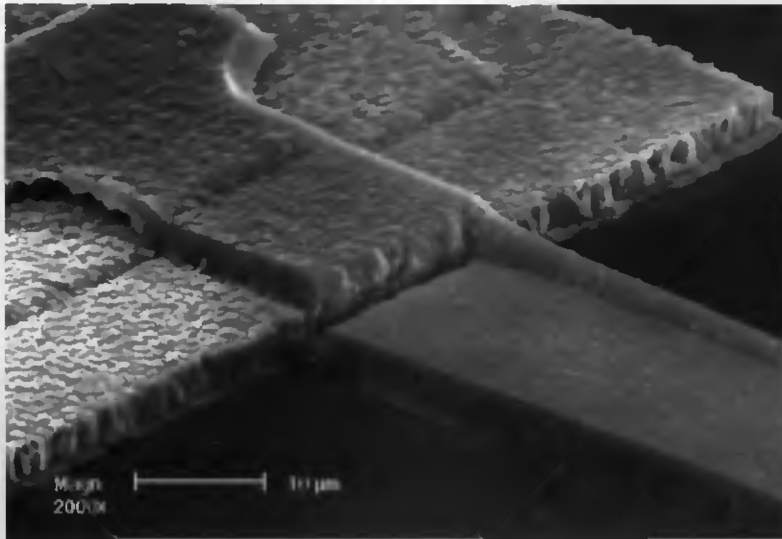

Fig. 6.5.2 Uncompleted metal coating of the 5 μm zinc oxide step may be responsible for bad electrical contacts to the upper electrode

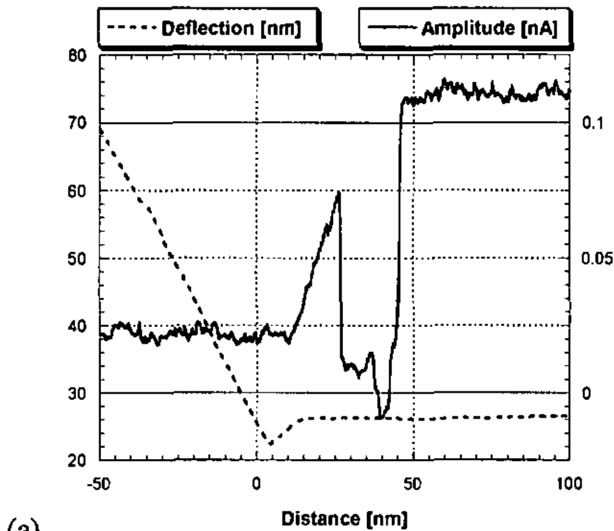

(a)

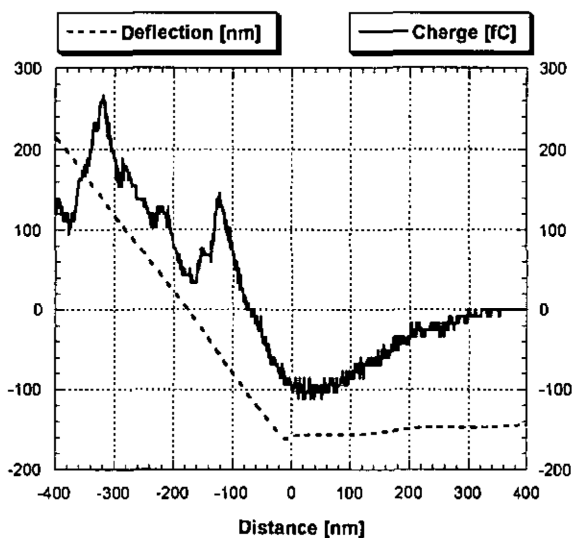

(b)

Fig. 6.5.3 Break-down-like discontinuities in amplitude ((a), right scale) and charge ((b), right scale) versus distance curves (left scales). See text for an explanation of possible causes.

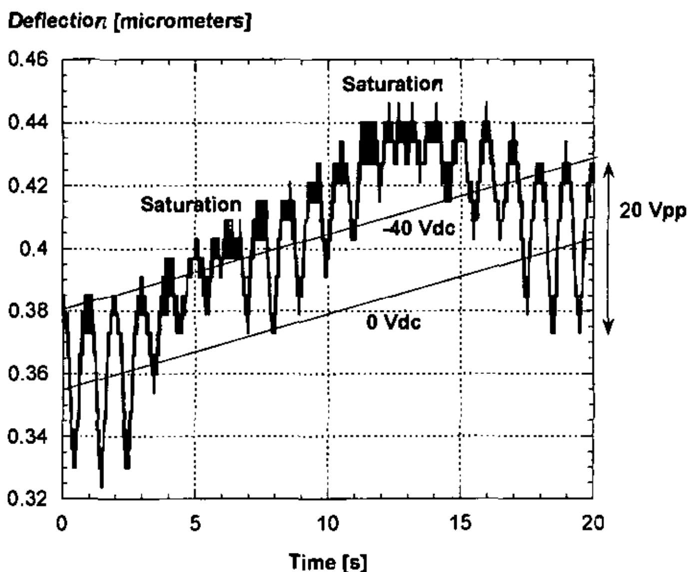

Fig. 6.5.4 Pseudo static actuation of a 500 μm beam. A DC bias voltage varying from 0V to -40 V and then from -40 V to 0 V again is added to a 20 Vpp pseudo static signal at 1 Hz. General drift is due to the measurement set-up. Two so-called saturation regions appear clearly between -40 and 0 V but it is not clear whether they are generated by material properties or by the geometry of the cantilever. See Fig. 6.3.1 to compare the DC actuation with the same 20 Vpp signal at 1 Hz but with a superimposed voltage varying between +40 and 0 V.

6.6 Conclusion to chapter 6

Cantilevers with integrated self-exciting piezoelectric sensors represent a very elegant solution for parallel AFM imaging. The actuator and detector functions are achieved by one single piezoelectric layer sandwiched between two metal electrodes, so that technological steps remain as few and as simple as possible. Neither the deposition nor the patterning of these layers require high temperature or strong etchants. In this chapter, it was demonstrated that wet etching techniques for tips allow the fabrication of arrays of such cantilevers with highly reproducible sharp tips. Such arrays could be easily and safely brought in close proximity to the samples for imaging.

However, variations of the electro-mechanical characteristics from one cantilever to another were observed as well as variation of the characteristics of one cantilever over time. It is not clear whether these changes are produced by material deposition, insufficient insulation of the electrodes or material degradation. Thus, deposition of piezoelectric thin films and the aging behavior of these layers should be further investigated to ensure reliable fabrication processes and devices with acceptable lifetimes.

References to chapter 6

1. S.C. Minne, S.R. Manalis and C.F. Quate, Appl. Phys. Lett. 67 (26) 1995, pp. 3918-3920
2. T. Itoh, C. Lee and T. Suga, Appl. Phys. Lett. 69 (14) 1996, pp. 2036-2038
3. T. Fujii and S. Watanabe, Appl. Phys. Lett. 68 (4) 1996, pp. 467-468
4. N. Blanc, J. Brugger, N.F. de Rooij and U. Dürig, J. Vac. Sci. Technol. B 14 (2) 1996, pp. 901-905
5. K. Takata, Jpn. J. Appl. Phys. 32, 1993, pp.2455-2458
6. J. Brugger, J. Burger, M. Binggeli, R. Imura and N.F de Rooij, Proceedings of the Transducers and Eurosensors '95 Conference, Stockholm (Sweden), 1995, p. 636-639
7. O.Wolter, Th.Bayer and J.Greschner, J. Vac. Sci. Technol., B 9, 1991, p.1353
8. J.-H. Liu, T.M. Betzner and H.T. Henderson, J. Micromech. Microeng. 5, 1995, p.18
9. G.-A. Racine, R. Luthier and N.F. de Rooij, Proceedings of the MEMS '93 Conference, Fort Lauderdale (USA), 1993, p 128
10. R.B. Marcus and T.T. Sheng, J. Electrochem. Soc., Solid State Science and Technology, 1982, p.1278
11. J. G. Smits and W. Choi, IEEE Trans. Ultrason. Ferroelectr. Freq. Control 38 (3) 1991 pp. 256-270
12. T. Itoh and T. Suga, Jpn. J. Appl. Phys. 33 (1) 1994, pp. 334-340
13. T. Itoh and T. Suga, IEICE Trans. Electron. E78-C (2) 1995, pp. 146-151

Chapter 7

Electrolytic thin layer STM probes

7.1 Introduction

The scanning tunneling microscope (STM), demonstrated for the first time in 1981 by G. Binnig and H. Rohrer [1, 2], very soon revealed itself to be a powerful tool for electrochemical studies at nanometer scale [3]. However, the problem of access to the chemical information about the electrolyte near the scanning tip has not yet been solved in a satisfying way. The Scanning ElectroChemical Microscope (SECM) [4] allows the imaging of chemical properties of a surface, but does not have the high resolution of STM. The situation can be significantly improved if the scanning tip is located in a so-called electrolytic thin layer [5, 6, 7].

In this chapter, the fabrication of a new scanning probe defining an electrolytic thin layer (ETL) around the tunneling tip is described. Furthermore, a ring electrode, which is integrated on the probe and around the tip, allows the controlled deposition and desorption of electroactive species during the scan. First, the concept of the Electrolytic Thin Layer Scanning Tunneling Microscope (ETL-STM) will be discussed. Then, the fabrication process will be described in detail, and, finally, first measurements will be presented and briefly discussed.

This project was realized in collaboration with the Universtity of Bern and with the Paul Scherrer Institute in Villigen.

7.2. The electrolytic thin layer scanning tunneling microscope (ETL-STM)

The determination and controlled generation of chemical species involved in electrolyte/electrode interface reactions is of primary importance for electrochemical scanning probe microscopy. Thus, the development of a scanning probe able to precisely control concentrations of specific electroactive compounds near the scanning tip is of great interest. Fig. 7.2.1 shows a schematic representation of such a device. A tip and a ring electrode for electroactive compound sensing and generation are fitted on a large cylinder (relative to tip dimensions) made of chemically inert and insulating material. The tip and the electrode are

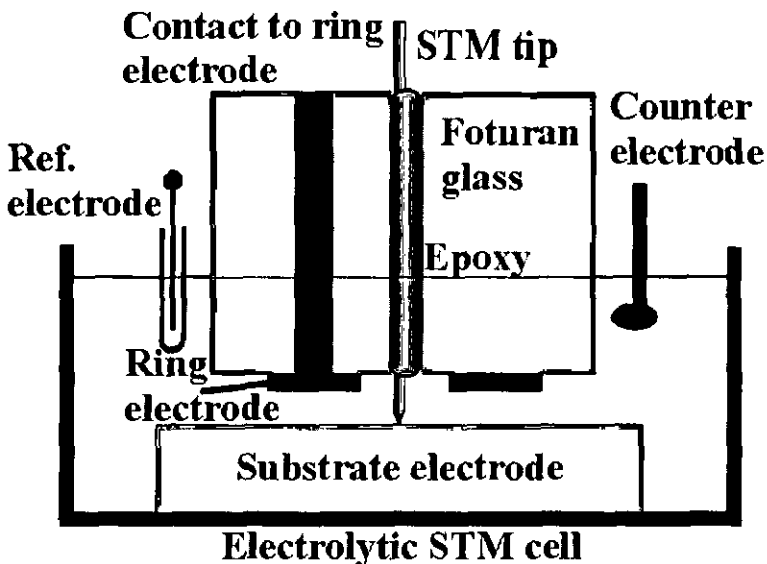

Fig. 7.2.1 Schematic illustration of electrolytic thin layer scanning tunneling microscope

each independently connected through the insulating material by metallic contacts. As the salient part of the tip is only a few tens of micrometers long, the electrolyte layer between the cylindrical probe and the substrate forms an electrolytic thin layer. The whole probe is mounted on a piezotube to allow the scanning of the sample. In this thin-layer STM concept, the ring is operated as a potential controlled electrode that can be used as an electrochemical generator or sensor of electroactive compounds involved in electrochemical reactions at the substrate electrode (Fig 7.2.2).

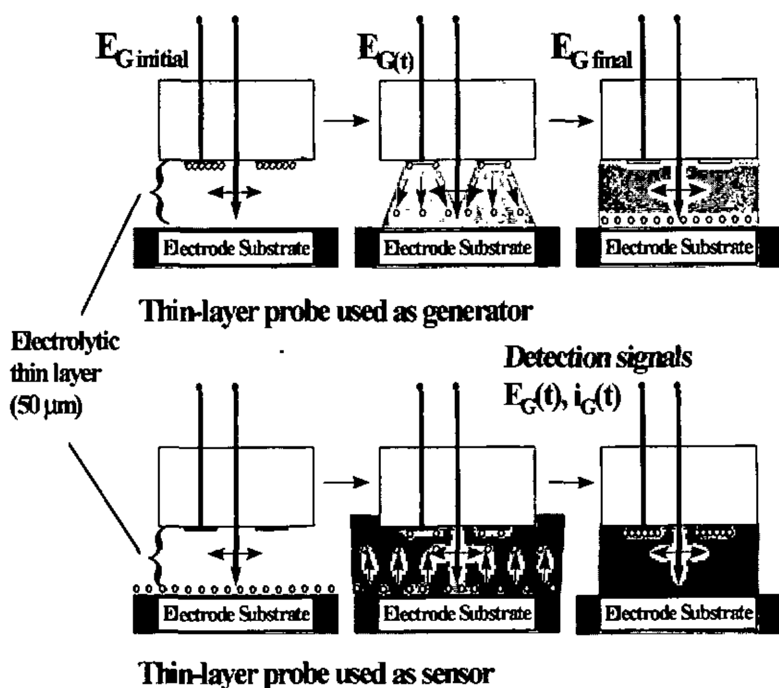

Fig.7.2.2 Working principle of the electrolytic thin layer scanning tunneling microscope (ETL-STM)

7.3. Structure design and fabrication

7.3.1. Probe design

Because it is chemically inert, has high electrical resistance, and can be etched to form features having high aspect ratios, the photostructurable glass Foturan®[8, 9] was the ideal candidate for the cylindrical body of the probe. Since Foturan does contain Ag, a species which could act as interferent were it to leach out into solution, the following experiment was done. A piece of Foturan was immersed in a 10^{-2} M perchloric acid ($HClO_4$) solution for 60 days. After this time, the Foturan was removed, and a current-voltage curve in the $HClO_4$ solution was obtained to determine whether Ag was present to any significant extent. Fig. 7.3.1 shows this Ag trace analysis curve. As a comparison, measurements in 10^{-2} M $HClO_4$, and with additional silver concentrations of 10^{-7} M, 10^{-8} M and 10^{-9} M were performed. From these measurements, it was found that the silver concentration of Foturan was less than 10^{-9} M. Cylinders with diameters varying between 250 and 1400 μm, and with 2 to 3 via holes with diameters varying between 30 and 160 μm, were designed to determine a compromise between dimensions of the electrolytic thin layer and difficulty of probe approach.

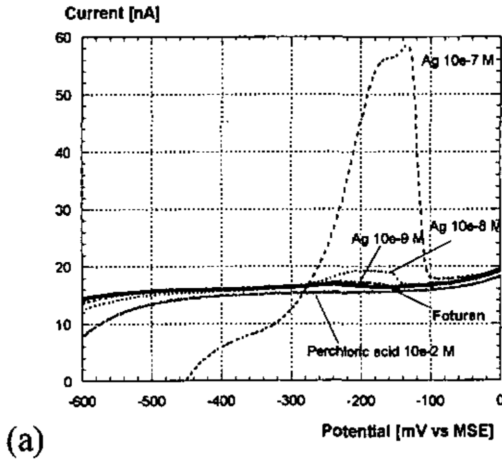

(a)

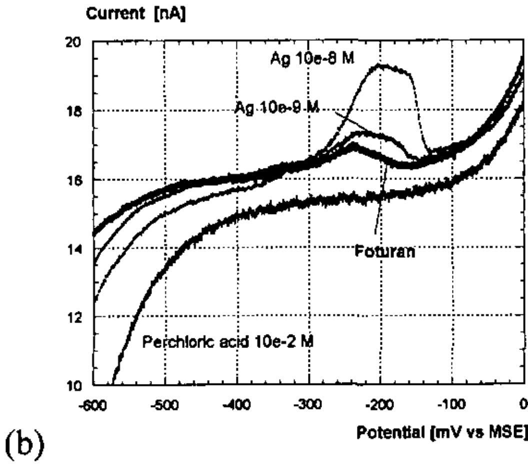

(b)

Fig. 7.3.1 Silver trace analysis in Foturan compared with 10^{-2} M perchloric acid with additional Ag^{+} concentration of 10^{-7}, 10^{-8} and 10^{-9} M respectively (a) and detail view of smallest dissolution peeks around 200 mV vs mercury sulfate electrode (MSE). Deposition time on the electrode was 60 s at -800mV vs MSE and scan rate was 1 mV/s.

3.2. Probe fabrication

The key step of the fabrication process (Fig. 7.3.2) is the electrochemical growth of the metal contacts through the glass cylinders [10]. This could be achieved in a parallel way by bonding the glass wafer with photoresist onto an oxidized silicon wafer on which a seed layer was previously patterned.

3.2.1 Structuring of Foturan

First, a 1 μm thick aluminum layer was deposited and patterned on 1.1 mm thick Foturan® wafers to serve as an optical mask for UV light exposure (Fig.7.3.2.1 (b)). This step was necessary to avoid drift during the exposure time, which is several hours. Then the aluminum layer was removed by wet etching and the glass wafers were annealed following a ramp up to about 600 °C. During this step, the exposed glass was transformed into ceramic which could later be selectively etched in hydrofluoric acid (HF). Some wafers were polished and their thickness reduced to about 600 μm.

Then, the transformed glass was etched with a 10% ultrasonic HF solution (Fig. 7.3.2.2 (b)). The lateral to vertical etch ratio was about 1 to 20, i.e. the glass transformed to ceramic by light exposure and annealing was etched about 20 times faster than that which was not exposed. This allowed the microfabrication of high aspect ratio structures made of chemically inert material.

3.2.2 Seed layer patterning

Meanwhile, a seed layer was patterned onto silicon wafers to make possible the electrochemical deposition of metal in the previously etched

Foturan wafers. Silicon wafers were oxidized and a platinum seed layer was patterned on one face with the lift-off technique (Fig. 7.3.2.1 (a)). A chemical vapor deposition (CVD) insulating silicon dioxide layer was then deposited and patterned with standard photolithography to avoid unwanted metal growth. Then a thick layer of photoresist was spun on the silicon wafer, and its edges removed with acetone to avoid unwanted sticking on the edges during the alignment (Fig. 7.3.2.2 (a)).

3.2.3 Assembling of Foturan and silicon wafers

During the third step (Fig. 7.3.2.3), the glass and silicon wafers were aligned and glued together using the phototresist layer which was deposited on the silicon wafer as a bonding medium. After a gas phase silanization, the Foturan® wafers were fixed in a commercial mask aligner (Al-6.2 by Electronic Vision). The silicon wafer was then inserted into the aligner without any baking, aligned and brought into close contact for one hour by a piston and a vacuum system. A prebake sequence was then performed during half an hour at 85 °C. This degassing is required from the photoresist to allow the following UV light exposure and development. It was observed that this step increased the adhesion between glass and silicon wafer for polished glass wafers, while gas bubbles appeared between both wafers for unpolished Foturan® wafers.

Then, the photoresist was exposed to UV light and developed, to be removed where metal was expected to be electrochemically grown. Metal was then grown in the holes to serve as a contact for the ring electrode (Fig. 7.3.2.4). A first prototype was realized with copper filling, using a 0.5 M Cu^{2+} / 0.1 M H_2SO_4 solution with a current density of 50 to 100 mA/cm^2 and a potential of -470 mV versus the mercury sulfate electrode

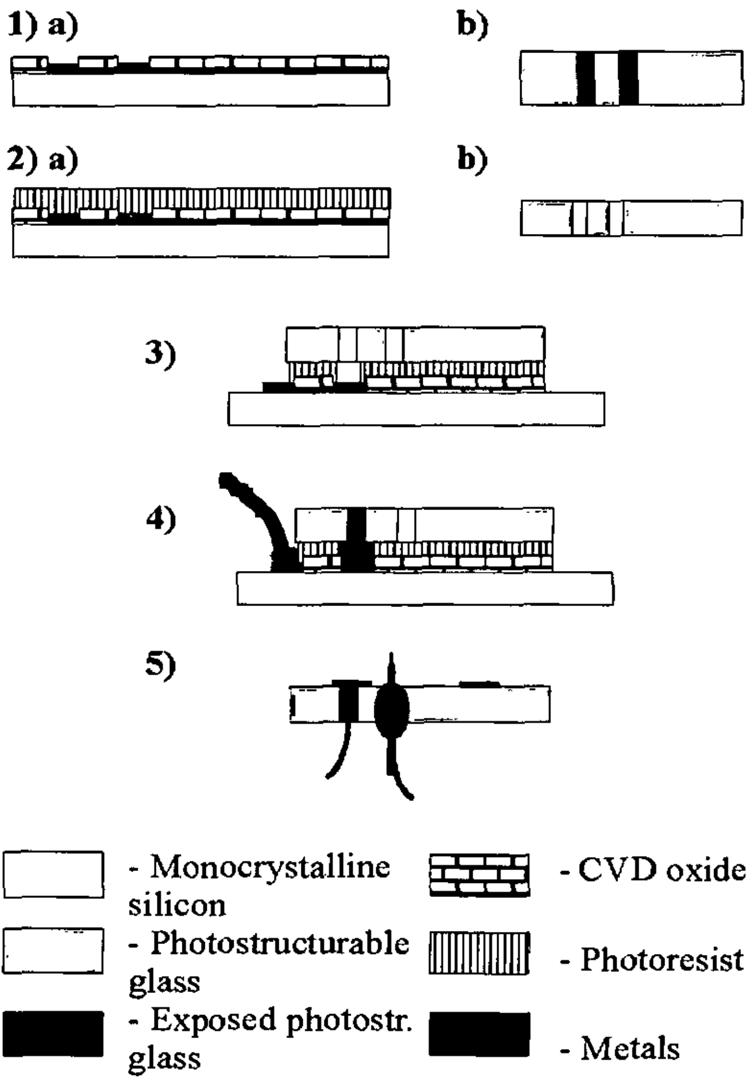

Fig. 7.3.2. Fabrication sequence far electrolytic thin layer STM probe

(MSE). The following wafers were filled with gold, in the commercially available Auro Dure 150 (Lea Ronal) solution, containing 14 g/l potassium gold cyanide (KAuCN). Holes which were filled with copper were filled to about 60 to 80% of their height, whereas the ones filled with gold were slightly overfilled. In both cases, separation of wafers could be done manually. The surfaces of the glass wafers were then smoothed by mechanical polishing. To do this, the already defined structures were embedded in cyanoacrylate glue to prevent them from being torn away by lateral forces.

Finally, a 6000 Å thick silver layer with titanium adhesion layer was deposited on glass wafers to be patterned. Due to the high aspect ratio of Foturan® structures, the photoresist needed to be sprayed with an airbrush onto the metal layer. It was then baked, exposed and developed in a standard way before silver was wet etched in an iron (III) nitrate solution [11] (Fig. 7.3.2.5). Then the tip was introduced and glued manually with a microprobe stage; packaging and electrical contacts were also realized manually. As a very last step, a 5 µm thick silver layer was electrochemically grown on the ring electrode to avoid its complete dissolution during electrolytic STM measurements.

7.4 Results

7.4.1 Fabricated devices

The good etch selectivity of the exposed glass with respect to unexposed allowed a 1.1 mm thick glass wafer to be etched through with an increase in hole diameter of only 70 μm. For the polished wafers, lateral etching was about 50 μm for a thickness of about 600 μm. Since the smallest mask opening used was 10 μm in diameter, holes with minimum diameter of about 80 μm were etched through the whole 1.1 mm thick unpolished wafer. Similarly, holes with diameter as small as 60 μm were achieved through the about 600 μm polished wafer. In both cases, holes had a circular profile. Fig. 7.4.1 shows a micrograph of a 1.4 mm diameter glass cylinder with two holes, still attached to the unpolished supporting wafer. The cylinder can be released by breaking the four sustaining arms. Tips were then fitted into the probes, on which the silver ring electrode was then electrochemically thickened to 5 μm. Fig. 7.4.2 shows an Environmental Scanning Electron Microscope (ESEM, by Philips) of a complete device. In this case, the apex of the tip was accidentally coated with epoxy.

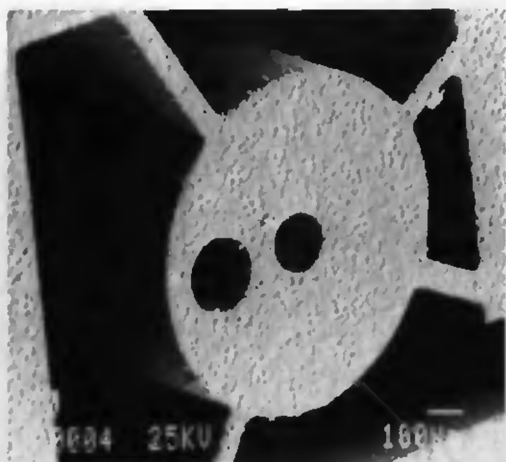

Fig. 7.4.1 Scanning probe in photostructurable gloss with via holes for STM tip (center) and for metal contoct to ring electrode (left)

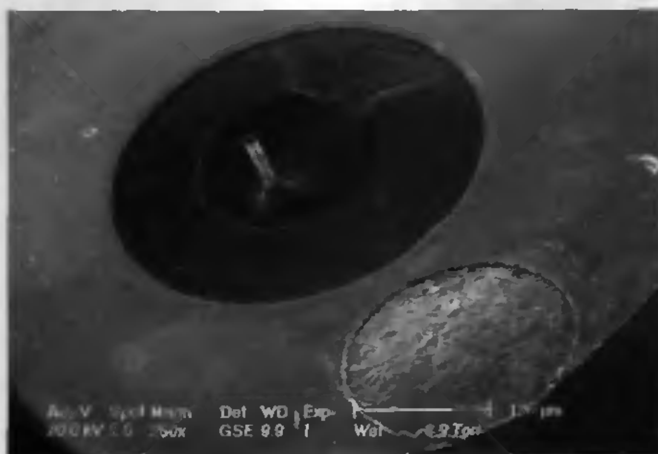

Fig. 7.4.2 Environmental SEM micrograph of o fully achieved probe. In this case, the apex of the tip was accidentally coated with epoxy.

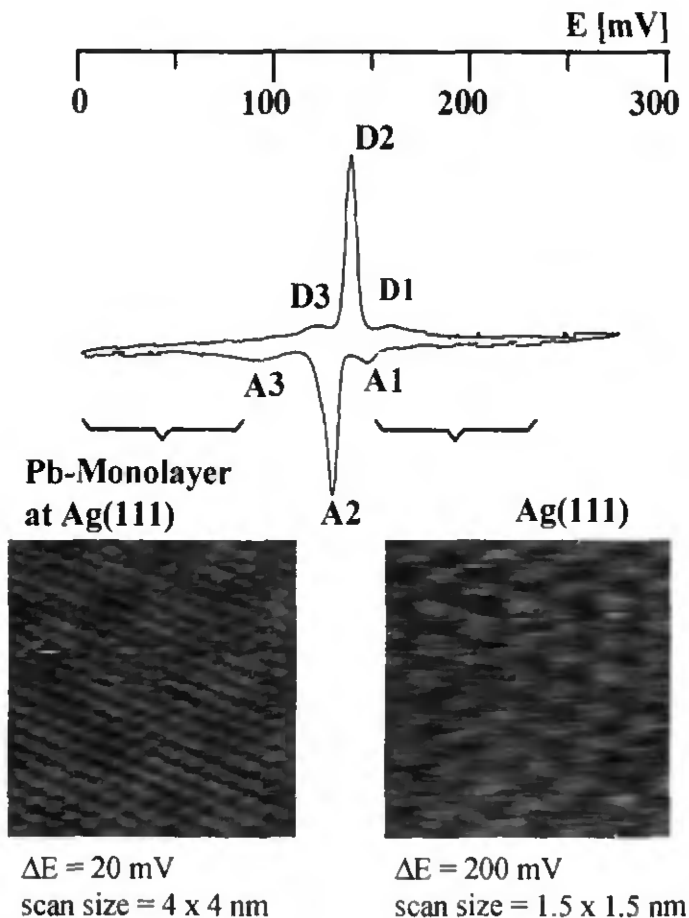

Fig. 7.4.3 Test system STM image realized with an ETL-STM probe. Points marked with an "A" and "D" represent adsorption and desorption peeks, respectively.

7.4.2 STM imaging in the electrolytic thin layer

Probes were then mounted on a commercial STM (Nanoscope by Digital Instrument). First test measurements with a thin layer probe were performed in an electrolyte solution containing 0.01M $HClO_4$ and 0.005 M lead ions at a potential controlled Ag <111> substrate electrode with atomically flat terraces that were completely covered with a lead monolayer [12, 13] (Fig.7.4.3). Atomic resolution was obtained on both silver and lead surfaces.

Electrolytic thin layer STM imaging of the same system was then achieved by using a probe with the silver ring electrode (initial conditions shown in Fig. 7.4.4 (a)). By increasing the potential of the ring electrode used as generator, a finite number of silver ions were released into the solution. Fig. 7.4.4 (b) and (c) show that the shape and size of the terraces changed due to the diffusion and deposition of the generated silver ions. Then, the lead monolayer is desorbed by increasing the potential of the substrate electrode (Fig. 7.4.4 (d)) and a new equilibrium state is obtained ((Fig. 7.4.4 (e)). Note that the texture of the surface is different at the end of the cycle ((Fig. 7.4.4 (e)) than at the beginning (Fig. 7.4.4 (a)).

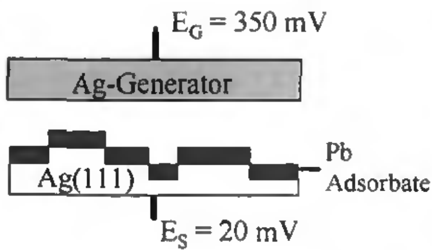
E_G = 350 mV
Ag-Generator
Pb
Adsorbate
Ag(111)
E_S = 20 mV
(a)

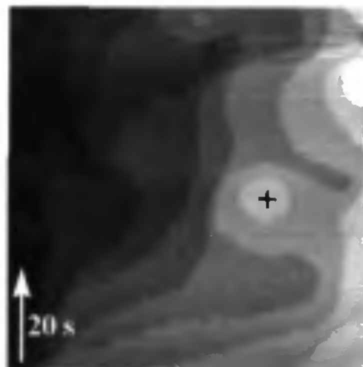
20 s

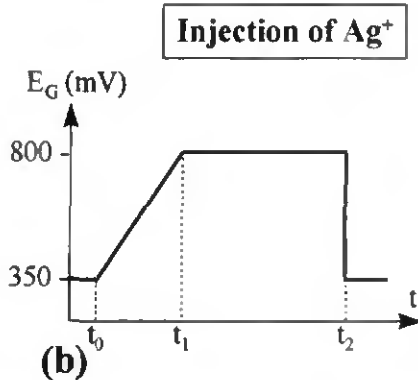
Injection of Ag^+
E_G (mV)
800
350
t
t_0
t_1
t_2
(b)

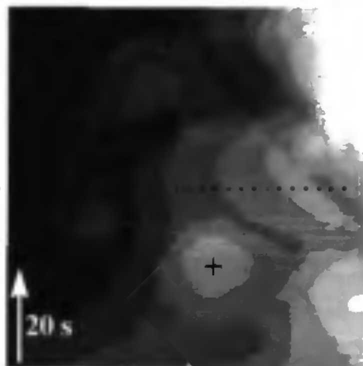
t_2
20 s

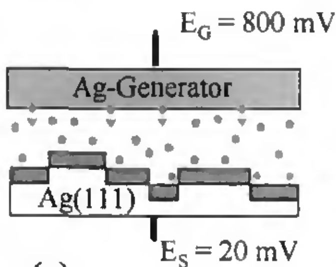
E_G = 800 mV
Ag-Generator
Ag(111)
E_S = 20 mV
(c)

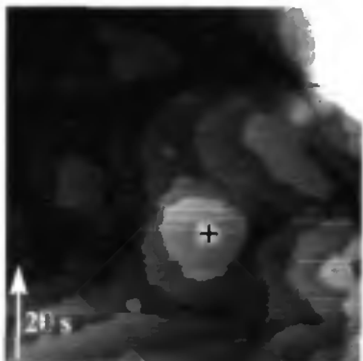

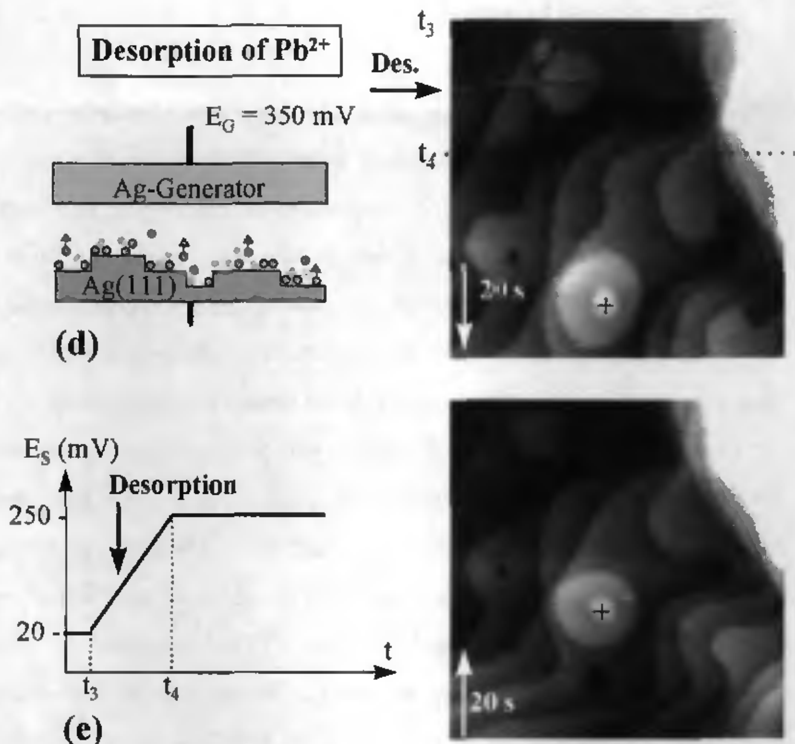

Fig. 7.4.4. Images of Ag<111> electrode (cavered with a Pb-manalayer) with manaatamic steps before (a), during (b) and abaut 4 minutes after (c) generation af a finite number af silver ions in the thin layer. The arrow in (d) indicates the desorptian of the Pb manalayer, and the silver surface with campletely desarbed lead is shawed in (e) Electralyte salution was 0.01 M $HClO_4$ + 0.005 M Pb^{2+}; windaw size: 100 x 100 nm; greyscale range: 2.5 nm. The mark (+) designs a reference paint an the substrate.

7.5. Conclusion to chapter 7

A fabrication technique was developed for a novel scanning probe type enabling electroactive compound determination and concentration control during electrolytic STM imaging within an electrolytic thin layer. The key step of this microfabrication process is the electrochemical growth of metal contacts (copper or gold) through photostructurable glass (Foturan). The geometry of these probes defines an electrolytic thin layer where the tip and an integrated ring electrode around it are immersed.

First measurements showed that electrolytic STM imaging with atomic resolution of an electrode surface with controlled deposition and desorption of electroactive species was possible in a thin layer electrolyte saturated with Ag ions. This demonstrated the validity of the Electrolytic Thin Layer Scanning Tunneling Microscope (ETL-STM) concept. This kind of STM imaging is of special interest for applications like metal underpotential deposits and corrosion studies (halide-induced corrosion mechanism, influence of pH).

References to chapter 7

1. G. Binnig and H. Rohrer, Helv. Phys. Acta, 55 (1982) 726
2. G. Binnig, H. Rohrer, Ch. Gerber and E. Weibel, Phys. Rev. Lett, 49, (1982) 57
3. *Scanning Tunneling Microscopy I/II*, (Edited by R. Wiesendanger and H.-J. Güntherodt), Springer Verlag, Berlin, 1992/1993
4. A. J. Bard, G. Denault, C. Lee, D Mandler and D. O. Wipf, Acc. Chem. Res. 23, 1990, p. 257
5. E. Schmidt, H. Siegenthaler, Helv. Chim. Acta 52 (1969) 2245
6. E. Schmidt, H. Siegenthaler, Helv. Chim. Acta 53 (1970) 321
7. E. Schmidt, H. Siegenthaler, J. Electroanal. Chem. 150 (1983) 59
8. D. Hülsenberg, R. Bruntsch, K. Schmidt and F. Reinhold, Silikattechnik 41 (1990) 11, 364
9. Schott/ IMM information: FOTURAN- a material for microtechnology
10. D. Hülsenberg, Microel. J. 28 (1997) pp. 419-432
11. M. Koudelka, Sensors & Actuators, 9 (1986) 249
12. U. Müller, D. Carnal et al., Phys.Rev. B 46 (1992) p.12899
13. U. Müller, D. Carnal et al., Phys.Rev. B 49 (1994) p.7795

Final conclusion

In this thesis, micromachining techniques were used to fabricate integrated SPM probes. As sharp tips are one of the key elements of SPM probes, one chapter was dedicated to them. A stylus-like AFM tip with an almost ideal shape was fabricated by combining two kinds of dry etching processes. Some wet etched tips were locally coated with diamond, to increase their resistance to wear. The local coating allows the further integration of sensing or actuating elements on the cantilevers. The tip effect was utilized in RIE to open small apertures on SNOM tips, and patterned thick photoresist layers were used to protect tips in wet and dry etching processes.

Then, an SPM device with integrated scanning actuators was discussed. It consists of an xy micro stage with integrated electrostatic comb actuators and sharp tip. The suitability of this xy micro table for AFM imaging was demonstrated and a scanning range of a few micrometers times a few micrometers was achieved. With such a structure, the expensive piezoelectric tube used for lateral scanning of the tip or the sample may be abandoned, and thermal and mechanical noise should be reduced.

Future AFM applications like very high density memories and integrated circuit inspection will require large arrays of cantilevers working in parallel. In such devices, each cantilever should have an independent actuation and detection unit, and tips should be uniform over the whole array. A fabrication process which allows the integration of reproducible self-sharpening tips on cantilever arrays with integrated self-

exciting piezoelectric sensors was presented. However, deposition and electro-mechanical behavior of the piezoelectric layers showed some undesirable characteristics and would require further development.

Finally, a novel probe for an electrolytic thin layer scanning tunneling microscope was fabricated. A special design allows the simultaneous STM imaging and the control of a generator or sensor electrode inside an electrolytic thin layer. First measurements showed that STM imaging of adsorption and desorption sequences is possible with this new probe.

Most of the work realized in this thesis has a common final goal: the microfabrication of fully integrated SPM units. There are at least four reasons to do this:

1) with the necessity of high throughput, a lot of future SPM applications will be working in parallel. This makes necessary the size reduction and integration of all the SPM components, as well as some signal treatment parts.
2) micro devices are our access to the nanoworld. The increasing complexity of the tasks to be realized at the nanoscale (very high density memories, DNA observations for example) requires efficient and flexible micro tools.
3) the batch fabrication of integrated devices could allow a dramatic price reduction of the unit element. Microfabricated devices may become as cheap and widely used as IC's today.
4) the pure technological performance. The academic working environment gave me a good and possibly unique opportunity to test how rich, powerful and also beautiful microfabrication is.

Acknowledgments

This dissertation is the result of my work at the Institute of Microtechnology of the University of Neuchâtel, in Prof. De Rooij's group, from 1993 to 1997. Obviously, I was helped and influenced by many discussions held in formal or informal ways. I would like to thank everyone who, in a direct or indirect way, contributed to the achievement of this PhD. dissertation.

Thank you! Professor Nico de Rooij, for giving me the opportunity to work in your team and to discover the fascinating world of microfabrication. Thank you! also for your always valuable advise and for trusting me in the good and bad moments of my fights with the divinities of technology.

Thank you! Urs Staufer, for letting me use, time to time, YOUR computer…and for some other small things!

I also would like to thank Professor Hans Siegenthaler and Erich Amman for their engagement in the electrolytic STM project and for their kindness and patience in trying to make me understand something about electrochemistry. This project about special STM probes could not have been achieved without the financial support of the Swiss National Science Foundation.

Thank you Professor Milena Koudelka-Hep for reading one chapter of this dissertation and for your caustic sense of humor.

I'm grateful to Philippe Luginbühl for his help with piezoelectric thin-layers and for our friendly collaboration.

Thanks also to S. Verpoorte for making my English readable and to M.-A. Grétillat for correcting one chapter of this thesis. I appreciated the collaboration of J. Brugger, V. P. Jaecklin and G.-A. Racine during the time we worked together.

Special thanks to Sabina Jenny, Sylviane Pochon, Pierre-André Clerc, Bastien Droz and Sylvain Jeanneret for their conscientious work, for their technological support and for their (almost) infinite patience. Thank you! Mathias Schulze, for helping me to solve every kind of computer problem and M. C. Strike for sharing the desk with me.

I also want to express my gratitude to the other actual or past members of the group, who shared part of their knowledge with me and who had to bear with me during all these years.

Thanks to Dr. P. Vettiger from IBM Rüschlikon and to Dr. H.-P. Herzig from Professor's Dändliker's group at IMT for agreeing to act as co-examiners of my work.

I'm specially grateful to Gianni Mondin, from Microsens, who evaporated metals on almost everything one could imagine and who allowed thus the development of some non-standard processes and to C. Ketterer, from CSEM, for taking the wonderful SEM micrographs.

The work on tips partially coated with diamond was realized in collaboration with Philippe Niedermann and Werner Hänni from CSEM, to whom I would like to express my gratitude.

I'm indebted to Martin Binggeli for his precious support in the realization of AFM images with the xy microstage.

Last but not least, I would like to thank Gregor Schürmann, Laurent Dellmann and Sylvain Roth for their collaboration in some serious and in many less serious activities.

Publication list

- P.-F. Indermühle, C. Linder, J. Brugger, V. P. Jaecklin and N. F. de Rooij, Design and fabrication of an overhanging xy-microactuator with integrated tip for scanning surface profiling, Sensors and Actuators A 43 (1994), pp. 346-350;

- P.-F. Indermühle, V. P. Jaecklin, J. Brugger, C. Linder, M . Binggeli and N. F. de Rooij, AFM imaging with an xy-micropositioner with integrated tip, Sensors and Actuators A 46-47 (1995), pp. 562-565;

-P.-F. Indermühle, G. Schürmann , G.-A. Racine and N. F. de Rooij, Self sharpening tip integrated on micro cantilevers with self-exciting piezoelectric sensor for parallel atomic force microscopy, Appl. Phys. Letters, Vol. 70, No. 17 (1997), pp. 2318-2319

-P.-F. Indermühle, G. Schürmann , G.-A. Racine and N. F. de Rooij, Fabrication and characterization of cantilevers with integrated sharp tips and piezoelectric elements for actuation and detection for parallel AFM applications, Sensors and Actuators A 60 (1997), pp. 186-190

-P.-F. Indermühle, G. Schürmann , G.-A. Racine and N. F. de Rooij, Atomic force microscopy using cantilevers with integrated tips and piezoelectric layers for actuation and detection, J. Micromech. Microeng. 7 (1997), pp. 218-220

- P.-F. Indermühle, S. Roth, L. Dellmann and N. F. de Rooij, Patterned thick photoresist layers for protection of protruding structures during wet and dry etching processes, accepted for publication in J. Micromech. Microeng.;

- P.-F. Indermühle, E. Ammann, P. Häring, R. Kötz, H. Siegenthaler and N. F. de Rooij, Electrolytic thin layer scanning tunneling microscope: fabrication and first results, Microelectr. Eng. 41/42 (1998), pp. 547-550

- J. Brugger, V. P. Jaecklin, C. Linder, N. Blanc, P.-F. Indermühle and N. F. de Rooij, Microfabricated tools for nanoscience, J. Micromech. Microeng. 3 (1993), pp. 161-167

- P. Niedermann, W. Hänni, D. Morel, A. Perret, N. Skinner, P.-F. Indermühle, N. F. de Rooij and P.-A Buffat, CVD diamond probes for nanotechnology, accepted for publication in Applied Physics A

- H. Siegenthaler, E. Ammann, P.-F. Indermühle, P. I. Oden and G. Repphun, Nanoscale probes of the solid-liquid interface, Proc. NATO Forum on Nanoscience and Technology 1997, Toledo (Spain), Kluwer Academic Publishers, to appear in 1998.